Simplest Model for Doped Conducting Polymer: Single-Crystalline Dimer Radical Cation Salts

Mori and Ozaki Groups

Conjugated polymers are essential materials in organic electronic device technologies owing to their mechanical flexibility, lightness, and solution processability. Among them, poly(3,4-ethylenedioxythiophene):poly(styrenesulfonate) (PEDOT:PSS, Fig. 1a), a polyion complex in which the positively charged PEDOT is stabilized by PSS anions, is one of the most widely used conducting polymers. The high conductivity (up to > 4000 S cm^{-1}), transparency, and solution processability have increasingly led them to a wide range of applications, for example, as a hole injection layer in organic photovoltaic (OPV) devices. Nevertheless, in-depth structural information of PEDOT:PSS is sorely lacking, which has severely limited the understanding of the structure-based conducting mechanism requisite for performance improvement; this also hampers molecular design strategies of next-generation electric conductors. One promising approach to elucidate the structure-property relationships of doped PEDOT is to utilize discrete oligo-EDOT·A models (A: counter anion, Fig. 1b). Recently, we developed oligo-EDOT·A models with less bulky methylthio (MeS) groups (i.e., 2MeS-2EDOT·A; A = BF_4^-, ClO_4^-, PF_6^-) that facilitate the growth of X-ray quality single crystals with adequately tight π-stacking. Combination of the atomic-level structural analyses and physical property measurements of the discrete oligomer systems revealed strong π–π interactions along the stacking direction as the origin of the excellent conductivity of doped PEDOT.

Single crystals of charge-transfer salts 2MeS-2EDOT·A were then synthesized by the electrochemical oxidation of 2MeS-2EDOT in the presence of n-Bu_4N·A electrolyte. The X-ray structural analyses at 293 K revealed a 1:1 composition of oxidized 2MeS-2EDOT (i.e., monovalent radical cation 2MeS-2EDOT$^+$) and counter anion A located in the voids of 2MeS-2EDOT$^+$ donors (Figs. 2a, b). In each structure of 2MeS-2EDOT·A, the donors were tightly stacked in a one-dimensional (1D) configuration with a head-to-tail pattern and with the donors rotated 1–3° at the centroid along the π-stacking axis. Interestingly, the donors were uniformly π-stacked in the range 3.46–3.48 Å, consistent with those predicted for PEDOT:PSS (3.43–3.51 Å).

We investigated the band structures based on the crystal structures using first-principles density functional theory (DFT) calculations (OpenMX software). Concerning the 1+ electronic charge of the molecule and its crystallographycally uniform π-stacking structure, the HOCO band exhibited a half-filled state with no energy gaps at the Fermi level (Fig. 2c), suggesting a metallic electronic state. The band width W of the HOCO band was determined to be as high as 0.998 eV (Fig. 2c). This result indicates the exclusively strong molecular interaction (W ≈ 1 eV) found in 2MeS-2EDOT·A. The geometric and electronic structures of π-stacking are the most critical factors for the high conductivity of doped PEDOT.

We then measured the electrical resistivity (ρ) of 2MeS-2EDOT·A. The ρ along the long axis direction of the crystal shape (the donor stacking *a*-axis) of 2MeS-2EDOT·BF_4 was determined as 2.8 × 10^2 Ω cm (Fig. 2d) at room temperature. From an Arrhenius plot, the activation energy was determined as 177.2 ± 0.9 meV, exhibiting almost no *T*-dependence. Considering the metallic

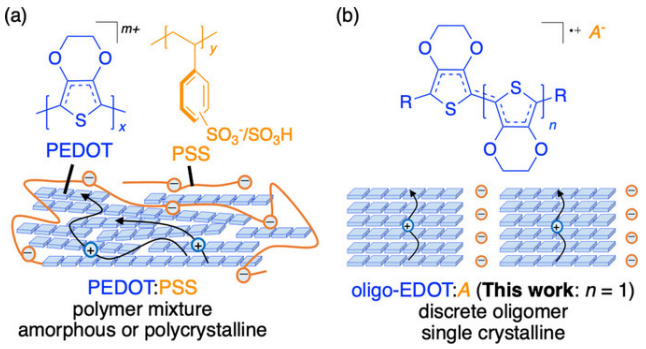

Fig. 1. Oligomer approach for doped PEDOT demonstrated in this study. (a) Structure of poly(3,4-ethylenedioxythiophene):poly(styrenesulfonate) (PEDOT:PSS). (b) Structure of discrete oligomer models: oligo-3,4-ethylenedioxythiophene (oligo-EDOT)·A (A = BF_4, ClO_4, PF_6).

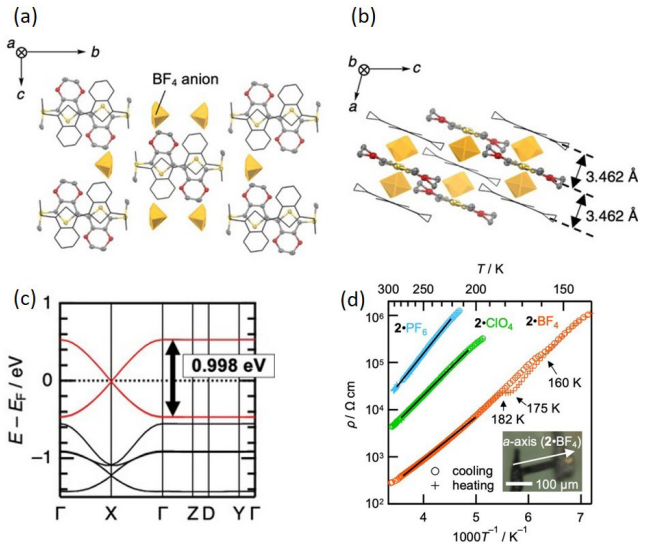

Fig. 2 Structures of 2MeS-2EDOT·BF_4 along (a) the a-axis and (b) the b-axis. The orange polyhedra represent the disordered BF_4 anions. (c) Calculated band structure of 2MeS-2EDOT·BF_4 and (d) ρ (resistivity) – Temperture−1 plots of 2MeS-2EDOT·A (A = BF_4, ClO_4, PF_6) Inset: a picture for the single crystal of 2MeS-2EDOT·BF_4 used in the measurement. Solid lines show fittings of the Arrhenius law.

half-filled electronic state indicated by the band calculations (Fig. 2c), the semiconducting behavior suggests that 2MeS-2EDOT·BF_4 is in a "genuine (half-filled) Mott state" with localized and poorly conducting electrons because of on-site Coulomb repulsion (U). The semiconducting behavior despite large W indicates that U is dominant over W in this system. Such a genuine Mott state (expressed as $U > W$) with large W is quite rare in organic conductor series. The semiconducting behaviors were likewise observed in 2MeS-2EDOT·ClO_4 and 2MeS-2EDOT·PF_6, and the room temperature ρ was determined as $4.3 \times 10^3\ \Omega$cm for 2MeS-2EDOT·ClO_4 and $4.3 \times 10^4\ \Omega$ cm for 2MeS-2EDOT·PF_6, respectively. The increase of ρ by one order of magnitude each was observed as the anion size increased and the π-stacking distances elongated (BF_4^-<ClO_4^-<PF_6^-, Fig. 2d). Activation energies were also determined as 223.6 ± 0.5 meV for 2MeS-2EDOT·ClO_4 and 277.9 ± 1.4 meV for 2MeS-2EDOT·PF_6, reflecting the chemical pressure effect from the anion sizes. It is to be noted that in the ρ–T^{-1} plot for 2MeS-2EDOT·BF_4, we observed a slight transition at 160 and 175 K for the cooling and heating processes, respectively, with a hysteresis of T (Fig. 2d), suggesting that a first-order phase transition is involved.

In conclusion, we developed tightly π-stacked models for discrete EDOT dimers 2MeS-2EDOT·A. These models exhibited unique 1D half-filled electronic structures with exclusively large band width ($W \approx 1$ eV) along the intracolumnar direction, implying the origin of the high electrical conductivity of doped PEDOT. The room temperature conductivities ($\sigma = \rho^{-1}$; < 3.6 μS cm^{-1}) were lower than that of doped PEDOT (> 4000 S cm^{-1}), which may originate in the genuine Mott state of our models caused by large U relative to W. The control of the competition between U and W in these systems (e.g., by elongating conjugation lengths to reduce U) may realize a variety of electronic states, including the metallic and even superconducting states. This unique approach of controlling U is accessible exclusively using our oligomer strategy. The construction of an oligomer library will further elucidate relationships between the structures and electronic properties.

References

[1] R. Kameyama, T. Fujino, S. Dekura, M. Kawamura, T. Ozaki, and H. Mori, A European Journal, **27**, 6696 (2021).
[2] R. Kameyama, T. Fujino, S. Dekura, and H. Mori, Phys. Chem. Chem. Phys. **24**, 9130 (2022).
[3] R. Kameyama, T. Fujino, S. Dekura, S. Imajo, T. Miyamoto, H. Okamoto, and H. Mori, J. Mater. Chem. C. **10**, 7543 (2022).

Authors

R. Kameyama, T. Fujino, S. Dekura, M. Kawamura, T. Ozaki and H. Mori

Topological Thermoelectric Effects in Organic Dirac Fermion System

Osada Group

Two topological thermoelectric effects, the nonlinear anomalous Ettingshausen effect and the quantized thermoelectric Hall effect, were investigated in the two-dimensional (2D) organic Dirac fermion (DF) system α-(BEDT-TTF)$_2$I$_3$.

(1) Nonlinear anomalous Ettingshausen effect (AEE)

So far, we have experimentally confirmed that the weak charge ordering (CO) state of α-(BEDT-TTF)$_2$I$_3$, which is the region close to the 2D massless DF phase in the CO phase, is a 2D massive DF state with a small CO gap. Because the finite Berry curvature dipole was expected in the massive DF state with tilted Dirac cones, we experimentally searched for the nonlinear anomalous Hall effect (AHE) in the current-carrying state in the weak CO state at zero magnetic field, and successfully observed it.

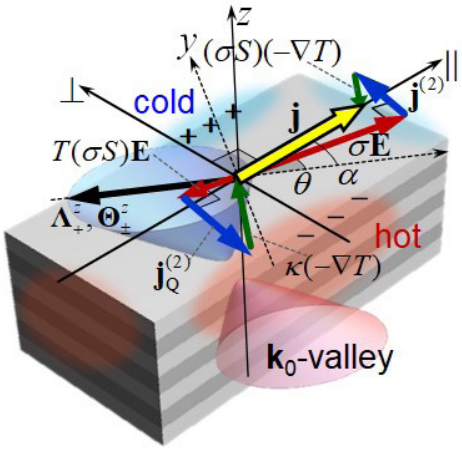

Fig. 1. Schematic of the current-induced topological transport phenomena, nonlinear anomalous Hall and Ettingshausen effects, in the current-carrying state in the thermally isolated 2D massive Dirac fermion system. $\mathbf{\Lambda}$ ($\mathbf{\Theta}$) indicates the (thermoelectric) Berry curvature dipole.

Here, we newly proposed a novel current-induced thermoelectric phenomenon, the nonlinear AEE, which is a thermoelectric analogue of the nonlinear AHE [1]. The thermoelectric Berry curvature dipole was introduced to explain this thermoelectric effect instead of the Berry curvature dipole. The nonlinear AEE is a phenomenon in which a temperature gradient proportional to the square current is induced in the direction perpendicular to the current. It exhibits rectifying characteristics (nonreciprocity). The generated transverse heat current flows unidirectionally even under an AC current. The nonlinear AEE occurs simultaneously with the nonlinear AHE as shown in Fig. 1. We estimated that the nonlinear AEE is sufficiently observable in the current-carrying state in the weak CO state of α-(BEDT-TTF)$_2$I$_3$.

(2) Quantized thermoelectric Hall effect (QTHE)

The high-performance thermoelectricity, that is boundless increase of the Seebeck coefficient S_{xx}, has been theoretically and experimentally investigated in 3D topological semimetals with nodal points (Dirac/Weyl semimetals) at the high-magnetic-field quantum limit. Recently, more advantageous thermoelectric effect called QTHE was proposed in the 2D massless DF system at the clean limit. The thermoelectric conductivity α_{xy} takes a quantized constant value of $(4\log 2)k_Be/h$, which is independent of temperature, magnetic field, and carrier density. It causes the boundless increase of S_{xx} even at low temperatures. α-(BEDT-TTF)$_2$I$_3$ was considered as one of candidate materials.

We investigated the thermoelectricity of the 2D massless DF system in real α-(BEDT-TTF)$_2$I$_3$ under high magnetic fields [2]. Because of its small electron group velocity, the Zeeman splitting becomes relatively important and cannot be ignored in α-(BEDT-TTF)$_2$I$_3$. We showed that the Zeeman splitting of the $n = 0$ Landau level suppresses the QTHE: α_{xy} decreases from the quantized value at low temperatures leaving a shoulder-like structure, and S_{xx} decreases after linear increase at high magnetic fields leaving a hump-

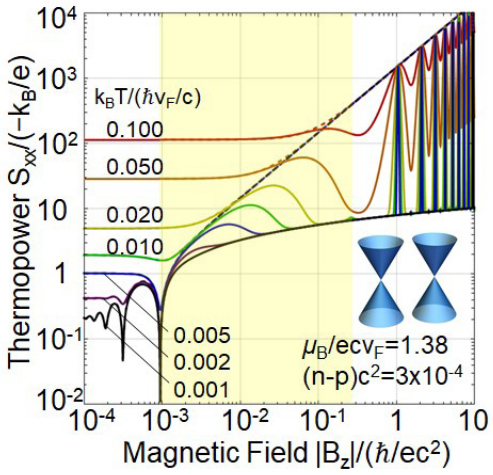

Fig. 2. The magnetic field dependence of the Seebeck coefficient of the 2D massless Dirac fermion system at a fixed carrier density around the charge neutrality point. The solid and dashed curves are for cases with and without the Zeeman effect.

like structure (Fig. 2). These features were observed in our previous experiment. In contrast to 3D nodal-point semimetals with robust gapless features, it is difficult to realize the QTHE in real 2D Dirac fermion systems due to the Zeeman gap in the $n = 0$ Landau level under high magnetic fields.

References
[1] T. Osada and A. Kiswandhi, J. Phys. Soc. Jpn. **90**, 053704 (2021).
[2] T. Osada, J. Phys. Soc. Jpn. **90**, 113703 (2021).

Authors
T. Osada, A. Kiswandhi, M. Sato, K. Uchida, and T. Taen

Discrete Time Crystals in Solids

Tsunetsugu Group

A discrete time crystal (DTC) is an exotic nonequilibrium phase of matter that is realized in periodically driven quantum systems and characterized by the breakdown of the discrete time translation symmetry [1]. The DTC phase has been well studied and experimentally demonstrated

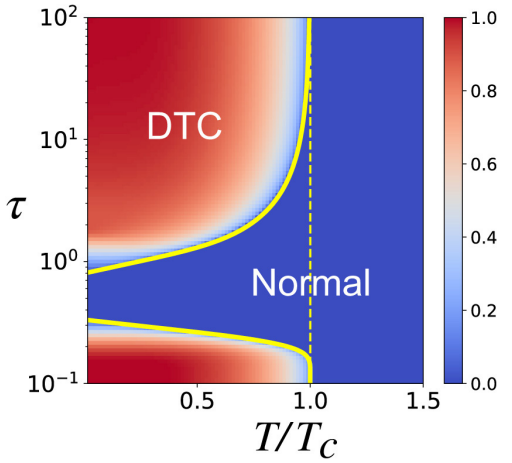

Fig. 1. Phase diagram of the discrete time crystal in solids, and the amplitude of the DTC order parameter is shown by color. The temperature T of the bath is normalized by the equilibrium ferromagnetic transition temperature T_c. τ is the interval between the consecutive pulses in units of $J = \hbar = 1$ (J is the exchange energy).

in artificial quantum systems without dissipation, such as trapped ions, NV centers in diamonds, and digital quantum computers. However, it had not been explored in solid-state materials, in which unavoidable dissipation is hard to control. Therefore, if one realizes the DTC phase in those materials, it could offer a new possibility of controlling their properties and functionalities.

In this study [2], we have studied the DTC phase in solid-state materials and uncovered its mechanism and properties. We have analyzed a ferromagnetic quantum Ising model periodically driven by a train of magnetic field pulses each corresponding to (nearly) π-pulse (period τ). Using the Floquet-Redfield equation, we have incorporated dissipations due to the couplings of the quantum spins to their surrounding phonon bath. This is much harder to solve than the usual Schrödinger equation because it requires treating a $D \times D$ density matrix rather than a D-dimensional wave function (D denotes the Hilbert space dimension, which increases exponentially with the number of spins). To circumvent this problem, we have employed the mean-field theory and numerically obtained the DTC order parameter in a self-consistent manner.

Performing massive numerical calculations on the supercomputer at ISSP, we have determined the DTC phase diagram in solids as shown in Fig. 1. In the normal phase, the system relaxes to a nonequilibrium steady state which oscillates periodically with the same period τ as the drive's. On the other hand, in the DTC phase, the system turns into a time crystal which oscillates with the doubled period 2τ. These results show that DTCs can be realized in real magnetic materials subject to dissipation at low temperatures if the pulse interval is either long or short enough. Interestingly, this phase diagram highlights a reentrant behavior of the DTC phase as the pulse interval is varied.

We have further proposed how to realize and detect the DTC in experiments. We have analyzed the robustness of the DTC against imperfections in pulse shapes unavoidable in experiments such as their height and duration; We have shown that those imperfections do not break the DTC phase. We have also shown that critical phenomena accompany the DTC phase transition. In particular, when temperature is varied to cross the DTC/normal phase boundary, the decay of the DTC order parameter exhibits a power-law in time rather than an exponential. This characteristic behavior can be used as an indicator for the DTC in finite-time experiments. We have finally estimated the parameters for realizing DTC phase and proposed that the electron spin resonance on some magnetic materials may be a promising experimental platform. We believe that these results pave the way for a new research field of time crystals in material science.

References
[1] K. Sacha and J. Zakrzewski, Rep. Prog. Phys. **81**, 016401 (2018).
[2] K. Chinzei and T. N. Ikeda, Phys. Rev. Research **4**, 023025 (2022).

Authors
K. Chinzei and T. N. Ikeda

High-Harmonic Generation in GaAs beyond the Perturbative Regime

Itatani and Kato Groups

Recently, high-harmonic generation (HHG) has been experimentally observed in solids. In contrast to gaseous media, solids have the vastly diverse nature such as in their band structures, energy gaps, crystalline anisotropy, and magnetism. It has thus far been experimentally and theoretically investigated in various solids, but comprehensive understanding of the crossover behavior from the perturbative to the nonperturbative regime has not been gained yet. Such an understanding requires a unified viewpoint connecting the perturbative to nonperturbative regimes.

In the perturbative regime, it is well known that the intensity of the nth-order harmonics obeys an E^{2n} scaling law with respect to the field amplitude E. In the conventional formulation of nonlinear optics using the Bloch basis, this scaling law is successfully explained by the multiphoton interband transition of Bloch electrons. The E^{2n} scaling, however, breaks down at sufficiently high fields (typically at several MV/cm). In recent theoretical studies, this nonperturbative nature of HHG is explained by the alternative formulation, in which intraband electron acceleration motion is taken into account with a new basis called the Houston basis. In spite of these theoretical developments, it has not been clarified yet how the properties of HHG in the nonperturbative regime are seamlessly connected to those in the perturbative regime where the E^{2n} scaling holds. For a clear understanding on this crossover behavior, accurate measurement of the field-intensity dependences of HHG is crucial and indispensable.

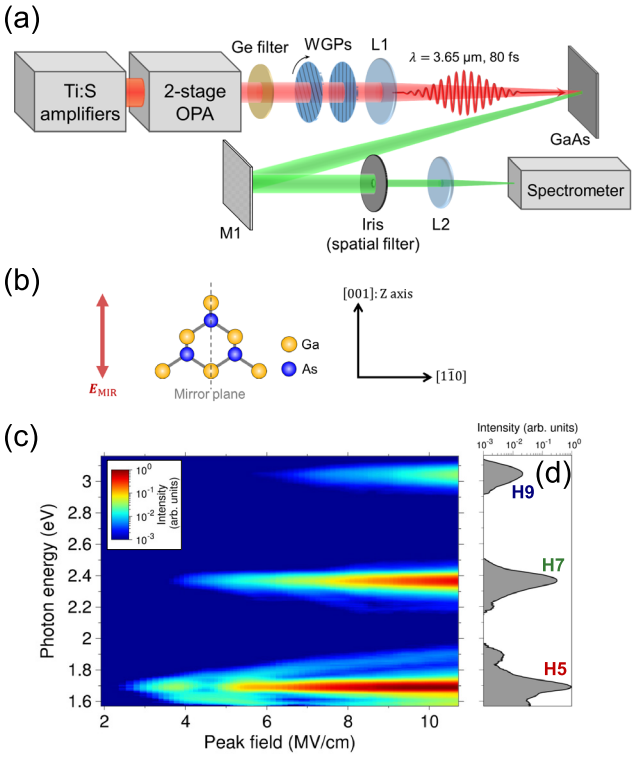

Fig. 1. (a) Experimental setup for HHG in reflection geometry using bulk GaAs and MIR laser source. Ti:Sapphire regenerative and multi-pass amplifiers (450Hz, 5 mJ, 70 fs) were used to pump the optical parametric amplifier (OPA). WGPs, a pair of wire-grid polarizers; L1 (f = 300 mm) and L2 (f = 50 mm), CaF_2 lenses; M1 (R = 100 mm), Al-coated concave mirror. (b) Structure of the (110) surface of GaAs and direction of the laser polarization. (c) Field-intensity dependences of the 5th, 7th, and 9th harmonic spectra. (d) HHG spectrum at the peak field of 10 MV/cm.

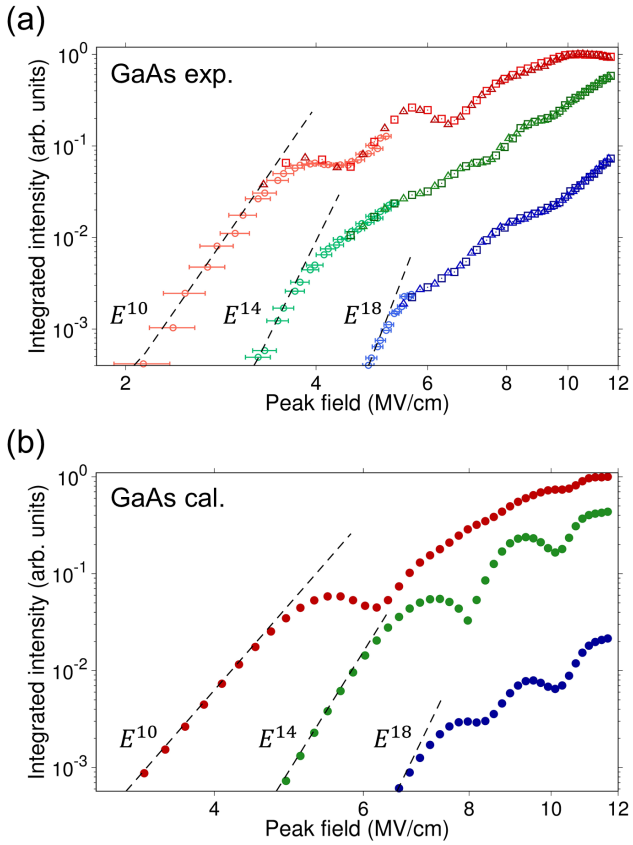

Fig. 2. (a) Field-intensity dependences of the 5th (red), 7th (green), and 9th (blue) HHG intensities. Two datasets (squares and triangles) were measured in a single sweep starting from 2 to 12 MV/cm and then from 12 to 2 MV/cm, respectively. Small HHG signals (circles) were measured with a longer acquisition time. (b) Calculated results of the Luttinger-Kohn model. In the weak-field regime, the harmonic intensities almost obey an E^{2n} perturbative scaling law for both the measured and calculated results (dashed black lines).

Based on this motivation, we experimentally and theoretically investigated the field-intensity dependence of HHG in GaAs [1]. The experiments were carried out by using an intense mid-infrared laser irradiating a GaAs sample, as shown in Fig. 1(a) , in the reflection geometry to minimize nonlinear propagation effects and phase mismatch [2]. We set the pulse duration and the wavelength of the incident light to be 80 fs and 3.65 μm. The peak field was estimated to be up to 12 MV/cm inside the sample. We measured the HHG intensities as a function of the peak field of the incident pulses from 2 to 12 MV/cm. We show in Figs. 1(c) and 1(d) the obtained HHG spectra which indicate only odd-order harmonics due to the inversion symmetry of GaAs (Fig. 1(b)). Fig. 2(a) shows the intensities of the 5th, 7th, and 9th harmonics as a function of laser intensity. This figure indicates that harmonic intensities did not saturate monotonically with increasing laser intensity, but rather exhibited oscillations. As the field intensity was increased, the oscillatory behaviors appeared above 4, 5, and 6 MV/cm for the 5th, 7th, and 9th harmonics, respectively, where they started to deviate from the perturbative scaling law. An explanation of these experimental results will require clarification of the crossover of HHG from the perturbative to the nonperturbative regime as well as the physical origin of the oscillatory behavior.

To analyze these experimental results, we employed an eight-band Luttinger-Kohn model, which includes conduction, heavy-hole, light-hole, and split-off bands for both spin-up and spin-down components. We introduce our

theoretical framework by applying our previous works [3,4] to the Luttinger-Kohn model and calculate the intensities of the 5th, 7th, and 9th harmonics originating from GaAs. Consequently, we succeed in reproducing E^{2n} scaling laws in the perturbative regime as well as the oscillatory behaviors in the non-perturbative regime (Fig.2(b)). By performing further analyzation, we concluded that the diagonal elements of the Hamiltonian representing field-induced dynamic band modification is crucial in the nonperturbative regime. Since this field-induced dynamic band modification can naturally be ignored in the perturbative regime, we can easily obtain the HHG intensities showing the crossover behavior from the perturbative to the nonperturbative regime. The findings of our work give important foundation for understanding a variation of nonlinear optics from the perturbative to nonperturbative regime and open up the possibility of novel optical technologies, such as strong-field coherent control of solid HHG and Floquet engineering of dressed states in solids.

References

[1] T. Tamaya, P. Xia, C. Kim, F. Lu, T. Kanai, N. Ishii, J. Itatani, H. Akiyama, and T. Kato, Phys. Rev. B **104**, L121202 (2021).
[2] P. Xia, C. Kim, F. Lu, T. Kanai, H. Akiyama, J. Itatani, and N. Ishii, Opt. Express **26**, 29393 (2018).
[3] T. Tamaya, A. Ishikawa, T. Ogawa, and K. Tanaka, Phys. Rev. Lett. **116**, 016601 (2016).
[4] T. Tamaya and T. Kato, Phys. Rev. B **100**, 081203(R) (2019).

Authors

T. Tamaya*, P. Xia*, C. Kim, F. Lu, T. Kanai, N.Ishii, J. Itatani, H. Akiyama, and T. Kato

*T. T. and P. X contributed equally to this work

Einstein-de Haas Nanorotor

Kato Group

The angular-momentum conversion phenomena between spin and mechanical rotation are recognized as the gyromagnetic effects discovered in the early 20th century by S. J. Barnett, A. Einstein, and W. J. de Haas. They observed magnetization induced by mechanical rotation [1] and mechanical rotation induced by magnetization [2] known as the Einstein-de Haas (EdH) effect, revealing the origin of magnetism is the angular momentum. The gyromagnetic effects are universal phenomena that appeared even in nonmagnetic materials ranging from macroscopic to microscopic scales in various branches of physics, including ultracold atoms, spintronics, nuclear spin physics, and quark-hadron physics.

In our study [3], we developed a quantum theory to describe the microscopic mechanism of a nanorotor driven by electron spin injection via the EdH effect. As a feasible setup, we considered the double-wall carbon nanotube rotor as shown in Fig. 1 (a). For the double-walled carbon nanotube, mechanical rotational motion of the inner carbon nanotube was already studied both experimentally [4] and theoretically [5]. However, efficient driving forces for the rotational motion are still lacking.

In this system, the rotor (the inner carbon nanotube) is driven by four transitions as shown in Fig. 1 (b). By applying a bias voltage between two half-metallic ferromagnetic electrodes, an electron with a spin $s_z = \hbar/2$ tunnels from the left electrode into the nanorotor (from (b-1) to (b-2)). This electron cannot tunnel to the drain electrode as long as its spin state remains $s_z = \hbar/2$ because there is no electronic

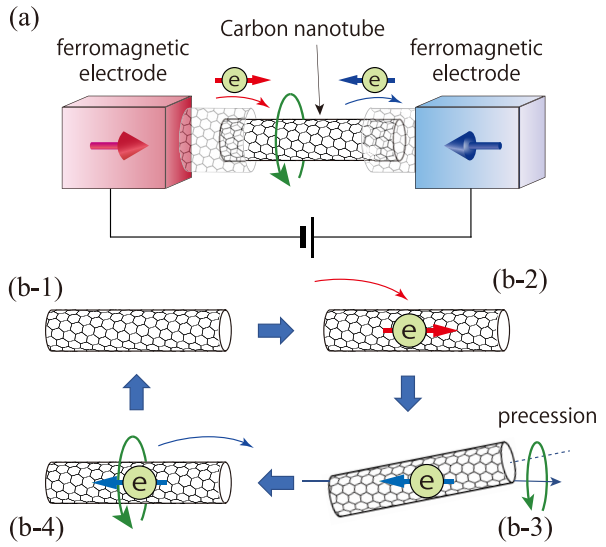

Fig. 1 Schematic diagram of the nanorotor rotationally driven by spin injection. (a) The system consisting of a double-wall carbon nanotube and two ferromagnetic electrodes. (b) The four processes for driving of rotational motion of the nanoroter.

state for the spin $s_z = \hbar/2$ in the half-metallic ferromagnetic drain. Electron accumulation by additional electron tunneling is also forbidden because of the Coulomb blockade in the nanorotor that acts like a quantum dot. Therefore, only spin flipping of the injected electron enables continuous current flow through the rotor (from (b-2) to (b-3)). Simultaneously with this spin flipping, angular momentum $\hbar$ is eventually transferred from the injected electron to the mechanical rotational motion. After this angular momentum transfer, the electron with the spin $s_z = -\hbar/2$ can leave the nanotube into the right electrode. Therefore, the current through the nanorotor is expected to be a driving force of the rotational motion of the nanorotor in this system. In our study, we clarified that the precession of the nanorotor as shown in Fig. 1 (b-3) always occurs in the angular momentum transfer from the electron spin to the nanorotor. Therefore, in order to drive the nanorotor efficiently, the state of the nanoroter is needed to be relaxed from a precession state into a sleeping top state (from (b-3) to (b-4)).

The transition into the precession state is explained as follows. When the nanoroter is assumed to be a rigid body, its quantum states are specified by three quantum numbers, L, M, and k, where L is the quantum number corresponding

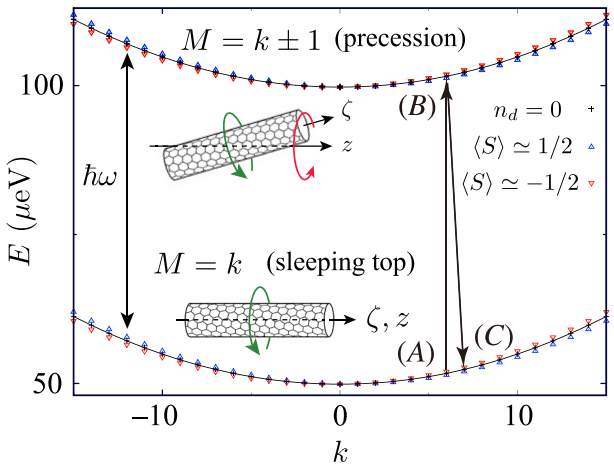

Fig. 2. Eigenenergies of rotational motion as a function of k. The upper and lower branches correspond to the precession state ($M = k \pm 1$) and the sleeping top state ($M = k$), respectively.

to the magnitude of the angular momentum, M is the z component of the angular momentum, and k is the angular momentum around the axis of the rotor. In Fig. 2, we show the eigenenergies of the roter for the sleeping top state ($M = k$, the lower inset of Fig. 2) and the precession state ($M = k \pm 1$, the upper inset of Fig. 2). We showed that the spin-rotation coupling between electron spins and the nanoroter induces only the transition from (A) to (B) in Fig. 2 because the spin-rotation coupling only changes M without changing k. Therefore, we need to introduce a phonon heat bath which causes relaxation from the precession state (B) to the sleeping top state (C). In our work [3], we discussed a detailed condition for efficient and stable driving of the rotational motion of the nanoroter.

The present driving mechanism is not restricted to carbon nanotubes; it applies to other materials as well. The process discussed here would be a minimal model for the momentum transfer from an electron to rotor that effectively includes the other possible processes.

This study has been performed as a joint study with Mamoru Matsuo, who was a visiting professor of ISSP in the academic year 2016.

References

[1] S. J. Barnett, Phys. Rev. **56**, 239 (1915).
[2] A. Einstein and W. J. de Haas, KNAW proc. **18 I**, 696 (1915).
[3] W. Izumida, R. Okuyama, K. Sato, T. Kato, and M. Matsuo, Phys. Rev. Lett. **128**, 017701 (2022).
[4] A. M. Fennimore, T. D. Yuzvinsky, W.-Q. Han, M. S. Fuhrer, J. Cumings, and A. Zettl, Nature **424**, 408 (2003).
[5] S. W. D. Bailey, I. Amanatidis, and C. J. Lambert, Phys. Rev. Lett. **100**, 256802 (2008).

Authors

W. Izumida[a], R. Okuyama[b], K. Sato[c], T. Kato, and M. Matsuo[d]
[a]Tohoku University
[b]Meiji University
[c]National Institute of Technology, Sendai College
[d]Kavli Institute for Theoretical Sciences, University of Chinese Academy of Sciences

Orbital Torque in Ferromagnetic-Metal/ Ru/Al_2O_3 Trilayers

Otani Group

For the development of spintronic memory and logic devices, the efficient current-induced spin-torque effect is critical. Spin-orbit torque, which uses spin-orbit coupling (SOC) in heavy metals (and/or Rashba interfaces) to create spin current and resulting torque to switch the magnetization of a neighboring ferromagnetic layer, has received a lot of attention in the last decade. The torque effect based on orbital angular momentum injection and SOC in the ferromagnet, known as orbital torque (OT), has recently attracted much attention. While each electronic state in a spin current may only carry $\hbar/2$ angular momentum, the angular momentum carried by a state in an orbital current has no limit, implying that OT has higher efficiency. Indeed, in most metal elements, orbital-current production efficiency is substantially higher than its spin equivalent. Furthermore, because SOC is not required, the materials choices for the orbital source are pretty broad, rather than being confined to a few types of heavy metals like spin-current generation. As a result, OT is a strong contender for the operating principle of practical spintronic devices.

The development of OT devices based on polycrystalline stacks is beneficial for industrial on-silicon manufacture. OT was previously discovered primarily due to the interfacial orbital Rashba effect (ORE) in polycrystalline layered structures grown by room-temperature evaporation or sputtering, which can modulate OT through layer design. These studies use an interface or a bulk containing Cu or Pt as a source of orbital angular momentum. The full d-shell of Cu and the high SOC of Pt obstruct orbital transport and make OT analysis in polycrystalline stacks more difficult. Oxidation helps orbital transport in Cu, adding complexity to the structure. Meanwhile, theoretical works have focused on the orbital generation and transport in single-crystalline systems because of the complexity of orbital transport in polycrystalline heterostructures. It is highly warranted to bridge the gap between experiment and theory by obtaining efficient, long-range orbital transport in a uniform polycrystalline layer and developing a corresponding theoretical approach to orbital transport that remains elusive.

We experimentally study the current induced torque effect in polycrystalline ferromagnetic metal (FM)/Ru/Al_2O_3 stacks shown in Fig. 1(a). FM is either $Co_{40}Fe_{40}B_{20}$ or $Ni_{80}Fe_{20}$. Using a device structure, we demonstrate a high torque efficiency due to the ORE at the Ru/Al_2O_3 interface (Fig. 1(b)). Ru is chosen because of its electronic configuration of $4d^75s^1$ and a small bulk-originating spin-orbit torque so that orbital-current generation is allowed by orbital hybridization; the absence of d-electrons does not limit orbital-current propagation at the Fermi level or SOC-related relaxation, and OT is not disturbed by the conventional spin Hall torque. We performed spin-torque ferromagnetic resonance (ST-FMR) measurements

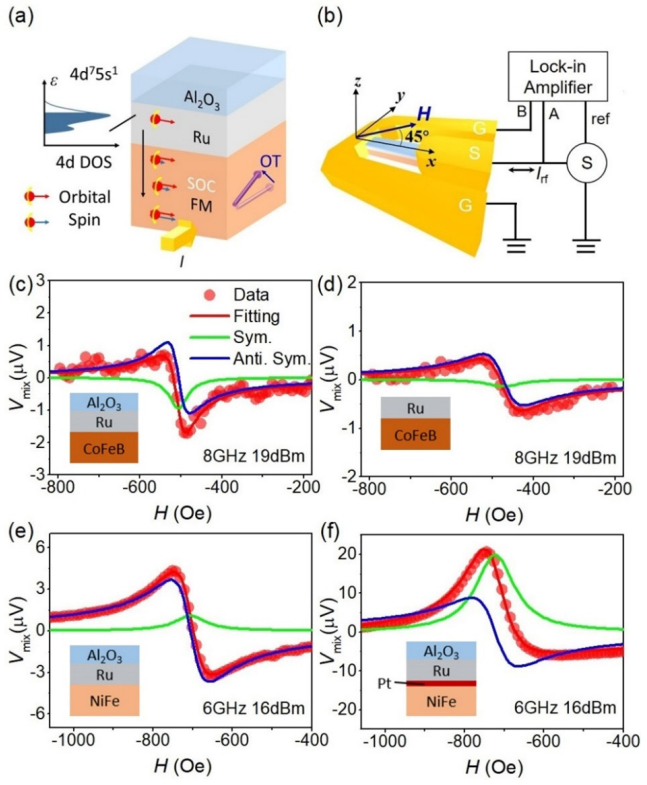

Fig. 1. (a) Schematic of the orbital torque in FM/Ru/Al_2O_3. (b) Experimental setup of the ST-FMR measurement. (c)–(f) ST-FMR spectra and fitting for the CoFeB(7)/Ru(6)/Al_2O_3(2) (c) and CoFeB(7)/Ru(6) (d) devices at 8 GHz, and NiFe(7)/Ru(6)/Al_2O_3(2) (e) and NiFe(7)/Pt(1)/Ru(6)/Al_2O_3(2) (f) devices at 6 GHz. The red circles are experimental data; the red lines are fitting curves. The symmetric and antisymmetric components plots are in the right panel with green and blue lines. Schematics of the sample layout are shown in the inset.

(Fig. 1(b)) on the polycrystalline FM/Ru/Al_2O_3 stacks. Figure 1(c) shows the V_{mix} signal obtained from the ST-FMR measurement of a $Co_{40}Fe_{40}B_{20}$(7)/Ru(6)/Al_2O_3(2) (units in nanometers) trilayer. The signal V_{mix} is decomposed into symmetric (S) and asymmetric (A) Lorentzian components, revealing sizable negative S components that indicates the current-induced damping-like torque. From systematic studies in this work, we find characteristic behaviors of OT: (i) the sign and magnitude of the torque efficiency are strongly dependent on the FM materials and insertion layers according to the sign and magnitude of their SOC (Fig. 1(c) and (e)); and (ii) torque efficiency is enhanced with increasing CoFeB layer thickness t_F, with a large saturation torque efficiency of 0.3 for t_F = 12 nm, consistent with the long propagation length of the orbital current in the ferromagnet. Our quantum evolution simulation shows the unique random processing feature of orbital transport in polycrystalline materials, enabling long-range orbital transport in polycrystalline samples, even in a crystal field.

This study concludes that transition metal-based materials with a small SOC, simple structure, and itinerant d-electrons can provide a suitable platform for studying orbital transport in polycrystalline structures and developing torque devices.

Reference

[1] L. Liao, F. Xue, L. Han, J. Kim, R. Zhang, L. Li, J. Liu, X. Kou, C. Song, F. Pan, and Y. Otani, Phs. Rev. B **105**, 104434 (2022).

Authors

L. Liao, F. Xue[a], L. Han[b], J. Kim[c], R. Zhang[b], L. Li[a], J. Liu[a], X. Kou[a], C. Song[b], F. Pan[b], and Y. Otani

[a]ShanghaiTech University

[b]Tsinghua University

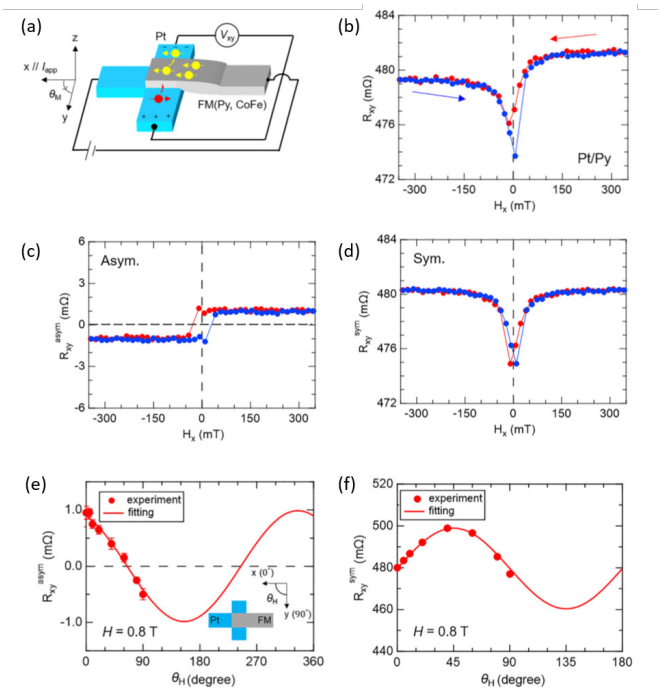

Fig. 1. (a) Schematic of ISHE measurement in the T-shaped spin conversion device. (b) Magnetic field dependence of the transverse resistance *Rxy* in the Pt/FeNi device with θ = 0°. Red and blue arrows show the magnetic field sweeping direction. (c), (d) asymmetric and symmetric components of *Rxy*. (e), (f) Magnetic field angle dependences of the asymmetrical and symmetrical components H = 0.8 T.

Planar Hall Effect on the Output Signal in T-Shaped Spin Conversion Device

Otani Group

The T-shaped spin conversion device consisting of ferromagnetic and spin Hall (or spin conversion) materials is an indispensable component in a new type of logic circuit: magnetoelectric spin-orbit logic circuit. In this device, a spin polarized current is directly injected into the spin Hall material from the ferromagnet, and the inverse spin Hall effect (ISHE) is detected as the transverse voltage as shown in Fig. 1 (a). The output signal can be an order of magnitude greater than that of the nonlocal methods. Pham et al. have demonstrated an increase in the ISHE signal by scaling down the T-shaped device structure, that is favorable for the high-density device [1]. They also discussed the adverse effects of the adjacent ferromagnet on the total signal via a transverse anisotropic magnetoresistance, the planar Hall effect (PHE), concluding that it only causes the offset of the output signal. However, our recent experiments showed the superposition of the signal induced by PHE which change its sign upon magnetization reversal.

In this work, we investigated the influence of PHE on the ISHE induced voltage on the T-shaped device. The T-shaped Pt wires were first formed on the Si/SiO_2 substrate using e-beam lithography, e-beam deposition, and liftoff. The thickness of Pt is 20 nm. We then deposited a ferromagnetic wire on the Pt. Figure 2(b) shows the magnetic field dependence of R_{xy} in the Pt/FeNi device. One can extract the asymmetric contribution in R_{xy} by calculating the difference between the signals measured at trace and retrace scan. Figures 1(c) and (d) show asymmetric and symmetric components as a function of the applied field, respectively. Figure 1 (e) and (f) show the magnetic field angle dependences of the symmetric and symmetric components, respectively. The ISHE causes an asymmetric component of the transverse resistance in the T-shaped device structure. On the other hand, we found that the PHE contributes to the transverse voltage as a symmetric component because the magnetic moment continuously rotates clockwise (or counterclockwise). From the experimental results, the spin Hall angle of Pt and the anisotropic magnetoresistance ratio of FeNi were estimated to be ~ 3.0% and ~ 1.0%, respectively, that are in the same order as the reported value. We did same measurement on a Pt/CoFe device. The overall change in the asymmetric component is almost the same as that in the Pt/FeNi, while the change in the symmetric component is about half of that in the Pt/FeNi device. This reduction of the symmetric signal is attributed to the lower anisotropic magnetoresistance ratio of CoFe than that of FeNi. Therefore, it is essential to use the ferromagnet that has small anisotropic magnetoresistance ratio to reduce the adverse effect in the T-shaped device.

In conclusion, our systematic studies reveal that the PHE causes a symmetric component in the output signal because of the continuous clockwise (or counterclockwise) magnetic rotation. We find that we can suppress the undesired signal by choosing a low AMR ferromagnet such as the CoFe alloy. These results help us to design the T-shaped device structure for studying spin conversion in spin Hall materials, topological insulators, and Rashba interface for developing the spintronic logic devices.

References
[1] V. T. Pham, I. Groen, S. Manipatruni, W. Y. Choi, D. E. Nikonov, E. Sagasta, C.-C. Lin, T. A. Gosavi, A. Marty, L. E. Hueso, I. A. Young, and F. Casanova, Nat. Electron. **3**, 309 (2020)
[2] H. Mizuno, H. Isshiki, K. Kondou, Y. Zhu, and Y. Otani, Appl. Phys. Lett. **119**, 092401 (2021)

Authors
Y. Otani and H. Isshiki

Squeezed Abrikosov-Josephson Vortex

Hasegawa Group

Two-dimensional (2D) superconductors are sensitive to the presence of disorder, which induces electron localization, phase fluctuation, and eventually the superconducting-insulator transition at zero temperature. Here we present a new way of introducing disorder into high-quality monolayer superconductors by forming them on vicinal substrates. We fabricated the striped incommensurate (SIC) structure, one of the Pb monolayer superconducting phases, on vicinal Si(111) substrates tilted by 1.1° or 0.5°. Since each step works as a disorder and behaves like a Josephson junction, by just adjusting the miscut angle, the step separation, or disorder density, can be controlled precisely.

The role of a single step on atomic-layer superconductors has been investigated by scanning tunneling microscopy (STM) [1]. The shape of vortex cores trapped at steps depends on how the step decouples the superconducting terraces. When the decoupling is weak, round Abrikosov vortex is pinned at the step. With the intermediate decoupling, trapped vortices are elongated along the step, which is called a Abrikosov-Josephson vortex (AJV) and their local density of states (DOS) within the gap is not fully recovered at the core. In the case of the strongly decoupling step, a further elongated vortex with local DOS almost same as that of superconducting states, that is, Josephson vortex, is formed along the step.

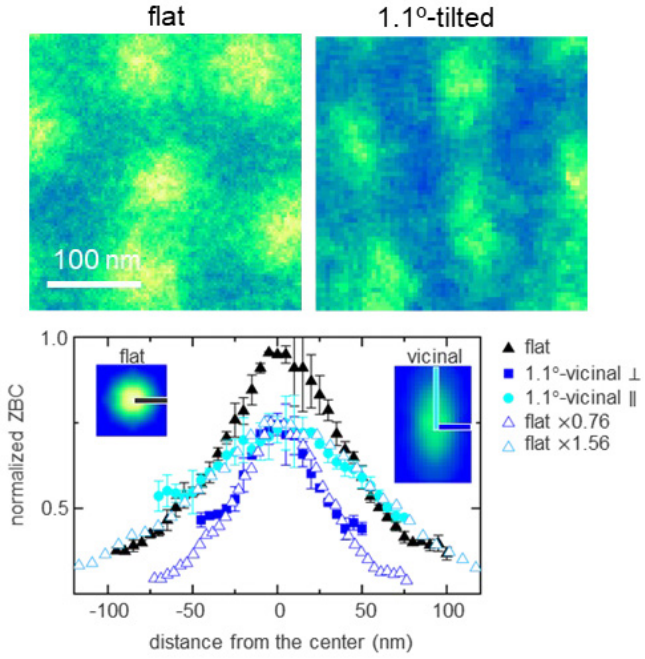

Fig. 1. (upper panels) ZBC maps taken on flat and 1.1°-tilted vicinal SIC samples showing vortices under out-of-plane magnetic field of 120 mT. (lower panel) ZBC profiles across the vortex center taken on the flat (black triangles) and the vicinal (blue squares and light blue circles) samples, respectively. Blue squares (light blue circles) indicate the profiles taken in the direction perpendicular (parallel) to the steps. Empty blue (light blue) triangles are the profile taken on the vortices of the flat sample multiplied by 0.78 in height and by 1.56 (0.76) along the horizontal axis, demonstrating similarity in the three profiles. Insets show the averaged vortices taken on the flat and vicinal samples.

Through the electron transport measurement under out-of-plane magnetic fields B, we found that the critical magnetic field (B_{c2}) of the superconducting phase formed on vicinal substrates is higher than that formed on the flat substrate. Using STM at 0.36 K, we estimated B_{c2} from the magnetic field that saturates the conductance at the bottom of the superconducting gap, that is, zero bias conductance (ZBC), and found consistent with those of the transport measurements.

In order to understand the enhanced B_{c2} microscopically, we investigated vortices by STM. The upper panels of Fig. 1 are ZBC maps showing the vortices taken on the flat and 1.1°-tilted SIC sample under B = 120 mT. Compared with the round vortices observed on the flat sample, the vortices on the tilted sample are elongated along the step direction. In addition, ZBC at the center is suppressed. Since both are characteristic features of AJV we attribute them to an AJV.

According to the Ginzburg-Landau (GL) equation, the critical field is inversely proportional to ξ^2. Since the size of vortex is closely related to ξ, we investigated the size and shape of the vortices. The lower panel of Figure 1 shows the ZBC cross-sectional profiles taken on vortices on the flat sample (black triangles), on the vicinal sample in the directions parallel (//, light blue circles) and perpendicular ($\perp$, blue squares) to the steps. From the plot we found that these three profiles have a similar shape. First, on the vortices of the vicinal sample, ZBC at the center is suppressed by a factor of 0.78. Then, the suppressed profile was laterally expanded by a factor of 1.56 (shrunk by 0.76) to find good agreements with the parallel (perpendicular) profiles of the vicinal sample's vortices.

Curiously, the squeezing ratio in the perpendicular direction, 0.76, corresponds well to the inverse of the B_{c2} enhancement ratio ($B_{c2,flat}/B_{c2,vicinal}$). According to the anisotropic 2D GL model, $B_{c2,vicinal}$ is given by $\Phi_0/2\pi\xi_\perp\xi_{//}$, where $\xi_\perp$ and $\xi_{//}$ are the coherence length in the directions perpendicular and parallel to the steps. Thereby the correspondence suggests us that the B_{c2} enhancement is due to the reduced coherence length $\xi_\perp$ by the presence of the steps.

The reduction in ξ by the high-density steps is explained by the suppression of mean free path l by disorder according to the equation $\xi = \sqrt{\xi_0 l}$, where ξ_0 is the coherence length without disorder. Since l is written as $h/e^2k_F\rho$ for a 2D system, where ρ is the resistivity, in a 2D metallic layer with an array of linear resistors at equal interval w as shown in the inset of Fig. 2(a), we found $B_{c2.vicinal}/B_{c2.flat}$ is written as $(1 + \alpha/w)^{-1/2}$, where $\alpha \equiv \rho_{step}/\rho_{terrace}$ is a ratio of step and terrace resistivity. Figure 2(a) shows B_{c2} dependence on the terrace width w obtained from our experimental results including those of 0.5°-tilted vicinal sample. A solid curve is a fitted one with α = 15.4 nm, showing good agreement. Since $l_{flat} \sim 3.3$ nm we estimates $l_\perp$ for 1.1° (0.5°) -tilted vicinal SIC phases is 1.6 (2.3) nm, respectively.

One of the characteristic features of AJV is the suppression of DOS within the gap at the vortex core. According to the calculations of AJV [1], the DOS suppression is described as t^2, where t is the ratio of hopping strength across the step to that within the terrace. Since the width of the elongated vortex core is given by $2\xi_\perp$, vortices on the

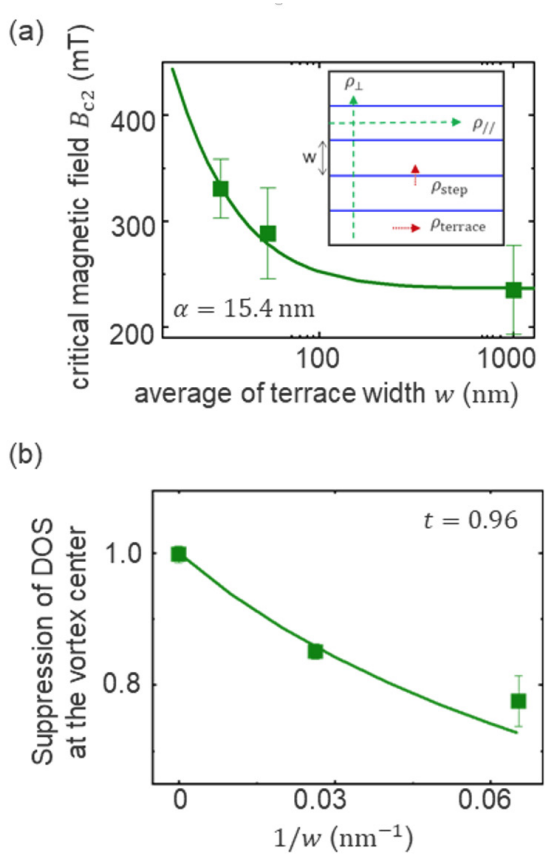

Fig. 2. (a) Terrace width dependence of the critical magnetic field. The solid curve is a fitting described in the text. The inset shows a schematic of the arrayed resistors to model the vicinal SIC phases. (b) terrace width dependence of the suppressed DOS at the vortex center. The solid curve is a fitting written in the text.

vicinal substrates cross the steps $2\xi_\perp/w$ times. The effective hopping strength ratio across the steps is thus given as $t^{2\xi_\perp/w}$. Figure 2(b) shows the terrace width dependence of the suppression factor $t^{4\xi_\perp/w}$. A solid green curve is a fitting one with $\xi_\perp = \xi_{flat}\,(1 + \alpha/w)^{-1/2}$, showing a good agreement when $t = 0.96$. Considering an almost round shape of vortices trapped at a single step of the same SIC phase [1], the estimated value close to 1 is reasonable. We thus conclude that the elongated vortices observed on the vicinal samples are due to the formation of AJV. They are, however, different from ones formed on a single step that have the width of the coherence length. In the vicinal SIC phases, AJV are squeezed in the direction perpendicular to the steps because of the limited mean free path in the direction.

Reference
[1] S. Yoshizawa *et al.*, Phys. Rev. Lett. **113**, 247004 (2014).

Authors
Y. Sato, M. Haze, S. Yoshizawa[a], T. Uchihashi[a], and Y. Hasegawa
[a]National Institute for Materials Science

Thin Film Growth by Energy-Moderated Laser Ablation

Lippmaa Group

Pulsed laser deposition (PLD) is one the most successful thin film growth methods for oxides and other materials with very high melting points. The main merit of PLD is the ability to grow thin films of almost any material for which stoichiometric bulk evaporation sources are available. This universal nature of PLD stems from the near-stoichiometric transfer of material from the source to the film in the laser ablation process. However, despite this universal nature of PLD, it is also generally understood that the highest crystalline quality in thin films can be achieved by molecular beam epitaxy (MBE), rather than PLD. The inferior quality of PLD-grown films often manifests itself in the form of higher defect density, lower carrier mobility in semiconductors, inferior dielectric permittivity compared to bulk crystals, and in systematic shifts of film lattice parameters compared to known bulk reference values. These functional property differences in PLD films can be traced back to stoichiometry shifts in the deposition process and mechanical damage to the film due to the high-energy plasma in the laser ablation plume.

The stoichiometry shift may be related to nonstoichiometric evaporation of different elements from an ablation target, to a difference in the scattering spread of atoms with different weight in the gas phase as the ablation plume expands and interacts with the ambient background gas, or to selective re-evaporation of some atomic species from a film surface at the growth temperature. Depending on which mechanism is responsible, the target composition, ablation laser pulse power density, or the growth temperature and growth rate can be adjusted to correct for the stoichiometry errors.

A more difficult question is how to handle the formation of point defects in the film due to the high kinetic energy of atoms that impinge on the film surface. Time-of-flight measurements have shown that the kinetic energy of atomic species in a laser ablation plume can reach 100 eV, depending on the energy transfer from laser light to the expanding plasma. This energy is sufficient to cause sputtering damage on the film surface and thus leads to the formation of point defects that are not related to any stoichiometry errors. For oxide thin films, such point defect damage can be detected as an expansion of the film lattice compared to known bulk reference value. An effective way to reduce such sputter damage is to reduce the kinetic energy of the plume by introducing a dense background gas. As illustrated in Fig. 1, the position of a $SrTiO_3$ film x-ray diffraction (XRD) peak changes as a function of the ambient oxygen pressure. An overlap of the homoepitaxial film peak with the

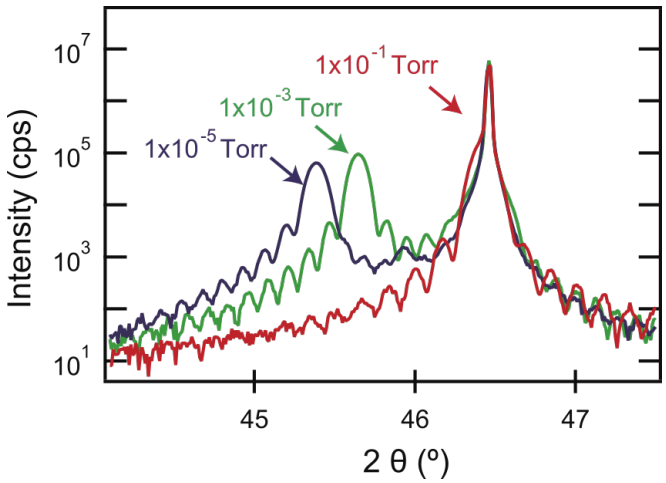

Fig. 1. X-ray diffraction patterns of homoepitaxial $SrTiO_3$ films grown by PLD at several oxygen pressures. The film peaks separate from the substrate position 46.4° due to lattice expansion caused by point defects. An overlap with the substrate is achieved only at very high oxygen pressure (100 mTorr).

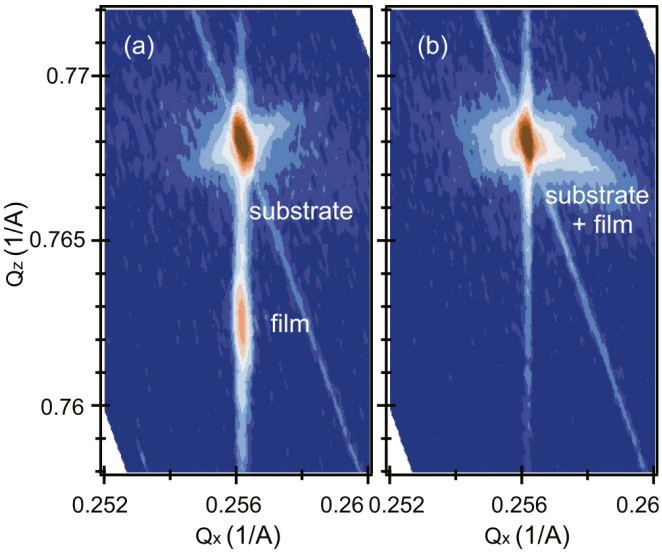

Fig. 2. Reciprocal space maps of homoepitaxial $SrTiO_3$ films grown in (a) 10^{-5} Torr of O_2 and (b) mixture of 10^{-5} Torr O_2 / 600 mTorr He. The film peak exactly overlaps with the substrate peak when the kinetic energy of the plasma plume is moderated by the presence of He in the film growth chamber.

$SrTiO_3$ substrate peak was obtained at 100 mTorr oxygen pressure. Using very high oxygen pressure during film growth is not a good solution because it reduces the deposition rate, may cause gas-phase stoichiometry errors, and degrades the surface flatness of oxide films.

In this work, plasma kinetic energy moderation was therefore done by introducing He gas into the process chamber to a pressure of 600 mTorr [1]. Despite the high pressure, the presence of He does not reduce the deposition rate significantly and allows for independent adjustment of the reactive oxygen pressure while the kinetic energy of the plume can be reduced by an order of magnitude. As the maximum energy of plasma species drops below about 20 eV, sputter damage of the thin film is nearly eliminated. A dramatic change in the film structure can be seen in the reciprocal space maps in Fig. 2. The map shown in panel (a) is for a homoepitaxial $SrTiO_3$ film grown at an oxygen pressure of 10^{-5} Torr. The film diffraction peak is clearly shifted away from the substrate, indicating that the film lattice is strongly expanded. Separate composition analysis showed that the film was very close to stoichiometric and a Sr/Ti ratio error cannot be the cause of the lattice expansion. In contrast, panel (b) shows a map for a film grown in a mixture of 10^{-5} Torr of oxygen and 600 mTorr of He. No separate film peak is visible in this case since the homoepitaxial film peak overlaps exactly with the substrate peak.

High-pressure He in the PLD chamber thus effectively moderates the kinetic energy of the ablation plume and eliminates the sputtering damage of the oxide film. The kinetic energy is a function of the laser peak power and thus depends not only on the pulse energy but also on the pulse length. The kinetic energy moderation is thus an especially important technique for improving thin film quality when a Nd:YAG lasers with a pulse length of close to 4 ns are used for PLD growth of thin films.

Reference

[1] R. Takahashi, T. Yamamoto, and M. Lippmaa, Cryst. Growth. Des. **21**, 5017 (2021).

Authors
R. Takahashi[a], T. Yamamoto[b], and M. Lippmaa
[a]Nihon University
[b]Nagoya University

Functionalization of the MoS_2 Basal Plane for Activation of Molecular Hydrogen by Pd Deposition Studied by Ambient-Pressure X-ray Photoelectron Spectroscopy

Yoshinobu and I. Matsuda Groups

Molybdenum disulfide (MoS_2) is one of the transition-metal dichalcogenides (TMDs) and has a layered structure. The monolayer or multilayer MoS_2 is expected to have various applications such as field-effect transistors, optoelectronic devices, and gas sensors due to the unique optical properties, sufficiently high carrier mobility, and excellent chemical and thermal stability. In addition, MoS_2 has been used as industrial catalysts for many years. For example, the Co-MoS_2/Al_2O_3 catalyst has been industrially used as a hydrodesulfurization catalyst that hydrogenates sulfur contained in crude oil to improve the purity. Thus, the MoS_2 surface is a reaction field for various catalytic reactions involving hydrogen atoms. The dissociative adsorption of hydrogen molecules on MoS_2 surfaces is considered to be a thermally activated process. At room temperature, the basal plane of MoS_2 is inert for the dissociation of molecular hydrogen. Therefore, creating active sites for the hydrogen dissociation on the MoS_2 basal surface is expected to lead to higher efficiency of hydrogenation reactions and hydrogen gas sensors using the MoS_2 crystal.

We investigated the effects of gaseous hydrogen exposure on the bare MoS_2 and Pd-deposited MoS_2 basal surfaces using ambient-pressure X-ray photoelectron spectroscopy [1]. In the Mo 3d core-level, S 2p core-level, and valence-band photoelectron spectra of a bare MoS_2 surface, little change was observed in the energy shift before and after exposure to hydrogen gas. Upon hydrogen gas exposure on the Pd-deposited MoS_2 surface, the Pd 3d XPS spectra changed (Figs. 1(a) and (b)), which can be interpreted as the adsorption of dissociated hydrogen atoms on the Pd sites; each peak in the photoelectron spectra (Mo 3d, S 2p, and valence-band) shifted to a lower binding energy with

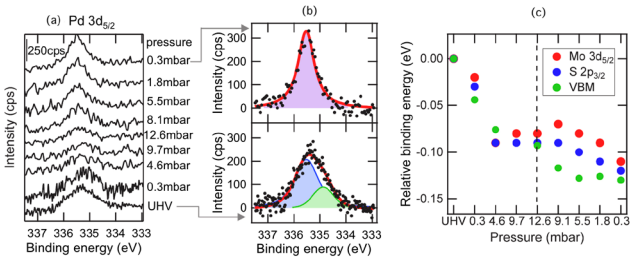

Fig. 1. (a) Pd $3d_{5/2}$ spectra of the Pd/MoS_2 as a function of H_2 gas pressure at 300 K. The amount of deposited Pd was estimated to be 2.0 % for the amount of Mo atoms on the outermost MoS_2 layer. (b) The upper and lower figure are the fitting results for the Pd $3d_{5/2}$ AP-XPS spectra before and after the hydrogen exposure, respectively. The green component and blue component in the lower figure are assigned to be surface and bulk components of the Pd islands, while the pink component would consist of both the bulk component and hydrogen atoms-adsorbed surface component. (c) The relative binding energies for the Mo $3d_{5/2}$ core-level, S $2p_{3/2}$ core-level, and valence band maximum (VBM) as a function of H_2 gas pressure.

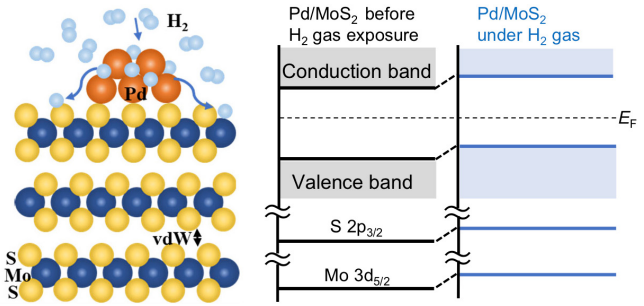

Fig. 2. (Left) The schematic of the dissociation of molecular hydrogen, the adsorption of atomic hydrogen on the Pd-deposited sites on the MoS_2 surface and the spillover of hydrogen atoms onto the MoS_2 surface. (Right) The energy diagram of the Pd-deposited MoS_2 surface before and after hydrogen exposure.

0.1 eV (Fig. 1(c)). When hydrogen gas was evacuated, the peak energy remained lower compared with that before hydrogen gas exposure (Fig. 1(a)). These results indicate that the dissociation of molecular hydrogen and the adsorption of atomic hydrogen occur on the Pd-deposited sites on the MoS_2 surface, and thereafter hydrogen atoms spillover onto the MoS_2 surface. This study shows that the active site for the dissociation of molecular hydrogen is created on an inert MoS_2 basal surface by Pd deposition. In addition, the electronic states of the MoS_2 substrate have been modulated by hydrogen atoms spilled over onto the MoS_2 surface. These processes and the energy diagram are schematically shown in Fig. 2.

Reference
[1] F. Ozaki, S. Tanaka, W. Osada, K. Mukai, M.Horio, T. Koitaya, S. Yamamoto, I. Matsuda, and J. Yoshinobu, Applied Surface Science **593**, 153313 (2022).

Authors
F. Ozaki, S. Tanaka, W. Osada, K. Mukai, M. Horio, T. Koitaya[a], S. Yamamoto[b], I. Matsuda, and J. Yoshinobu
[a]Institute for Molecular Science
[b]Tohoku University

Development of Accurate Density Functional Theory

Sugino Group

Significance of the density functional theory (DFT) is in the ability to obtain the particle density ρ and the energy E without knowing the many-body wave function or the Green's function. Establishing the ρ-to-E mapping (or the functional $E[\rho]$), or equivalently the mapping to the external potential ($V_{\mathrm{ext}}[\rho]$), is a grand challenge of computational materials science. This can be done, in principle, by inverting the V_{ext}-to-ρ relations that are provided by performing extremely-high-precision simulations; but there was no such trial until very recently. Such machine-learning (ML) based approach may be enabled by overcoming problems associated with handling very large dataset. With this in mind, we have previously done accurate quantum chemical simulations of a few molecules and the resulting density-to-energy relation was modeled with the neural network technique. The functional thus developed was found to improve the accuracy of molecular calculations showing a promise of achieving the chemical accuracy with DFT; however, application to solids was hampered by the fact that the molecular ρ is qualitatively different from the solid-state ρ and the non-availability of accurate ρ for solid states. In this context, we have shown that the insufficient information contained the molecular ρ can be augmented by adding the theoretically established ρ-to-E relations that hold for general ρ. To demonstrate this, we have reconstructed the functional using the theoretical relations as constraints of ML. The functional was developed using a semilocal functional format, called meta-generalized-gradient-approximation (meta-GGA), where the density, gradient of the density, and the kinetic energy density are used as the descriptor. By applying thus-established functional ($V_{\mathrm{ext}}[\rho]$) to various crystalline solids, we have shown improved predictability of the lattice parameters. The functional was made public for the benefit of supercomputer uses [1].

Further improvement in the accuracy is most likely to be brought by using more sophisticated descriptors, such as the weighted densities. To get insights into it, classical systems provide a suitable benchmark because of the simple structure as compared to quantum systems. In this context, we investigated the structure of classical fluids of Lennard-Jones particles. In the classical systems, the density to the free-energy mapping can be rigorously described through the Bogoliubov-Born-Green-Kirkwood-Yvon (BBGKY) hierarchical equations and establishing the mapping corresponds to finding a universal closure relation, or simply a closure, that can appropriately truncate the hierarchy. To investigate it, we used the method of adiabatic continuation of the interaction and the scheme of functional renormalization group (FRG). We have obtained this way the flow equation that is suitable for deriving a working equation for numerical work. We focused herein on the Kirkwood super-

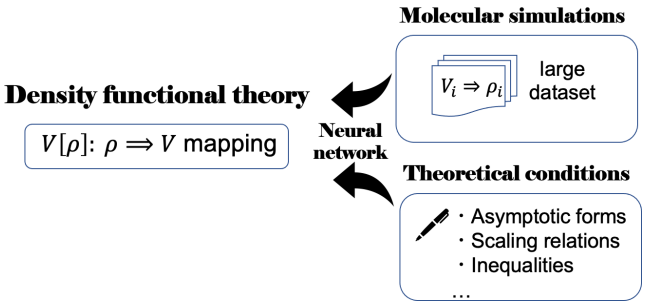

Fig. 1. Machine learning of the density functional $V[\rho]$ made possible using combined molecular data and theoretical conditions. The functional thus constructed can be applied to extended systems like solids not included in the learning set.

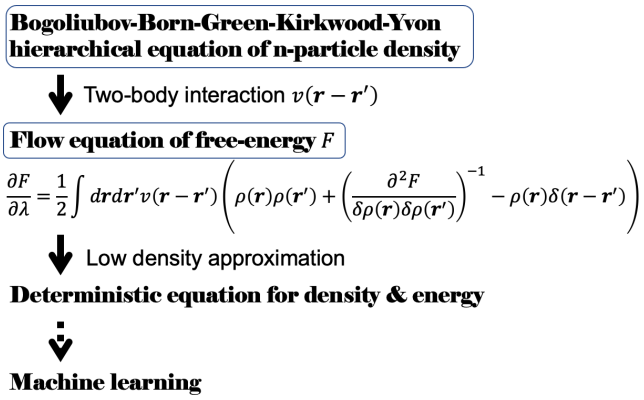

Fig. 2. Density functional theory for classical systems. Flow equation suitable for numerical work was developed to be used for the machine learning of the density-to-free energy mapping.

position with which to decompose the n-particle density into two-particle densities, which is strikingly accurate in the low-density region. By applying the resulting equation to a one-component one-dimensional fluid, we found it possible to obtain accurate density and energy when compared with other liquid theories. This result is already a demonstration of the power of the Kirkwood approximation combined with FRG in describing classical liquids, but more importantly, the resulting method has a form suitable for ML and thus encourages future work on the construction of the functional [2].

References

[1] R. Nagai, R. Akashi, and O. Sugino, npj Compt. Mater. **6**, 1 (2020); *ibid*, Phys. Rev. Res. **4**, 013106 (2022).
[2] T. Yokota, J. Haruyama, and O. Sugino, Phys. Rev. E **104**, 014124 (2021).

Authors

R. Nagai, [a]R. Akashi, [b]T. Yokota, and O. Sugino
[a]National Institute for Quantum Science and Technology
[b]Interdisciplinary Theoretical and Mathematical Science Program, RIKEN.

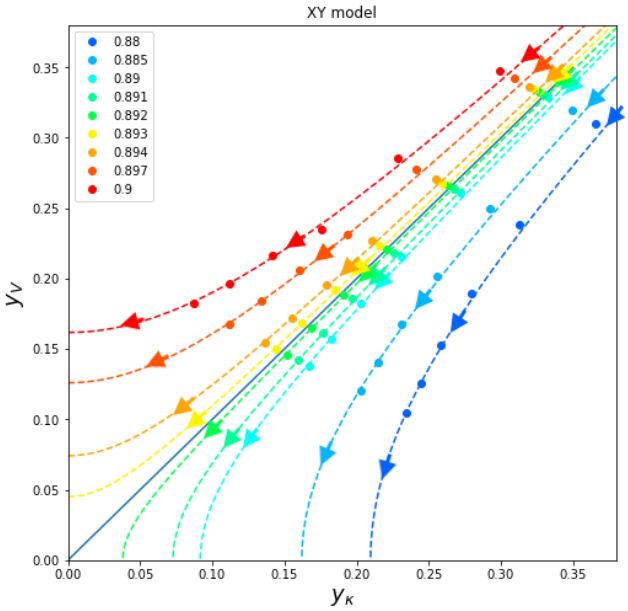

Fig. 2. The Renormalization-Group flow for the BKT transition in the classical two-dimensional XY model, constructed numerically from the transfer matrix spectrum based on the combination of tensor-network renormalization and conformal field theory.

Resolving the Berezinskii-Kosterlitz-Thouless Transition in the Two-Dimensional XY Model with Tensor-Network-Based Level Spectroscopy

Oshikawa Group

The Berezinskii-Kosterlitz-Thouless (BKT) transition was historically the first example of topological phase transitions, which is now an essential concept in physics as signified by the Nobel Prize in Physics in 2016. The canonical model exhibiting the BKT transition is the classical XY model in two dimensions. The BKT transition is conceptually well understood in terms of the Kosterlitz Renormalization Group (RG) equation. However, the famous "Kosterlitz RG flow" has remained a rather abstract concept, which cannot be seen directly. Moreover, because of the notorious logarithmic corrections, significant finite-size effects persist even in a large system, making conventional finite-size scaling of Monte Carlo methods such as Binder plot powerless. Even with considerable efforts over decades, an accurate determination of the critical temperature remains difficult, even with a huge computational power, for the system as simple as the classical XY model in two dimensions.

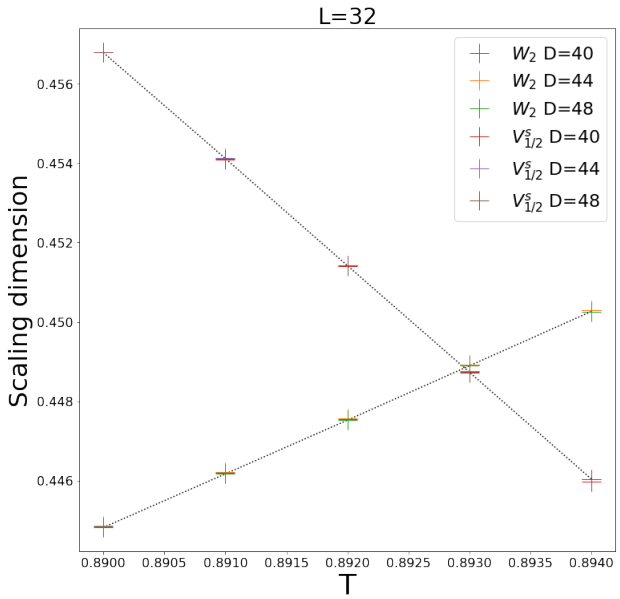

Fig. 1. The "level spectroscopy" applied to the classical two-dimensional XY model with the tensor-network renormalization. The crossing of the two "energy levels" (eigenvalues of the transfer matrix) in a finite-size system gives a precise estimate of the BKT transition temperature, as the logarithmic correction is cancelled out.

On the other hand, many one-dimensional quantum systems can be also described by the same effective theory and thus also exhibit the BKT transition. Interestingly, a powerful numerical finite-size scaling method called "level spectroscopy" was developed specifically for those 1D quantum systems by Okamoto and Nomura. Based on the conformal field theory results on the finite-size energy spectrum thanks to Cardy, they found that the BKT transition can be identified with a level crossing between a certain pair of the energy levels, canceling the logarithmic corrections. This allows a surprisingly accurate determination of the BKT transition point with exact numerical diagonalization of rather small systems. However, the applications of level spectroscopy have been limited to one-dimensional quantum BKT system such as quantum spin chains so far. While it should be applicable to the spectrum of the transfer matrix for the classical two-dimensional XY model, the level spectroscopy has not been applied there, because of the difficulty in calculating the spectrum for the system with continuous variables such as the angle of the XY spin.

In this work, we demonstrated a successful implementation of level spectroscopy on the classical two-dimensional XY model, based on the tensor network renormalization (TNR) scheme. The TNR enables us to obtain a precise spectrum of the transfer matrix, to which the level spectroscopy can be applied. As in the case of the one-dimensional quantum system, it allows a very accurate determination of the critical point by removing the logarithmic corrections from systems of moderate sizes, which can be described by a tensor network with a finite bond dimension. As a result, we have improved the accuracy of the BKT transition tempera-

ture in the classical two-dimensional XY model, by an order of magnitude over the best numerical estimate in the literature.

Furthermore, our TNR study covers larger system sizes than those in the existing level spectroscopy studies on one-dimensional quantum systems. We found a new feature of the finite-size scaling, that leads to a further improvement of level spectroscopy. Finally, we also applied our methodology to visualize the celebrated Kosterlitz RG flow of the BKT transition based on the numerical data, for the first time to our knowledge.

Reference
[1] A. Ueda and M. Oshikawa, Phys. Rev. B **104,** 165132 (2021). [Editor's Suggestion]

Authors
A. Ueda and M. Oshikawa

Large Anomalous Nernst Effect and Nodal Plane in an Iron-Based Kagome Ferromagnet

Nakatsuji Group

Anomalous Nernst effect (ANE), a thermoelectric effect in magnetic material, has recently attracted attention as unique energy-harvesting technology. It holds promise in developing high-efficiency energy-harvesting devices with a simple lateral structure, high flexibility, and low production cost. The design of magnetic materials that exhibits a large ANE will help develop a novel energy harvesting technology. Here, we observed a high ANE exceeding 3 μV/K above room temperature in the kagome ferromagnet Fe_3Sn with a high Curie temperature of 760 K [1].

Figure 1a shows the temperature dependence of anomalous Nernst coefficient S_{ij} and transverse thermoelectric conductivity α_{ji}. With increasing temperature up to 400 K, the magnitude of the ANE coefficient increases monotonically and reaches 3 μV/K above room temperature. The temperature dependence of α_{ij}/T exhibits logarithmic behavior over almost a decade of temperature from 400 K down to 40 K, and remains roughly constant at ˜0.02 $Am^{-1}K^{-2}$ below ˜40 K (Fig. 1b). The logarithmic behavior of α_{ij}/T signals a nontrivial electronic structure close to the Fermi energy.

To investigate the origin of ANE, we carried out first-principles calculations to analyze α_{ij}, and the calculated result agrees well with the experimental data (Fig. 1b). We then conclude that the origin of the ANE is a pair of partially flat

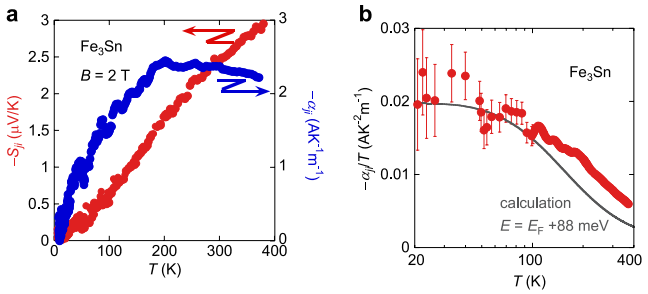

Fig. 1. (a) Temperature dependence of the Nernst signal (S_{ji}) and the transverse thermoelectric conductivity (α_{ij}) measured under an external magnetic field of 2 T. (b) Temperature dependence of the transverse thermoelectric conductivity (α_{ji}/T). The dark line represents α_{ji}/T obtained by DFT calculation at E_F = +88 meV.

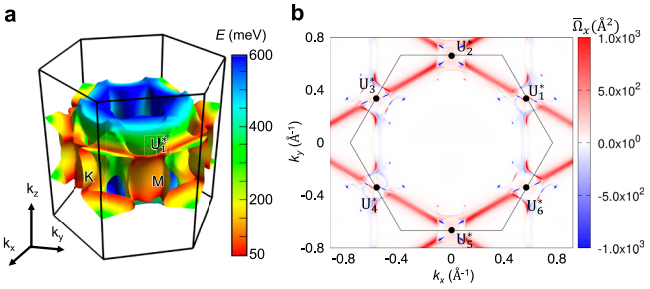

Fig. 2. (a) Nodal plane in the hexagonal Brillouin zone obtained as follows: $\Delta\varepsilon(\boldsymbol{k}) \equiv \varepsilon^{\alpha}(\boldsymbol{k}) - \varepsilon^{\beta}(\boldsymbol{k}) = 0$, where $\Delta\varepsilon(\boldsymbol{k})$, $\varepsilon^{\alpha(\beta)}(\boldsymbol{k})$, and $\boldsymbol{k}$ are the energy difference between two bands, eigenvalue for up- and down-spin bands, and wave vector, respectively. The color bar shows the energy of the nodal plane calculated without SOC. (b) Contour plot of the sum of the Berry curvature over the occupied states ($E = E_F + 50$ meV) on $k_z = 0.13$ plane.

bands of up- and down-spins, known as the "nodal plane" (Fig. 2a). Indeed, strong intensity of the Berry curvature arising from the flat nodal plane appears at specific chemical potentials (Fig. 2b). Similar to the nodal lines, nodal planes are ubiquitous in electronic band structures without SOC. Nodal planes often turn into nodal lines at constant energy cuts, and these constant energy lines lead to partially flat bands with a small energy gap after introducing SOC. Such characteristic band structure is not unique to Fe_3Sn and could be realized in other kagome lattice materials. It is well known that M points in kagome lattice may result in van Hove singularities (namely, the derivative of energy dispersion is zero). Therefore, energy dispersion on lines connecting M points could be flat compared with other k paths. Our theoretical analysis based on the first-principles calculation clarifies that a "nodal plane" induces strongly enhanced Berry curvature, resulting in the large ANE. The flat degenerate electronic bands provide a valuable guide to designing magnetic materials with a large ANE.

Reference
[1] T. Chen, S. Minami, A. Sakai, Y. Wang, Z. Feng, T. Nomoto, M. Hirayama, R. Ishii, T. Koretsune, R. Arita, and S. Nakatsuji, Sci. Adv. **8**, eabk1480 (2022).

Authors
T. Chen, S. Minami[a], A. Sakai, Y. Wang[a], Z. Feng, T. Nomoto[a], M. Hirayama[b], R. Ishii, T. Koretsune[c], R. Arita[a,b], and S. Nakatsuji
[a]The University of Tokyo
[b]RIKEN Center of Emergent Matter Science (CEMS)
[c]Tohoku University

Anomalous Scaling Behavior of Transverse Thermoelectric Conductivity in Ferromagnet CoMnSb

Nakatsuji Group

Transverse transport effects such as anomalous Hall and Nernst effects are effective probes to topological texture in electronic band structures. In particular, large Berry curvature originating from Weyl nodes or nodal line structures is known to enhance these effects significantly. In contrast to the Hall conductivity σ_{yx}, which measures the summation of the Berry curvature below Fermi energy, the transverse thermoelectric conductivity α_{yx} sensitively captures the Berry curvature in the vicinity of the Fermi energy [1]. Therefore, the Nernst effect provides complementary information about the characteristics of the topological band structure. Moreover, scaling behavior $\alpha_{yx} \sim -T \log T$ is recently reported

in ferromagnet Co_2MnGa [2]. This anomaly is attributed to the Weyl semimetal state tuned close to the quantum Lifshitz critical point. However, the universality of this critical behavior is still yet to be confirmed experimentally.

Here, we report magnetic, transport, and thermoelectric properties of single crystals of ferromagnetic CoMnSb with a high Curie temperature of 470 K [3]. The actual experimental crystal structure of CoMnSb is a $2\times2\times2$ superstructure of the previously predicted half-Heusler structure. Since theoretical understanding of the transverse transport phenomena in the superstructure CoMnSb is lacking, we performed first-principles calculation of superstructure CoMnSb to compare with experimental results.

We find a sizable anomalous Hall conductivity σ_{yx} and transverse thermoelectric conductivity α_{yx} experimentally. We observe substantial anomalous Hall conductivity σ_{yx} and transverse thermoelectric conductivity α_{yx}. The experimental σ_{yx} (T) is well described by DFT calculation for the chemical potential E - $E_F \approx$ -130 meV (Fig. 1(a)), which is consistent with the valence electron count estimated from the sample composition measured by Inductively Coupled Plasma (ICP) method. Moreover, α_{yx} exhibits $-T\log T$ cr itical behavior instead of the conventional Fermi liquid behavior $\alpha_{yx} \sim T$ over a decade of temperature between 10 and 400 K (Fig. 1(b)). This behavior is similar to ferromagnetic Weyl semimetal Co_2MnGa and nodal-line semimetals Fe_3X (X = Al, Ga) [2, 5]. Our theoretical calculation shows that in the vicinity of the chemical potential E - $E_F \approx$ -130 meV, the scaling behavior $\alpha_{yx} \sim -T\log T$ arises from Weyl nodes in the band structure (Fig. 2).

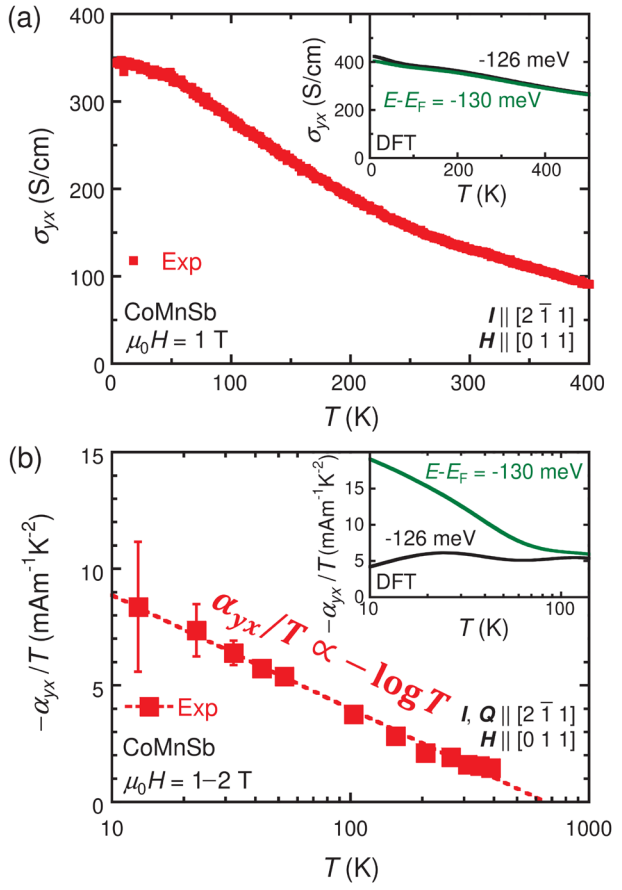

Fig. 1. Temperature T dependence of (a) the Hall conductivity σ_{yx}, and (b) the transverse thermoelectric conductivity divided by T, α_{yx} / T in comparison with theoretical calculations (insets) for CoMnSb. Two different chemical potentials, E - E_F = -126 meV (black) and E - E_F = -130 meV (green), are selected for calculating σ_{yx} (T) and α_{yx} (T) / T.

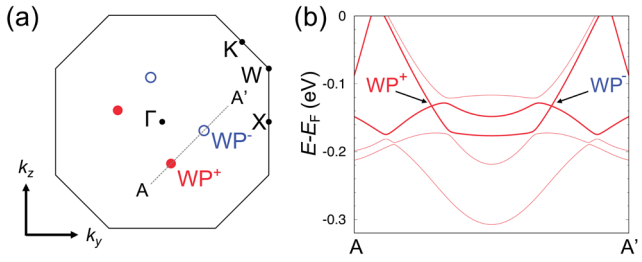

Fig. 2. (a) Momentum-space distribution of Weyl nodes in CoMnSb on the k_x = 0 plane, which shows the Weyl node pair WP$^-$ (open blue circle) and WP$^+$ (closed red circle). The coordinate of WP$^-$ and WP$^+$ (k_y, k_z) are (0.21, -0.04) and (0.04, -0.21) in the unit of angstrom inverse, respectively. Black solid lines correspond to the boundary of the fcc Brillouin zone. (b) Band structure along A--A' (the black-dotted line) shown in (a).

In summary, we have successfully synthesized single-crystal samples of superstructure CoMnSb and explored their transverse transport properties. The observed critical scaling behavior in the transverse thermoelectric conductivity $\alpha_{yx} \sim -T\log T$ clearly deviates from the conventional Fermi liquid behavior, providing a hallmark of topological texture in the band structure. The comparison of experimental results with DFT calculations shows that this critical behavior results from Weyl nodes. This result indicates that the logarithmic criticality in the transverse thermoelectric conductivity provides a highly sensitive signature to reveal the topological band texture.

References

[1] G. Sharma, P. Goswami, and S. Tewari, Phys. Rev. B **93**, 035116 (2016).
[2] A. Sakai *et al.*, Nat. Phys. **14**, 1119 (2018).
[3] H. Nakamura *et al.*, Phys. Rev. B **104**, L161114 (2021).
[4] S. Minami *et al.*, Appl. Phys. Lett. **113**, 032403 (2018).
[5] A. Sakai *et al.*, Nature **581**, 53 (2020).

Authors

H. Nakamura, S. Minami[a], T. Tomita, A. A. Nugroho[b], and S. Nakatsuji
[a]The University of Tokyo
[b]Institut Teknologi Bandung

Phonon Spectrum of Quantum Pyrochlores $Pr_2Zr_2O_7$ and $Pr_2Ir_2O_7$

Nakatsuji Group

Experimental realization of a quantum spin liquid (QSL) state is among the central topics of condensed matter physics. In a QSL state, spins do not form long-range order even down to absolute zero, characterized by strong long-range entanglement[1]. Geometric frustrations and competing interactions are central ingredients to realizing QSL states. However, almost all candidate materials discovered possess chemical or structural disorders. Thus, it is crucial to understand the role of structural disorders. Can structural disorder be a factor that stabilizes a QSL state, as proposed in some theoretical studies [2]? How to experimentally distinguish the effects of structural disorders from that induced by the intrinsic lattice dynamics?

To answer these questions, we performed Raman scattering spectroscopy to separate dynamic lattice effects from the structural disorders on the Pr-based pyrochlore oxides $Pr_2Zr_2O_7$ and $Pr_2Ir_2O_7$[3,4]. Both materials host exotic ground states without long-range orders. Their CEF

ground state is an E_g non-Kramers doublet, which is unprotected by the time-reversal symmetry and thus can be split by a slight deviation from the D_{3d} local symmetry. As a result, structural disorders may play an essential role in shaping the ground-state properties of both systems.

Our Raman studies reveal that splitting of the ground state E_g doublet and the E_g doublet at 55 meV results from different physical origins [3]. Figures 1(a) and (b) show the Raman spectra of CEF excitation and the CEF level scheme of $Pr_2Zr_2O_7$ at 14 K, respectively. The E_g level at 55 meV is split by the T_{2g} phonons instead of structural disorder. The observed splitting characterized by a well-defined symmetry can only occur in the presence of mixing with another excitation of E symmetry, leading to a vibronic state (Fig. 1(c)). Based on DFT calculations, the vibronic state in $Pr_2Zr_2O_7$ is most likely driven by T_{2g} phonon lying at 64.6 meV at the Γ point (Fig. 1(d)). The associated eigenvectors involve motion of O1 oxygens that modulates the Pr^{3+} oxygen environment (Fig. 1(e)).

Our second study [4] reveals that $Pr_2Zr_2O_7$ exhibits phonon softening, which modulates the Pr-O-Pr angle and changes the magnetic super-exchange interaction. Compared to $Pr_2Zr_2O_7$, $Pr_2Ir_2O_7$ shows a similar but much broader phonon spectrum (Fig. 2). Given that the metallic $Pr_2Ir_2O_7$ features phonon-electron scattering mechanisms, which are absent in the insulating $Pr_2Zr_2O_7$, the difference in their phonon spectrum is likely a result of phonon-electron scattering rather than disorders.

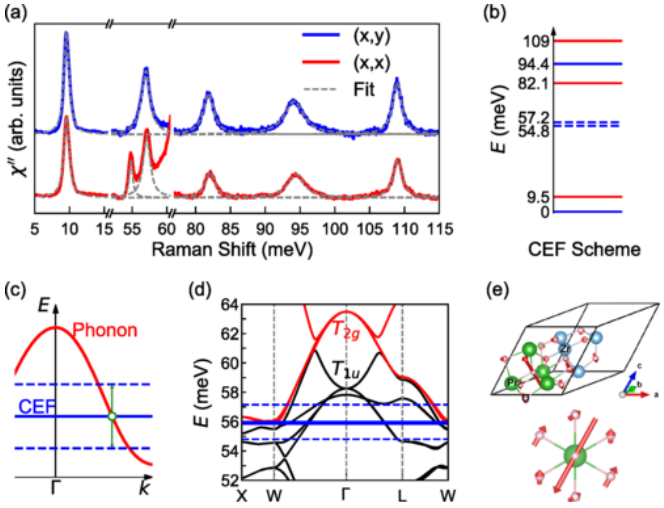

Fig. 1. (a) Raman spectra of $Pr_2Zr_2O_7$ at 14 K. (b) A schematic diagram of the Pr^{3+} CEF levels in $Pr_2Zr_2O_7$. (c) A schematic diagram of the vibronic coupling between the phonons and CEF states. (d) The $Pr_2Zr_2O_7$ phonon dispersion obtained by DFT calculations. The energy range close to the vibronic features is shown. Dashed blue lines represent the experimentally observed CEF vibronic excitations. The vibronic coupling is expected to occur at the intersection point of the nonsplit CEF doublet (solid blue line) and the T_{2g} phonon branch (red curve). (e) Atomic displacements of the T_{2g} phonon mode. Upper panel: View of the unit cell. Lower panel: PrO_8 octahedron site viewed from the [111] direction.

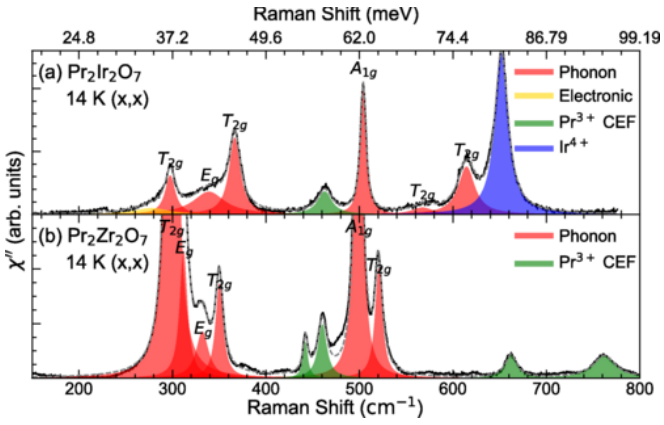

Fig. 2. Raman scattering spectra of (a) $Pr_2Ir_2O_7$ and (b) $Pr_2Zr_2O_7$ at 14 K in parallel polarization configuration.

References

[1] P.W. Anderson, Mat. Res. Bull. **8**, 153 (1973).
[2] L. Savary and L. Balents, Phys. Rev. Lett. **118**, 087203 (2017).
[3] Y. Xu, H. Man, N. Tang, T. Ohtsuki, S. Baidya, S. Nakatsuji, D. Vanderbilt, and N. Drichko, Phys. Rev. B **89**, 075137 (2022).
[4] Y. Xu, H. Man, N. Tang, S. Baidya, H. Zhang, S. Nakatsuji, D. Vanderbilt, and N. Drichko, Phys. Rev. B **104**, 075125 (2021).

Authors

Y. Xu[a], H. Man[a], N. Tang, T. Ohtsuki, S. Baidya[b], S. Nakatsuji, D. Vanderbilt[b], and N. Drichko[a], and H. Zhang[b]
[a]John Hopkins University
[b]Rutgers University

Ferrimagnetic Compensation and its Thickness Dependence of TbFeCo Alloy Thin Films

Nakatsuji Group

Rare earth (RE)-transition metal (TM) ferrimagnetic materials have compositions in which the antiferromagnetically coupled magnetization of RE and TM atoms compensates, resulting in a zero net magnetization. Tuning magnetization to zero is particularly advantageous in creating efficient memory devices based on magnetic materials. Moreover, such materials exhibit bulk perpendicular magnetic anisotropy (PMA), whose origin is different from the interfacial PMA. This property offers another advantage for applications. This study reports a systematic investigation into the magnetic properties of ferrimagnetic TbFeCo thin films deposited on a Pt underlayer. Our results show that the Tb concentration, at which magnetic moments of Tb and Fe or Co sublattices are compensated, increases with the thickness of TbFeCo thin films because the Tb atoms are magnetically inert as they are mixed with the Pt underlayer (Fig. 1). Furthermore, we clarify the relationship between the loss of magnetism of Tb atoms and bulk PMA. This study provides a prospect for designing ferrimagnetic ultrathin films with large PMA, which is essential for fabricating magnetic memory devices.

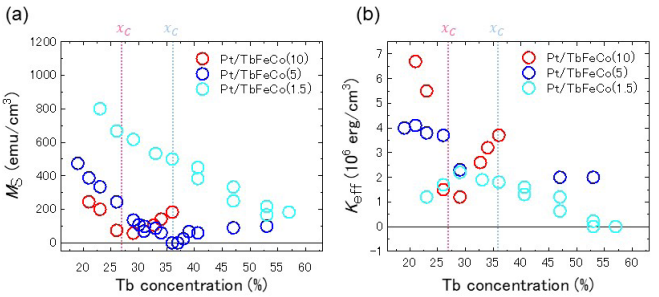

Fig. 1. (a) and (b) Tb concentration dependence of the saturation magnetization M_S (a) and the effective magnetic anisotropy energy density K_{eff} (b) for TbFeCo thin films with different thicknesses. The underlayer is Pt. Red circles: Pt/TbFeCo(10 nm), blue circles: Pt/TbFeCo(5 nm), and light blue circles: Pt/TbFeCo(1.5 nm). Red and blue broken vertical lines denote the compensation composition x_c for Pt/TbFeCo(10 nm) and Pt/TbFeCo(5 nm), respectively.

Reference
[1] M. Ishibashi, K. Yakushiji, M. Kawaguchi, A. Tsukamoto, S. Nakatsuji, and M. Hayashi, Appl. Phys. Lett. **120**, 022405 (2022).

Authors
M. Ishibashi[a], K. Yakushiji[b], M. Kawaguchi[a], A. Tsukamoto[c], S. Nakatsuji[a, d, e, f], and M. Hayashi[a, e]
[a]The University of Tokyo
[b]National Institute of Advanced Industrial Science and Technology
[c]Nihon University
[d]CREST, Japan Science and Technology Agency
[e]Trans-scale Quantum Science Institute, University of Tokyo
[f]Johns Hopkins University

Enhanced Anomalous Hall Signal by Electrical Manipulation in Antiferromagnetic Weyl Metal Mn_3Sn

Nakatsuji, Otani, and Miwa Groups

Topological properties may play a significant role in developing next-generation electronic devices. Weyl semimetals characterized by linearly dispersive band touching points may exhibit surprisingly large topological transport responses, such as anomalous Hall effect (AHE), anomalous Nernst effect (ANE), and chiral anomaly. Manipulation of such topological responses electrically may lead to a new type of nonvolatile memory device.

Recently, electrical manipulation of topological responses for a magnetic Weyl semimetal has been demonstrated. Magnetic switching using spin-orbit torque (SOT) is established in the antiferromagnet Mn_3Sn (Fig. 1(a)) [1]. Figure. 1b shows the schematic of the electrical switching in Mn_3Sn/W memory devices. The polarization of the flowing current determines the orientation of the magnetization of Mn_3Sn. The different states of Mn_3Sn can be read by measuring the Hall voltage, namely "0" and "1" states. For application purposes, it is essential to develop means to enhance the readout signal of the magnetic switching in Mn_3Sn. Several ingredients determine the signal's magnitude, such as geometrical factors of a memory cell, shunting current, and volume fraction of the switching domain. While the former two are extrinsic and tunable by changing the magnetic cell and layer structure, the latter is intrinsic to the cell that consists of a multilayer stack.

This work optimizes the multilayer structure and deposition process and realizes a three-time enhancement of the readout signal (Hall resistance). The Ru buffer layer is removed from the reported Ru/Mn_3Sn/W layer to decrease the current shunting effect, and the Mn_3Sn/W bilayer is directly deposited on the Si/SiO_2 substrate. Moreover, additional annealing progress at the Mn_3Sn/W interface is applied to suppress the roughness at the Mn_3Sn /W interface; as a result, the roughness is decreased to 0.5 nm, one order of magnitude smaller than that of the reported Ru/Mn_3Sn/W thin film.

The obtained AHE signal of the Mn_3Sn/W thin film is twice larger than the previous value reported for Ru/ Mn_3Sn /W thin film. Based on the X-ray diffraction analysis, both the decreased current shunting effect and the different orientation of Mn_3Sn domains contribute to the enhancement of the AHE signal. In the current switching measurement, the switching volume fraction calculated by the ratio between electrical and field switching signals is 50%, around 1.5 times larger than the reported value. The enhancement of the switching fraction is likely related to the higher spin injection efficiency at the interface due to the smooth interface. The enhancement of AHE and the switching fraction result in a three-time enhancement of the switching Hall resistance (Fig. 1(c)). This finding may bring memory devices based on topological antiferromagnet closer to real-world applications [2].

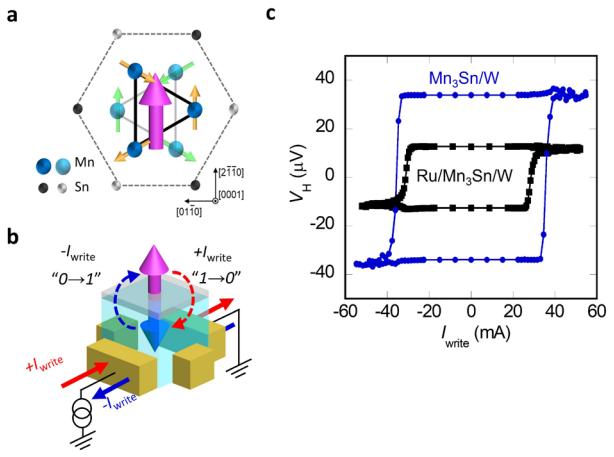

Fig. 1. (a) Crystal and spin structures of Mn_3Sn. The non-collinear spin structure consisting of six Mn magnetic moments (yellow and green arrows) can be viewed as the ferroic ordering of a magnetic octupole (purple arrow). (b) The schematic of the electrical switching in Mn_3Sn/W memory devices. Two different states of Mn_3Sn, "0" and "1" states, can be determined by the polarity of applying current. (c) Enhancement of the switching Hall voltage in the Mn_3Sn/W bilayer is three times larger than the value observed in the previous Ru/Mn_3Sn/W multilayer.

References
[1] H. Tsai, T. Higo, K. Kondou, T. Nomoto, A. Sakai, A. Kobayashi, T. Nakano, K. Yakushiji, R. Arita, S. Miwa, Y. Otani, snd S. Nakatsuji, Nature **580**, 608 (2020).
[2] H. Tsai, T. Higo, K. Kondou, S. Sakamoto, A. Kobayashi, T. Matsuo, S. Miwa, Y. Otani, and S. Nakatsuji, Small Sci. **1**, 2000025 (2021).

Authors
H. Tsai, T. Higo, K. Kondou[a], S. Sakamoto, A. Kobayashi, T. Matsuo, S. Miwa, Y. Otani, and S. Nakatsuji
[a]RIKEN CEMS

Observation of Spontaneous X-ray Magnetic Circular Dichroism in the Chiral Antiferromagnet Mn_3Sn Thin Film

Miwa and Nakatsuji Groups

Antiferromagnets without a net magnetic moment are invisible to many magnetic probes, including X-ray magnetic circular dichroism (XMCD). Recently, it was proposed that the inverse triangular spin (ITS) structure of a noncollinear antiferromagnet can give rise to finite XMCD signals through the non-vanishing magnetic dipole term T, which is probed by XMCD, even without net magnetization [1,2], as schematically shown in Fig. 1(a).

A chiral antiferromagnet Mn_3Sn with the $D0_{19}$ structure [3] is an ideal material for observing the XMCD signals originating from the ITS structure (also referred to as the ferroic order of cluster magnetic octupoles) because the direction of the ITS structure or the octupole polarization can be controlled by external magnetic fields through finite spin canting.

In the present study, to test if finite XMCD signals are observable in the ITS structure, we grew a Mn_3Sn epitaxial

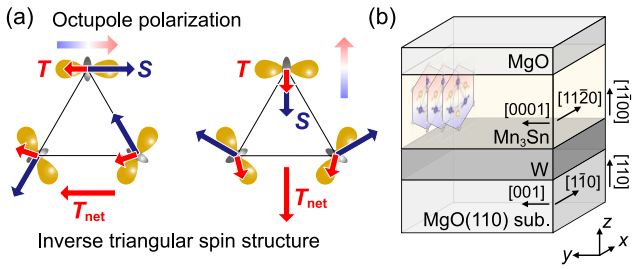

Fig. 1. (a) Inverse triangular spin (*S*) structure with magnetic dipole term (*T*). (b) Thin film structure.

thin film and performed XMCD measurements on it. The sample structure was MgO(110) substrate/W (15 nm)/ Mn_3Sn (40 nm)/MgO (3 nm), as schematically shown in Fig. 1(b). X-ray absorption spectroscopy (XAS) and XMCD measurements were performed on the BL-16A2 beamline at the Photon Factory. Measurement temperature was room temperature. The incident x-ray and magnetic field directions were perpendicular to the sample surface so that the octupole polarization becomes parallel to the incident x-rays.

Figure 2(a) shows a typical XAS spectrum of the Mn_3Sn thin film. The XAS spectral line shape did not depend on the magnetic field strength or direction. The XMCD spectra obtained with magnetic fields of 0.1 T and 5 T are shown by the red and blue curves in Fig. 2(b), respectively. The spectral line shapes significantly differ from each other: The spectrum obtained with 0.1 T shows a strong positive pre-edge peak, denoted by α in Fig. 2(b), while the spectrum obtained with 5 T shows an intense negative peak at the XAS peak position, denoted by β in Fig. 2(b).

The XMCD spectra are expected to consist of the spin-canting component, which develops with increasing magnetic fields, and the field independent octupole component. Because the peak β develops with increasing magnetic fields, it most likely originates from spin canting. Indeed, if the spectrum taken with 0.1 T is subtracted from the spectrum taken with 5 T, a broad featureless XMCD spectrum without peak α is obtained, as shown by the green curve in Fig. 2(b). This broad spectrum resembles the XMCD spectra of metallic systems, suggesting that it reflects the spin component. This argument also indicates that the spectrum taken with 0.1 T, which shows multiple sharp peaks, predominantly reflects the octupole component because it is independent of magnetic fields.

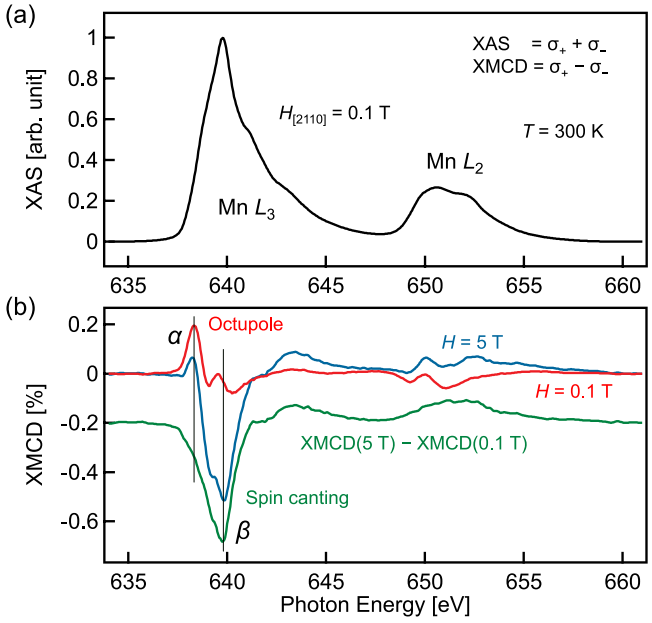

Fig. 2. (a) Typical XAS spectrum of the Mn_3Sn thin film. (b) XMCD spectra taken with magnetic fields (*H*) of 0.1 T (red curve) and 5 T (blue curve). The spin canting component (green curve) is extracted by subtracting the 0.1 T spectrum from the 5 T spectrum.

In summary, we demonstrated that the ITS structure can give rise to finite XMCD signals by performing XMCD measurements on a Mn_3Sn epitaxial thin film [4]. This finding should allow one to quantitatively evaluate the magnitude of the octupole polarization and spin canting, which would be difficult otherwise. The present results should also lead to the resolution of antiferromagnetic domains and antiferromagnetic domain walls using the scanning XMCD technique.

References
[1] Y. Yamasaki, H. Nakao, and T.-h. Arima, J. Phys. Soc. Jpn **89**, 083703 (2020).
[2] N. Sasabe, M. Kimata, and T. Nakamura, Phys. Rev. Lett. **126**, 157402 (2021).
[3] S. Nakatsuji, N. Kiyohara, and T. Higo, Nature **527**, 212 (2015).
[4] S. Sakamoto, T. Higo, M. Shiga, K. Amemiya, S. Nakatsuji, and S. Miwa, Phys. Rev. B **104**, 134431 (2021).

Authors
S. Sakamoto, T. Higo, M. Shiga, K. Amemiya[a], S. Nakatsuji, and S. Miwa
[a]KEK

Electron-Correlation-Driven Enhancement of Orbital Polarization at the Fe/MgO Interface

Miwa Group

Utilizing electron spins in electronic devices is a central theme in the field of spintronics. The giant tunneling magnetoresistance (TMR) effect and interfacial perpendicular magnetic anisotropy (PMA) in Fe/MgO-based multilayer systems are the foundation of such spintronics applications. For both effects, the atoms located at the interface play crucial roles. That is, the interfacial spin and orbital polarization determines TMR and PMA, respectively. Therefore, it is essential to understand how Fe atoms behave at the interface with MgO by characterizing their spin and orbital magnetic moments to further improve TMR and PMA.

For such a purpose, we performed depth-resolved x-ray magnetic circular dichroism (XMCD) measurements on the V/Fe/MgO trilayer grown on an MgO(001) substrate (Fig. 1(a)) The trilayer showed PMA, as confirmed by magneto-optical Kerr effect measurements with out-of-plane magnetic fields (Fig. 1(b)). The principle of the depth-resolved XMCD [1] is shown in Fig. 1(c). Here, photoelectrons emitted at different angles were detected separately. Because electrons have a finite inelastic mean free path λ_e in solids, the probability of inelastic electrons at depth z escaping into the vacuum depends on the electron emission angle θ_d. Therefore, detecting electrons as a function of θ_d yields probing depth (λ_{eff}) dependent XMCD spectra and hence the depth profiles of the spin and orbital magnetic moments. The depth-resolved XMCD measurements were conducted at the beamline BL-7A at the Photon Factory.

The obtained spin and orbital magnetic moments were plotted against the detection angles in Figs. 2(a) and 2(b),

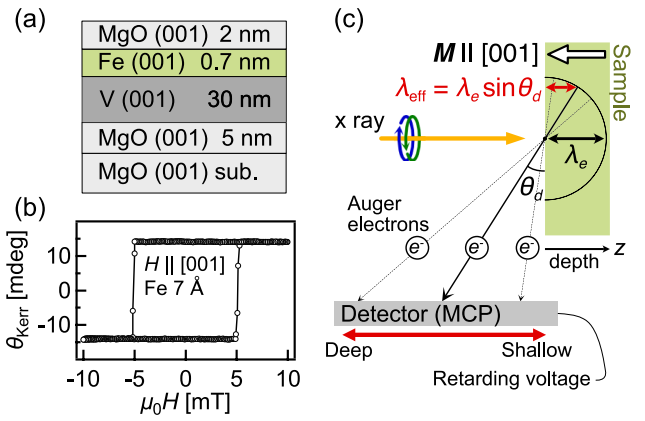

Fig. 1. (a) Sample structure. (b) Out-of-plane magnetization curve measured based on the magneto-optical Kerr effect. (c) Schematic illustration of experimental setup and principle of depth-resolved XMCD technique, where probing depth (λ_{eff}) depends on the electron emission angle (θ_d).

respectively. Both the spin and orbital magnetic moments increased as the detection angles decreased, suggesting that they enhanced near the Fe/MgO interface. By performing curve fitting, we estimated the magnetic moment of each layer, as shown by the solid staircase-like lines in Figs. 2(c) and 2(d). The obtained depth profiles show interfacial enhancement of the Fe orbital and spin magnetic moments at the Fe/MgO interface. By contrast, the spin magnetic moment diminished at the Fe/V interface.

To interpret the experimental observations, we performed first-principles calculations. Figure 2(e) shows the used supercell. The calculated magnetic moments are shown by the gray shaded bars in Figs. 2(c) and 2(d). Although the calculations reproduced interfacial enhancement of the spin magnetic moments, it significantly underestimated the orbital counterpart. To resolve this discrepancy, we performed the calculations with orbital polarization (OP) correction. This correction accounts for the electron–electron correlation

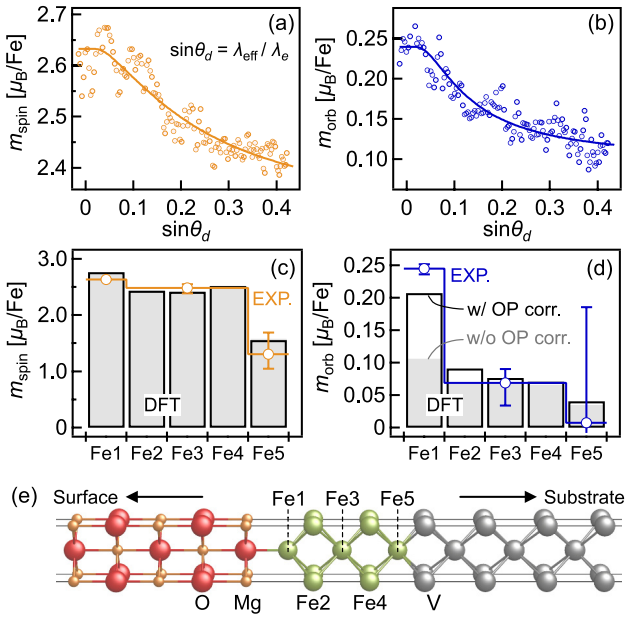

Fig. 2. Detection-angle-dependent (a) spin magnetic moment m_{spin}, (b) orbital magnetic moment m_{orb}. Solid curves represent the fit. Depth profiles of (c) spin magnetic moment and (d) orbital magnetic moment. Staircase-like lines with open markers represent experimental data; black bars and gray shaded bars represent results of first-principles calculations with and without orbital polarization (OP) correction, respectively. (e) Supercell used for calculations.

by satisfying Hund's second rule and provide an accurate description of orbital magnetic moments and PMA. The OP correction calculations considerably increased the orbital magnetic moment at the Fe/MgO interface close to the experimental value, as shown by the black bars in Figs. 2(c) and 2(d). This agreement suggests that the electron–electron correlation, probably strengthened by interfacial electron localization, enhance the orbital magnetic moment at the Fe/MgO interface and the PMA.

The present findings [2] should also apply to other ferromagnetic metal/oxide interfaces, including CoFeB/MgO systems, as enhanced electron−electron correlation is generic to such interfaces with the abrupt termination of metallic bonds. Furthermore, this study provides insights into the importance of considering electron−electron correlation, which have often been disregarded in spintronics, to understand various phenomena that emerge at interfaces.

References
[1] K. Amemiya, Phys. Chem. Chem. Phys. **14**, 10477 (2012).
[2] S. Sakamoto, M. Tsujikawa, M. Shirai, K. Amemiya, and S. Miwa, ACS Appl. Electron. Mater. **4**, 1794 (2022).

Authors
S. Sakamoto, M. Tsujikawa[a], M. Shirai[a], K. Amemiya[b], and S. Miwa
[a]Tohoku University
[b]KEK

Mott-Insulator-Like Bose-Einstein Condensation in a Tight-Binding System of Interacting Bosons with a Flat Band

Kawashima Group

We considered a Bose-Hubbard model on a two-dimensional lattice. We showed that the model parameters (the lattice structure, the hopping constants, and the chemical potential) can be tuned in such a way that the ground state is generated by applying, to the vacuum, N creation operators of locally-defined quasi-particles, where N is proportional to the total number of lattice points. The resulting model has a free parameter β that controls the degree of quantum fluctuation; β = 0 for no fluctuation and β = 1/2 for the maximum fluctuation. We carried out Monte Carlo simulation of this model at zero temperature, and discovered that the model undergoes a quantum phase transition when we change this parameter. While the system is 2+1 dimensional, the new phase transition exhibits the characteristics of 2 dimensions, i.e., the Kosterlitz-Thouless phase transition analogous to the classical XY model in 2 dimensions. Accordingly, the large β phase is the quasi Bose-Einstein condensation phase.

The above-mentioned ground state is expressed exactly as a tensor network with the bond dimension 2. Tracing out this tensor network is equivalent to calculating the partition function of some classical loop gas model. This is why the quantum criticality exhibits the purely 2-dimensional characteristics. It also allows us to construct a Monte Carlo algorithm for efficient sampling from the space of classical occupation-number configurations. In other words, we can stochastically trace out the tensor network to obtain various physical quantities of interest, such as the static structure factors and the helicity modulus.

The lattice is generated from the square lattice by duplicating each bond into p copies and introducing an additional site in the middle of each copy. (Fig. 1) The direct hopping

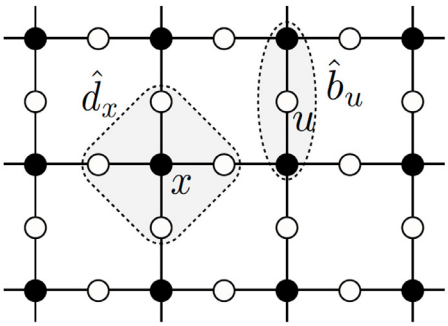

Fig. 1. The lattice considered (p=1). Within each cluster specified by x or u, a tuned hopping between the black and the white sites is defined.

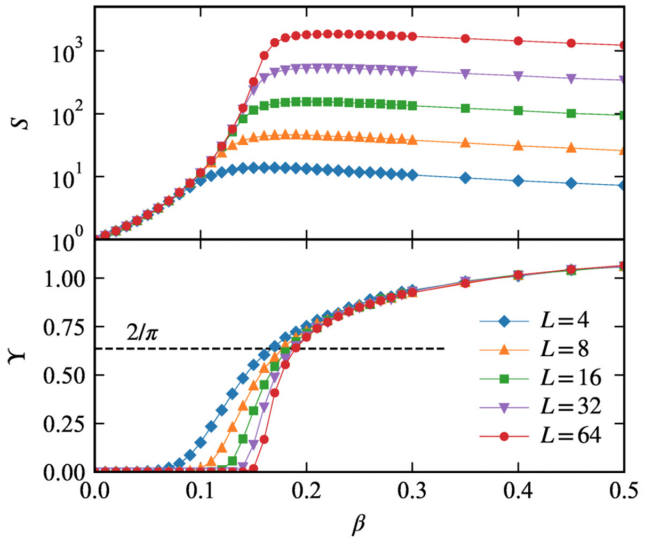

Fig. 2. The static structure factor S (top) and the helicity modulus (bottom) as functions of β for p=2. The horizontal line in the bottom panel indicates the universal jump 2/π, the thermodynamic value characteristic to the KT transition point.

is allowed only within local clusters labelled by either x or u. While bosons interact with each other, the model is constructed in such a way that the dispersion of a single particle has a flat band if influence of the other paricles could be neglected. The result of the Monte Carlo simulation are shown in Fig. 2. The static structure factor diverges around β = 0.2 and, at the same time, the helicity modulus jumps from 0 to 2/π, the universal value characteristic to the KT transition.

Reference

[1] H. Katsura, N. Kawashima, S. Morita, A. Tanaka, and H. Tasaki, Phys. Rev. Research, **3** 033190 (2021).

Authors
H. Katsura[a], N. Kawashima, S. Morita, A. Tanaka[b], and H. Tasaki[c]
[a]The University of Tokyo
[b]National Institute of Technology
[c]Gakushuin University

Double Superconducting Dome and Triple Enhancement of T_c in the Kagome Superconductor CsV_3Sb_5 under High Pressure

Uwatoko Group

The newly discovered kagome metals AV_3Sb_5 (A = K, Rb, Cs) have aroused tremendous research interest as a novel platform to study the interplay between nontrivial band topology, superconductivity (SC) and charge-density-wave (CDW) order [1-4]. At ambient conditions, these materials crystallize into a layered structure with hexagonal symmetry (space group *P6/mmm*), inset of Fig. 1(a), consisting of A layer and V-Sb slab stacked alternatively along the c-axis. The most prominent feature of this structure is the presence of quasi-2D ideal kagome layers of V ions coordinated by Sb. These compounds are metallic and enter a superconducting ground state below T_c = 0.93, 0.92, and 2.5 K for A= K, Rb, and Cs [2-4], respectively. In the normal state, their transport and magnetic properties exhibit a clear anomaly at T^* = 78, 104, and 94 K, respectively, due to the formation of CDW-like order as revealed by the x-ray diffraction and scanning tunning microscopy measurements [2-4]. The charge order in KV_3Sb_5 has been found to display a chiral anisotropy [5], which can lead to giant anomalous Hall effect in the absence of magnetic order or local moments [6,7]. It was also argued as a strong precursor of unconventional SC. Moreover, angle-resolved photoemission spectroscopy measurements and density-functional-theory calculations have characterized their normal state as a Z_2 topological metal with multiple Dirac nodal points near the Fermi level [1,4], consistent with the observations of Shubnikov-de Haas quantum oscillations and small Fermi surfaces (FSs) with low effective mass in RbV_3Sb_5 [3].

At present, the topologically related phenomena and SC have been actively studied in these AV_3Sb_5 compounds, but

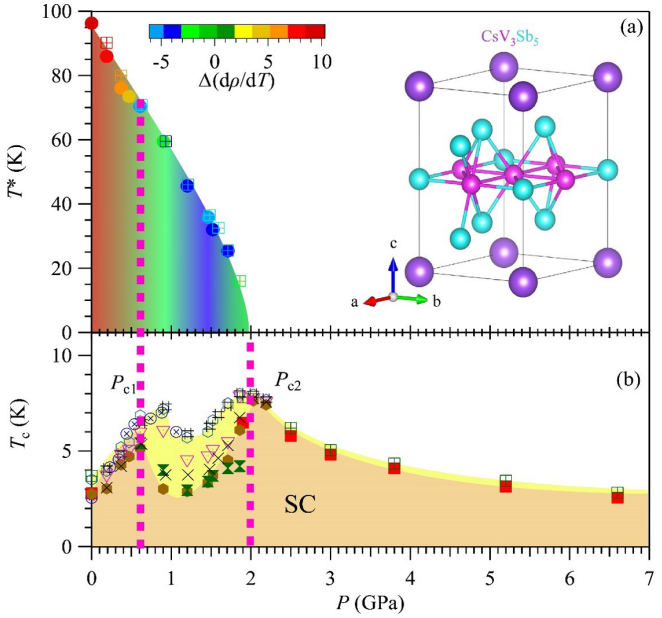

Fig. 1. Temperature-pressure phase diagram of CsV_3Sb_5. Pressure dependence of the transition temperatures for (a) the CDW-like order and (b) superconductivity. The color scale in (a) represents the sign of $\Delta(d\rho/dT)$ around T^*, which changes sign near P_{c1} due to the modification of CDW order. Inset of (a) shows the crystal structure of CsV_3Sb_5. The yellow region between P_{c1} and P_{c2} in (b) corresponds to a relatively broad superconducting transition.

the rich physics related to the electron correlation, especially the relationship between the intertwined electronic orders, has been barely revealed. In this regard, it is interesting to unveil the correlation between the CDW-like order and SC commonly observed in these AV_3Sb_5 materials. Thus, we have chosen to study CsV_3Sb_5 with the highest T_c among this series of compounds by applying a high-pressure approach, which has been widely used in disentangling the competing electronic orders of strongly correlated metals. The interplay between CDW and SC in CsV_3Sb_5 was studied via measurements of resistivity, DC and AC magnetic susceptibility under various pressures up to 6.6 GPa [8]. We find that the CDW transition decreases with pressure and experience a subtle modification at $P_{c1} \approx 0.6$-0.9 GPa before it vanishes completely at $P_{c2} \approx 2$ GPa. Correspondingly, $T_c(P)$ displays an unusual M-shaped double dome with two maxima around P_{c1} and P_{c2}, respectively, leading to a tripled enhancement of T_c to about 8 K at 2 GPa. The obtained temperature-pressure phase diagram, Fig. 1, resembles those of many unconventional superconductors, illustrating an intimated competition between CDW-like order and SC. The competition is found to be particularly strong for the intermediate pressure range $P_{c1} \leq P \leq P_{c2}$ as evidenced by the broad superconducting transition and reduced superconducting volume fraction. The modification of CDW order around P_{c1} has been discussed based on the band structure calculations. Our work not only demonstrates the potential to raise T_c of the V-based kagome superconductors, but also offers more insights into the rich physics related to the electron correlations in this novel family of topological kagome metals.

References

[1] B. R. Ortiz, L. C. Gomes, J. R. Morey *et al.*, Phys. Rev. Mater. **3**, 094407 (2019).
[2] B. R. Ortiz, E. Kenney, P.M. Sarte *et al.*, Phys. Rev. Mater. **5**, 034801 (2021).
[3] Q.W. Yin, Z. J. Tu, C. S. Gong *et al.*, Chin. Phys. Lett. **38**, 037403 (2021).
[4] B. R. Ortiz, S. M. L. Teicher, Y. Hu *et al.*, Phys. Rev. Lett. **125**, 247002 (2020).
[5] Y. X. Jiang, J. X. Yin, M. M. Denner *et al.*, Nature Mater. **20**, 1353 (2021).
[6] S. Y. Yang, Y. J. Wang, B. R. Ortiz *et al.*, Sci. Adv. **6**, eabb6003 (2020).
[7] E. M. Kenney, B. R. Ortiz, C. N. Wang *et al.*, J. Phys. Condens. Matter. **33**, 235801 (2021).
[8] K. Y. Chen, N. N. Wang, Q. W. Yin *et al.*, Phys. Rev. Lett. **126**, 247001 (2021).

Authors

K. Y. Chen[a], N. N. Wang[a], Q. W. Yin[b], Y. H. Gu[a], K. Jiang[a], Z. J. Tu[b], C. S. Gong[b], Y. Uwatoko, J. P. Sun[a], H. C. Lei[b], J. P. Hu[a], and J.-G. Cheng[a]

[a]Institute of Physics, Chinese Academy of Science
[b]Renmin University of China

Nearly Room Temperature Ferromagnetism in a Pressure-Induced Correlated Metallic State of van der Waals Insulator $CrGeTe_3$

Uwatoko Group

Discovery of two-dimensional (2D) magnetism in van der Waals (vdW) materials have unfurled diverse range of possibilities for development of novel spintronics, multiferroic and quantum computing devices using atomically

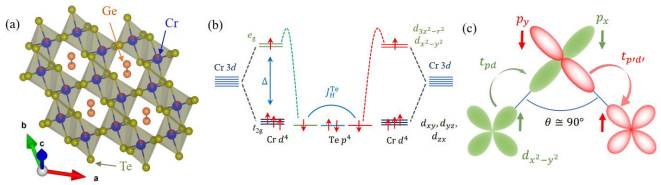

Fig. 1. (a) Single layer of $CrGeTe_3$ illustrating the honeycomb network of edge sharing $CrTe_6$ octahedra. In case of CrX_3, the place of Ge-Ge dimers remains vacant. (b) Crystalline electric field splitting of Cr 3*d* orbitals into t_{2g} - and e_g -manifolds. Δ is the energy difference between t_{2g}- and e_g levels. J_H^{Te} is the Hund's coupling energy at Te site. (c) Schematic picture of indirect superexchange FM interaction between Cr e_g-orbitals via two Te *p*-orbitals. $t_{pd}(t_{p'd'})$is the virtual hopping between e_g (e'_g) and *p* (*p*') orbitals. θ is the geometrical Cr-Te-Cr bond angle.

thin materials [1]. Among the vast pool of vdW materials, $CrGeTe_3$ and CrX_3 (X = Cl, Br, I) are Mott insulators with a charge gap, thus facilitating suitable platforms to exploit both charge and spin degrees of freedom. At low temperature, these insulators share a common layered rhombohedral $R\bar{3}$ -crystal structure held together by weak vdW forces along the *c*-axis. Each single layer consists of a honeycomb network of edge sharing octahedra formed by a central Cr atom bonded to six ligand atoms (Te or X), as illustrated in Fig. 1(a) for $CrGeTe_3$.

The crystalline field effect ensuing from this octahedra splits the Cr-3d orbitals into t_{2g} - and e_g-manifolds [Fig.1(b)]. The onsite Coulomb repulsion localizes the t_{2g}-electrons driving the system into an insulating state significantly well above T_C. Although, a direct antiferromagnetic exchange interaction exists between t_{2g}-electrons, thermal fluctuation inherent to 2D suppress the long-range magnetic order. The spin orbit coupling (SOC) emanating through the covalent bond between ligand *p* and Cr-e_g orbital generates the magnetocrystalline anisotropy energy to counteract the thermal fluctuation. Below T_C, the superexchange interaction between Cr-e_g electrons via two different ligand p-orbitals, as schematically portrayed in Fig.1(c), benefits from the distortion of $CrTe_6$ octahedra and the Hund's energy gain at the ligand Te (or X) site to stabilize the FM order. The correlation between t_{2g}-electrons also move up the ligand *p* bands close to Fermi level, thus opening a band gap between the Cr *d* conduction band and the ligand *p* valence band indicating a charge transfer type Mott behaviour.

However, one drawback for the practical technological application is the low Curie temperature, T_C, mostly below liquid nitrogen temperature. For exploitation of these attributes, it is essential to realize this novel FM state at or close to room temperature. Recently, T_C of $CrGeTe_3$ has been raised around 200 K either by intercalating large organic ions into single crystals [2] or using sophisticated process like electrochemical doping to field effect transistor devices [3]. Although, these results are promising, such filling control methods lead to strong charge inhomogeneity as well as structural and chemical defects, including creation of magnetic impurity, unfavourable for device application.

On the other hand, application of pressure is advantageous, which not only controls the bandwidth but also the spin exchange pathways via subtle modification of bond length and angle between atoms avoiding the complication of disorder. Here, for the first-time we show the evidence of nearly room temperature FM in $CrGeTe_3$ bulk single crystals with application of pressure [4]. Using highly sensitive dc magnetic susceptibility and resistivity measurement under high quality hydrostatic pressure, we found that T_C of $CrGeTe_3$ exceeds 250 K above 9.1 GPa. In Fig. 2, we present

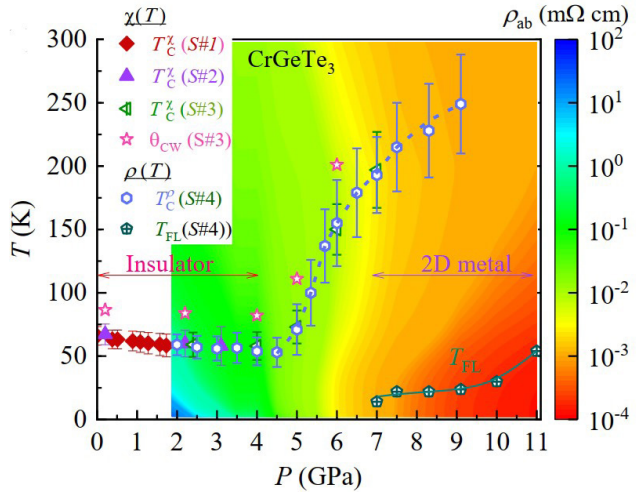

Fig. 2. Pressure temperature phase diagram of $CrGeTe_3$. Color scale represents the magnitude of ρ_{ab}. θ_{CW} and T_C^{χ} respectively are the Curie-Weiss temperature and Curie temperature, estimated from magnetic susceptibility. T_C^{ρ} and T_{FL} are Curie temperature and Fermi liquid temperature determined from ρ_{ab}.

the pressure-temperature phase diagram of $CrGeTe_3$ which uncovers a rare example of bandwidth-controlled insulator-metal transition (IMT) in a vdW materials. Moreover, the remarkable absence of accompanied structural transition and spin crossover involving magnetic to non-magnetic states across IMT, clearly indicates the pressure driven changes of electronic property are purely electronic in origin. Furthermore, these findings show that electronic property of $CrGeTe_3$ can be switched much more responsively using external perturbation, such as strain, doping compared to other vdW insulators.

References
[1] C. Gong *et al.,* Nature, **546**, 265 (2017).
[2] N. Wang *et al.,* J. Am. Chem. Soc, **141**, 17166 (2019).
[3] I. A. Verzhbitskiy *et al.,* Nat. Electron., **3**, 460 (2020).
[4] Dilip Bhoi, J. Gouchi, N. Hiraoka, Y. Zhang, N. Ogita, T. Hasegawa, K. Kitagawa, H. Takagi, K. H. Kim, and Y. Uwatoko, Phys. Rev. Lett. **127**, 217203 (2021)

Authors
D. Bhoi, J. Gouchi, N. Hiraoka[a], Y. Zhang[b], N. Ogita[c], T. Hasegawa[c], K. Kitagawa[a], H. Takagi[a,d,e], K. H. Kim[f,g], and Y. Uwatoko
[a]The University of Tokyo
[b]Southeast University
[c]Hiroshima University
[d]Institute for Functional Matter and Quantum Technologies, University of Stuttgart
[e]Max Planck Institute for Solid State Research
[f]CeNSCMR, Seoul National University
[g]Institute of Applied Physics, Seoul National University

Pressure-Induced Superconductivity in the Excitonic Insulator Candidate Ta_2NiSe_5

Uwatoko Group

Superconductor hosts a condensate of electron pairs (Cooper pairs), which can conduct electricity without any loss of energy. In conventional superconductivity, an attractive interaction mediated by lattice vibrations can lead electrons to form pairs. The bound states through attractive Coulomb attraction between electrons and holes, similar to Cooper pairs in superconductivity, are called excitons. A spontaneous condensation of excitons with lowering temperature is expected to occur due to weakly screened Coulomb interactions in narrow gap semiconductors and semimetals. In that case, the system becomes an insulator known as an excitonic insulator. The excitonic insulator was theoretically proposed more than 50 years ago, however, experimental facts for excitonic state are far from conclusive.

A layered chalcogenide Ta_2NiSe_5 located near the semiconductor-semimetal boundary has in recent years attracted attention as a promising candidate for the excitonic insulator. At ambient pressure, semiconductor-to-insulator transition occurs at $T_c \sim 328$ K, accompanied with a structural phase transition from high-temperature orthorhombic to low-temperature monoclinic. The transition at T_c has been discussed to be the excitonic transition as manifested by the characteristic flattening of the valence band [1]. Furthermore, the control of energy gap using a solid-solution $Ta_2Ni(Se_{1-x}S_x)_5$ and an application of moderate pressure reproduce the canonical phase diagram for the excitonic insulator [2]. Here we show a high-pressure phase diagram of Ta_2NiSe_5 covering the whole range from semiconducting to semimetallic region for the first time, and discovered pressure-induced superconductivity in the semimetallic phase [3].

Figure 1 depicts a pressure-temperature phase diagram of Ta_2NiSe_5 based on bulk measurements under pressure. Ta_2NiSe_5 exhibits a first-order structural transition under pressure at $P_s \sim 3$ GPa, which is accompanied by the change from an almost zero-gap semiconductor to a semimetal. In the pressure-induced semimetallic phase, there appears a transition to another semimetal with a partial-gap at T^*, accompanied with a lattice distortion analogous to that occurs at the excitonic transition at low-pressure semiconducting phase. With increasing pressure, T^* is suppressed and reaches to zero temperature around $P_c \sim 8$ GPa. A dome-like superconducting phase with a maximum $T_{sc} \sim 1.2$ K emerges around P_c. Since the Coulomb interactions between electrons and holes should be screened out substantially due to the increased carrier density, applying pressure changes the character of the gap from excitonic dominant to hybridization gap dominant on increasing the band overlap. Our results evidence the presence of the electron-lattice coupling may be one of the key ingredients for the occurrence of superconductivity and the excitonic transition in the low-pressure phase.

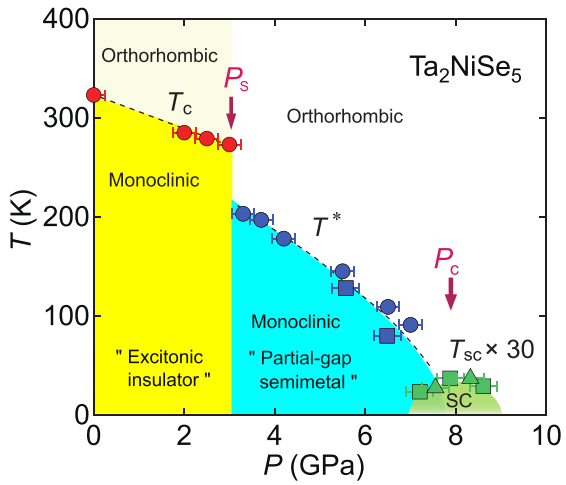

Fig. 1. Temperature-pressure phase diagram of Ta_2NiSe_5 obtained from bulk measurements under pressure. The lines are guides for the eye.

References
[1]Y. Wakisaka, T. Sudayama, K. Takubo, T. Mizokawa, M. Arita, H. Namatame, M. Taniguchi, N. Katayama, M. Nohara, and H. Takagi, Phys. Rev. Lett. **103**, 026402 (2009).
[2]Y. F. Lu, H. Kono, T. I. Larkin, A. W. Rost, T. Takayama, A. V. Boris, B. Keimer, and H. Takagi, Nat. Commun. **8**, 14408 (2017).
[3]K. Matsubayashi, H. Okamura, T. Mizokawa, N. Katayama, A. Nakano, H. Sawa, T. Kaneko, T. Toriyama, T. Konishi, Y. Ohta, H. Arima, R. Yamanaka, A. Hisada, T. Okada, Y. Ikemoto, T. Moriwaki, K. Munakata, A. Nakao, M. Nohara, Y. Lu, H. Takagi, and Y. Uwatoko, J. Phys. Soc. Jpn. **90**, 074706 (2021).

Authors
K. Matsubayashi[a], H. Okamura[b], T. Mizokawa[c], N. Katayama[d], A. Nakano[d], H. Sawa[d], T. Kaneko[e], T. Toriyama[e], T. Konishi[e], Y. Ohta[e], H. Arima[a], R. Yamanaka, A. Hisada[b], T. Okada, Y. Ikemoto[f], T. Moriwaki[f], K. Munakata[g], A. Nakao[g], M. Nohara[h], Y. Lu [i], H. Takagi[i], and Y. Uwatoko
[a]The University of Electro-Communications
[b]Tokushima University
[c]Waseda University
[d]Nagoya University
[e]Chiba University
[f]JASRI
[g]CROSS
[h]Hiroshima University
[i]The University of Tokyo

Difference in Curvature Sensing of Isotropic and Anisotropic Curvature-Inducing Proteins

Noguchi Group

In living cells, biomembrane shapes are controlled by various curvature-inducing proteins. We have studied the binding of these proteins using mean-field theories. Clathrin and coat protein complexes bend membranes in a laterally isotropic manner and generate spherical buds. In contrast, Bin/Amphiphysin/Rvs (BAR) superfamily proteins bend the membrane along their BAR domain axes and generate cylindrical membrane tubes. The former and latter proteins can be modeled as laterally isotropic objects and anisotropic objects of a crescent elliptic shape, respectively.

For isotropic proteins, we derived the free energy, including the Gaussian curvature and area expansion by the protein insertion [1]. Then, we investigated the formation of spherical buds [1] and binding onto a tethered vesicle [2]. Experimentally, a narrow membrane tube (tether) is elongated from a spherical vesicle by an external force imposed by a micropipette and optical tweezers. A first-order transition occurs between a small number of large buds and a large number of small buds with increasing chemical potential of protein binding [2]. For the tethered vesicle, interestingly, a first-order transition occurs twice between low and high protein densities in the tube. The force-dependence curves of the protein density in the membrane tube and the tube curvature are reflection symmetric and point symmetric, respectively, from the force point, in which the tube curvature matches the protein (sensing) curvature (see Figs. 1(a) and (b)) [2]. This theory reproduces the meshless membrane simulation results of the homogeneous phases very well. In addition, beaded-necklace-like tubes with microphase separation were found in the simulation.

For anisotropic proteins, an orientational-dependent excluded volume interaction is included in the free energy. We studied binding onto membrane tubes [3]. The proteins exhibit a second-order or first-order nematic transition with increasing protein density for intermediate and small radii of

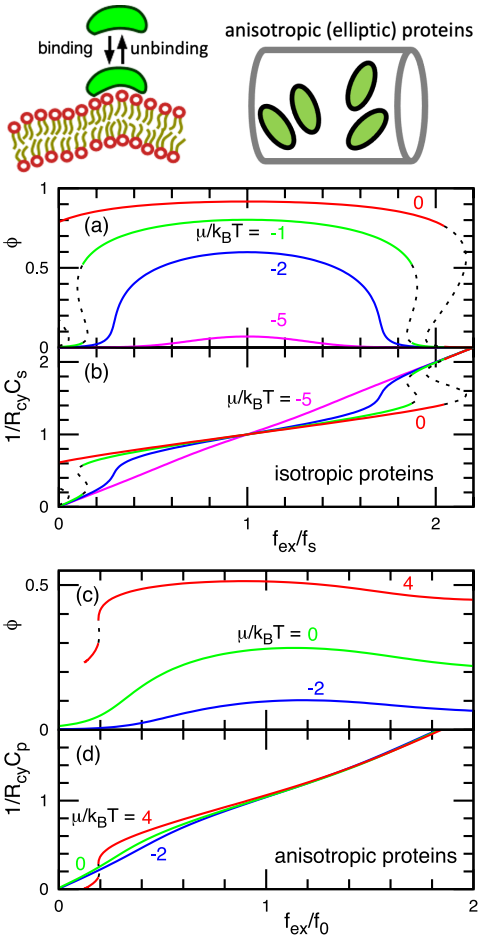

Fig. 1. Binding of proteins onto tubular membranes. External force f_{ex} dependence of protein density φ and tube radius R_{cy}. (a),(b) Isotropic proteins with sensing curvature C_s. (c),(d) Anisotropic proteins with a spontaneous curvature C_p along proteins axis. With increasing binding chemical potential m, more proteins are bound.

the membrane tube, respectively. The tube curvatures for the maximum protein binding (sensing) and orientational order are differently varied by the protein density and rigidity. As the external force along the tube axis increases, a first-order transition from a large tube radius with low protein density to a small radius with high density occurs only once, and subsequently, the protein orientation tilts to the tube-axis direction (see Figs. 1 (c) and (d)). The density-dependent sensing curvature and the number of transitions are characteristics due to the anisotropic bending energy. In contrast, each isotropic protein has a constant sensing curvature. This density-dependent sensing curvature has been measured in the experiment of BAR proteins. This theory quantitatively reproduces the results of meshless membrane simulation for short proteins. For long proteins, the formation of protein clusters generates a quantitative deviation from the theory, although qualitative agreements still hold.

The present theories can be used to estimate the bending rigidity and curvature of bound proteins in experiments and atomistic simulations. These mechanical parameters are keys to quantitatively understand the curvature sensing and generation of proteins.

References
[1] H. Noguchi, Phys. Rev. E **104**, 014410 (2021).
[2] H. Noguchi, Soft Matter **17**, 10469 (2021).
[3] H. Noguchi, C. Tozzi, and M. Arroyo, Soft Matter **18**, 3384 (2022).

Author
H. Noguchi

Structure of Glass-Forming Molecular Liquids under High Pressure

Yamamuro Group

Glass transition is one of the most important unsolved problems in condensed matter physics. The history of the glass transition study might start when Giauque found a heat capacity jump of glycerol in 1923 [1]. After that many people have studied the mechanism of the glass transition both through experimental and theoretical approaches. High pressure studies have played important roles in the glass transition research since they provide direct information for the validity of the two important concepts of the mechanism of the glass transition; i.e., the entropy theory and free-volume theory. At present, the entropy theory, particularly Adam-Gibbs (AG) theory [2], is dominant to explain thermodynamic properties of the glass transition [3] and the pressure dependence of the glass transition temperature (T_g) [4]. An extended version of the AG theory, random first-order transition (RFOT) theory [5], can also explain the non-linear dynamics of the glass transition. Molecular liquids are important materials in the glass transition research since they are similar to the systems treated in theoretical and computer simulation studies. We are interested in van der Waals molecules which are condensed only by the van der Waals interaction, and hydrogen-bonding molecules which have network structures formed by intermolecular hydrogen bonds.

Recently, we have measured X-ray diffraction (XRD) data of toluene ($C_6H_5CH_3$, T_g = 117 K) and glycerol [$(CH_2(OH)CH(OH)CH_2(OH)$, T_g = 187 K] under high pressures (toluene: < 0.9 GPa, glycerol: < 3.6 GPa) at RT. This work is a collaboration with Prof. Yoshio Kono (Ehime Univ.). We used a Paris-Edinburg cell and BL37XU, SPring-8, on which very precise horizontal focusing and collimation are available.

Figure 1 shows the structure factors of toluene at 0.9 GPa. The result of the MD simulation (AMBER force field, 0.2 ns, 500 molecules) is also shown. The MD simulation well reproduces the experimental data. Good agreement was obtained also for the data at 0 and 0.4 GPa. Figure 2 shows the pair distribution functions $g(r)$ of aromatic (benzene-ring) carbons obtained by the MD simulations. As the density (pressure) increases, three peaks between 3 and 6 Å become more prominent. These peaks are known to be due to the T-type pair correlation as shown in the inset. It is noteworthy that this trend is the same as the cooling effect at ambient pressure. Hence, we concluded that the AG concept is valid also for the glass transition by pressurization.

On the other hand, the structure factor of glycerol cannot be reproduced by the MD simulation using the potential parameters at ambient pressure. Therefore, we performed ab initio (Car-Parrinello) MD simulations using a smaller system (50 molecules) and shorter simulation time (0.15 ps) to determine the short-range structure, and then adjusted the Lenard-Jones parameters as a function of pressure so as to reproduce the $g(r)$ obtained by the ab initio MD. Figure 3 shows the structure factors using the adjusted potential parameters. Good agreement is obtained between the experimental and MD data. Form the obtained structure, we found that the molecular structure is deformed to be more compact keeping hydrogen bonds. The C-O intermolecular correlation is also important under high pressure. The present conclusion is quite different from the common sense that

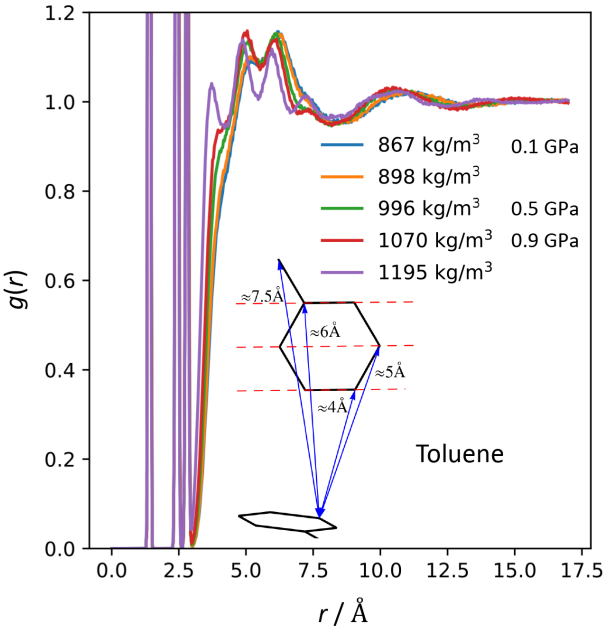

Fig. 2. Pair distribution function for aromatic carbon atoms of toluene. Preferred pair correlation is shown by inset.

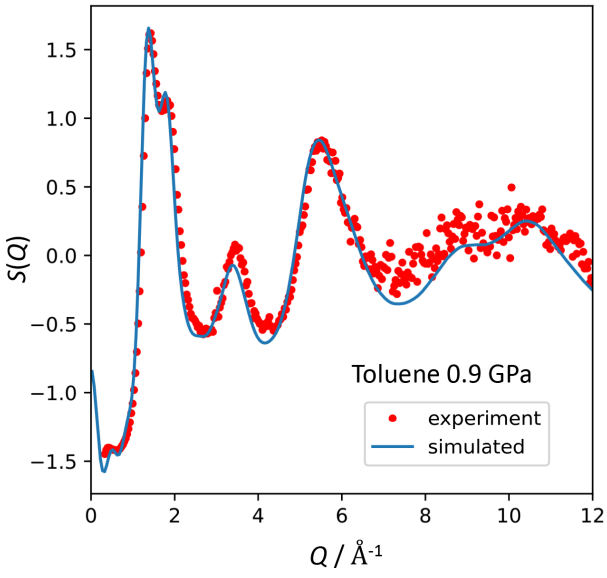

Fig. 1. Structure factor of toluene at 0.9 GPa.

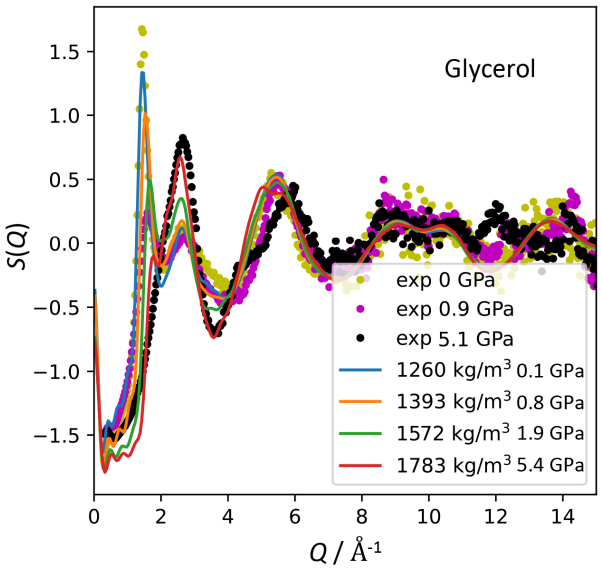

Fig. 3. Structure factor of glycerol under high pressure.

hydrogen bonds are just broken by pressurization. A neutron diffraction experiment is under planning to determine the position of the hydrogen atoms and make clearer discussion on the competing hydrogen-bond and van der Waals interactions under high pressure.

References

[1] G. E. Gibson and W. F. Giauque, J. Am. Chem. Soc. **40**, 93 (1923).
[2] G. Adam and J. H. Gibbs, J. Chem. Phys. **43**, 139 (1965).
[3] S. Tatsumi *et al*., Phys. Rev. Lett. **109**, 045701 (2012).
[4] O. Yamamuro *et al*., J. Non-Cryst. Solids, **183**, 144 (1995).
[5] T. R. Kirkpatrick *et al*., Phys. Rev. A **40**, 1045 (1989).

Authors

Y. Zhao, H. Akiba, N. Kondo[a], Y. Kono[a], and O. Yamamuro
[a]Ehime University

Nontrivial Temperature Dependence of Magnetic Anisotropy in Multiferroics $Ba_2MnGe_2O_7$

Masuda group

Spin-driven multiferroics have been extensively studied since the discovery of an enhanced magnetoelectric effect in $TbMnO_3$. Through spin-orbit coupling (SOC), a spin order induces a change of charge distribution, leading to emergence of electric polarization. The microscopic mechanisms of the multiferroics are categorized into three types: the spin current, the exchange striction, and the spin dependent *d-p* hybridization. A notable feature of the third one is that hybridized *d* and *p* orbitals of magnetic ion and ligand are modulated by spin states via SOC, and this induces an electric polarization. The relation between the electric polarization $\boldsymbol{P}$ and the spin moment $\boldsymbol{S}$ is locally described. The mechanism has been identified in several compounds including åkermanite compounds $Ba_2CoGe_2O_7$. Since the direction of the local spin moment determines the direction of the electric polarization, magnetic anisotropy plays a key role in forming multiferroic structure, *i.e.*, the simultaneous structures of the spin and polarization. The magnitude of the anisotropy gives the energy scale for the control of the magnetism by the electric field as well as magnetic field. Although the temperature (T) dependence of the anisotropy gap in magnon spectrum in a conventional magnet scales as a power of the sublattice magnetic moment, it may not be the case for the multiferroics. The change of the polarization with T affects the spin-interaction parameters through the *d-p* hybridization, which can lead to a nontrivial behavior in T dependence of the anisotropy and a low-energy spin dynamics. Here we study spin dynamics on a square-lattice antiferromagnet $Ba_2MnGe_2O_7$ known as multiferroic compound by using a state-of-art spectrometer with ultra-high resolution.

Figure 1(a) shows the INS spectrum measured at 0.05 K. Two dispersive modes with the boundary energy of 0.55 meV and with gaps ~ 0.05 meV and ~ 0.1 meV are clearly observed. The gap of the low-energy (T_1) mode is ascribed to easy-axis anisotropy in the square lattice by spin nematic interaction/electric polarization interaction; $\mathcal{H}_N = \sum_{i,j} J_N O_i^{XY} O_j^{XY} = \sum_{i,j} J_P P_i^Z P_j^Z$, where J_N is nematic interaction, O^{XY} is Stevens operator, and J_P is an effective interaction between the electric polarizations. Anisotropy gap of the high-energy (T_2) mode is ascribed to easy-plane anisotropy by a single-ion anisotropy. We find that the former gap is

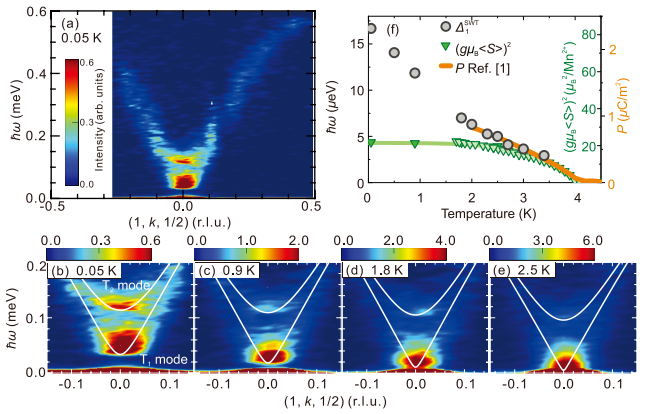

Fig. 1. Inelastic neutron scattering (INS) spectra. (a) False color plot of the INS spectrum measured at 0.05 K projected onto the $\hbar\omega$ - (1, k, 1/2) plane. The spectrum is integrated in the range of $0.9 \le h \le 1.1$ and $0.45 \le l \le 0.55$. White solid curves are calculated magnon-dispersions. (b)-(e) The INS spectra focused on the low-energy range measured at (b) 0.05 K, (c) 0.9 K, (d) 1.8 K and (e) 2.5 K. White solid curves are calculated dispersions. (f) T dependences of Δ_1^{SWT} (black circles), electric polarization P (orange curve from Ref. [1]) and the second power of the sublattice moment (light green triangles).

drastically suppressed with the increase of T, while the latter gap is moderately suppressed as shown in Figs. 1(b)-1(e). We also find that J_N is strongly dependent on T.

T dependences of the easy-axis anisotropy Δ_1^{SWT}, a scaled electric polarization P, and the second power of the scaled sublattice moment $(g\mu_B S)^2$ are shown in Fig. 1(f). We find that Δ_1^{SWT} does not scale as $(g\mu_B S)^2$, but is rather consistent with the temperature dependence of P. Indeed, our spin-wave calculation including the spin nematic term $\mathcal{H}_N$ exhibits that the formula of the anisotropy gap is proportional to P. Furthermore, the calculation shows that the drastic T dependence of J_N results from the change of orbital with T; the modification of the hybridized orbitals of Mn^{2+} and O^{2-} ions with T leads to a small change of the energy, which is negligible in highly anisotropic system but is enhanced in the nearly isotropic system such as the symmetric half-filled shell of Mn^{2+} ion, and it is probed as the change of J_N thorough SOC. We, thus, find a characteristic quasiparticle of the multiferroics originating from the hybridization of spin and orbital momenta.

References

[1] H. Murakawa, Y. Onose, S. Miyahara, N. Furukawa, and Y. Tokura, Phys. Rev. B **85**, 174106 (2012).
[2] S. Hasegawa, S. Hayashida, S. Asai, M. Matsuura, I. Zaliznyak, and T. Masuda, Phys. Rev. Research **3**, L032023 (2021).

Authors

S. Hasegawa, S. Hayashida, S. Asai, M. Matsuura[a], I. Zaliznyak[b], and T. Masuda
[a]CROSS
[b]Brookhaven National Laboratory

Polarized Neutron Scattering Study on a Centrosymmetric Skyrmion Host Gd_2PdSi_3

Nakajima Group

Gadolinium based intermetallic compounds have been intensively investigated since the discovery of magnetic skyrmion lattice, which is topologically-nontrivial vortex-like spin texture, with the large topological Hall effect in a

triangular lattice itinerant magnet Gd_2PdSi_3 [1]. Although magnetic skyrmions were discovered in chiral ferromagnets such as MnSi [2], the recent study on Gd_2PdSi_3 has demonstrated that centrosymmetric magnets can also host magnetic skyrmions owing to coupling between local magnetic moments and conduction electrons. Subsequent studies on a breathing kagome system $Gd_3Ru_4Al_{12}$ [3] and a tetragonal magnet $GdRu_2Si_2$ [4] also reported emergence of skyrmion lattice states. In these studies, resonant X-ray magnetic scattering techniques were used because the L_2 absorption edge of Gd is located at 7.935 keV, which is suited for conventional scattering measurements. By analyzing light polarizations of scattered X-rays, magnetic structures in these compounds were investigated. However, resonant X-ray scattering is quite sensitive not only to the magnetic moments but also charge density waves. A recent STM study on $GdRu_2Si_2$ reported possible coexistence of magnetic and charge modulations [5]. To verify the magnetic structures in Gd-based skyrmion systems, we employ polarized neutron scattering technique, which can unambiguously distinguish magnetic modulations from charge/nuclear modulations.

In the present study, we focus on Gd_2PdSi_3, in which the triangular skyrmion lattice state was discovered in the first field-induced phase. In zero field, this system exhibits two magnetic phase transitions, which were identified by previous specific heat measurements, below 21 K. According to the previous resonant X-ray study, the ground state has screw-type magnetic modulations, while the thermally-induced phase was not investigated in detail. We thus studied the temperature evolution of the magnetic order near zero magnetic field by means of polarized neutron scattering.

Gd is one of the strongest neutron absorbers, and thus we used an isotope-enriched $^{160}Gd_2PdSi_3$ crystal, which has relatively weak absorption, for the present study. The experiment was performed at the polarized neutron triple-axis neutron spectrometer PONTA in JRR-3. The sample was mounted in a closed-cycle refrigerator with the $(H,K,0)$ scattering plane. The spectrometer was operated in the P_{zz} and P_{xx} longitudinal polarization analysis modes. In the former mode, the direction of the neutron polarization is perpendicular to the horizontal scattering plane. In the latter, neutron polarization is set to be parallel or antiparallel to the scattering vector Q $(= k_i - k_f)$.

Figure 1(a) shows a polarized neutron scattering profile of a magnetic Bragg reflection at $(0,q,0)$ measured at 2.5 K. Red and blue symbols correspond to spin-flip (SF) and non-spin-flip (NSF) scattering intensities, which are proportional to Fourier-transformed magnetic moments parallel to the c axis and those perpendicular to both the c axis and q-vector, respectively. Note that NSF signals may also be attributed to a charge or lattice modulation with the same q-vector. We thus measured the same reflection with the P_{xx} configuration, in which all the magnetic signals are observed only in the SF channel. As shown in Fig. 1(b), we found that the reflection does not contain NSF intensity, demonstrating that the reflection at $(0,q,0)$ is purely magnetic. We thus conclude that the magnetic structure in the ground state is an elliptic screw-type structure. We also measured temperature dependence of the SF and NSF intensities with varying temperature, and found that the c-axis component of the magnetic moments disappears upon the phase transition to the intermediate phase. More detailed analyses are ongoing and will be published elsewhere.

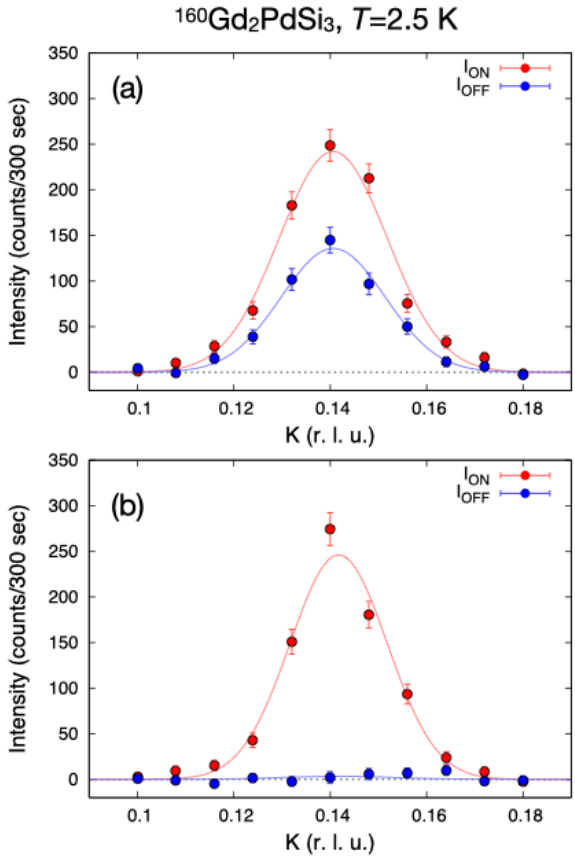

Fig. 1. Polarized neutron scattering profile of a magnetic Bragg reflection at (0,q,0) measured at 2.5 K in (a) P_{zz} and (b) P_{xx} configurations.

References

[1] T. Kurumaji *et al*., Science. **365**, 914 (2019).
[2] S. Muhlbauer *et al*., Science **323**, 915 (2009).
[3] M. Hirschberger *et al*., Nat. Commun. **10**, 5831 (2019).
[4] N. D. Khanh *et al*., Nat. Nanotech. **15**, 444 (2020).
[5] Y. Yasui *et al*., Nat. Commun. **11**, 5925 (2020).

Authors
J. Ju, H. Saito, and T. Nakajima

Tough and Highly Recoverable Hydrogel Reinforced by Strain-Induced Crystallization

Mayumi Group

Hydrogels, cross-linked polymer networks containing water, are expected to be applied for biomaterials such as artificial cartilage, ligaments, and prosthetic joints due to their high water content and biocompatibility. For the applications as the biomaterials, the mechanical toughness and instant recoverability are needed because artificial ligaments and prosthetic joints should survive under repeated high stress at a high frequency (ex. 1 Hz). Most tough hydrogels are reinforced by introducing sacrificial structures that can dissipate input energy [1]. However, since the sacrificial damages cannot recover instantly, the toughness of these gels drops substantially during consecutive cyclic loadings. In this work, we have developed for the first time a tough and instantly recoverable hydrogels utilizing strain-induced crystallization (SIC) [2].

We used slide-ring (SR) gel containing movable figure-of-eight cross-links that work as pulleys to eliminate stress heterogeneities during deformation. SR hydrogel was

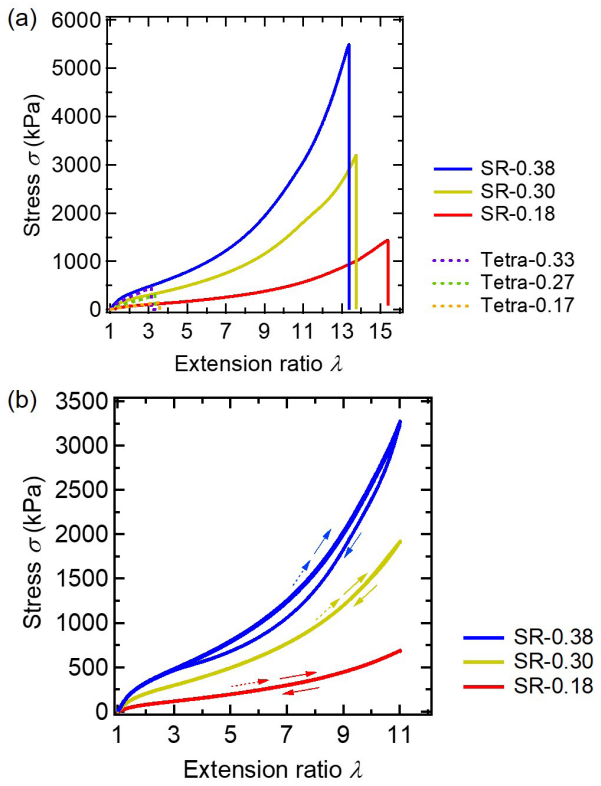

Fig. 1. Stress-extension ratio curves of SR and Tetra gels, (b) loading-unloading curves of SR gels under repeated cyclic stretching.

prepared from polyrotaxane in which only 2 % of its polyethylene glycol (PEG) axis was threaded with a-cyclodextrin (CD) rings. The CDs are covalently cross-linked by adding cross-linkers. The slidable cross-linking points in SR gels can slide on the PEG chains to homogenize stress in the polymer network. For comparison, fixed cross-link PEG gels were prepared via end-crosslinking of Tetra-armed PEG prepolymers. The PEG concentrations and molecular weights of polymer strands between cross-linking points in the Tetra gels were almost the same as those in the SR gels.

Fig. 1 (a) shows the tensile stress–extension ratio curves until rupture for the SR and Tetra gels. The SR gels can survive at higher stress (> 5 MPa) and higher strain (> 1000%) compared with the Tetra-PEG gels. The toughness of the SR gels is comparable to that of the most tough polymer gel with the breakable sacrificial structure. Also, as shown in Fig.1 (b), the mechanical hysteresis of the SR gels under repeated cycle is quite small, and the instant recovery of extension energy between two consecutive cycles is 95 %, which is much higher than the low recoverability of the tough polymer gels having breakable structure (< 50%).

The high toughness of the SR gels originates from strain-induced crystallization (SIC). As shown in Fig. 2, at large strains, we observed diffraction spots in the wide-angle X-ray scattering (WAXS) patterns, indicating the occurrence of SIC of the stretched PEG chains. On the other hand, no diffraction spots were observed for the Tetra gels. The slidability of the cross-liinking points homogenizes the orientation and deformation of PEG chains, which results in the remarkable high toughness of the SR gels. During the unloading process, the strain-induced crystalline structure disappeared immediately. The reversible formation/destruction of the PEG crystals under repeated cycles leads to the high mechanical reversibility of the SR gels.

Although SIC has been reported in rubbers without any

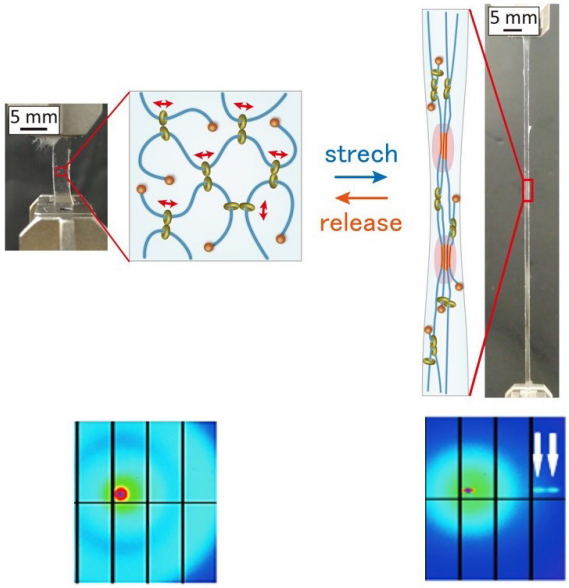

Fig. 2. Schematic illustration and WAXS patterns of SR gels.

solvent, it is the first time to discover the reversible SIC in polymer gels with much lower polymer concentrations. This self-reinforcement strategy by SIC is a novel concept for realizing simultaneously high mechanical toughness and rapid recoverability under cyclic deformation, which are required for the biomedical materials for artificial joints and ligaments.

References
[1] J. P. Gong, Soft Matter **6**, 2583 (2010).
[2] C. Liu, N. Morimoto, L. Jiang, S. Kawahara, T. Noritomi, H. Yokoyama, K. Mayumi, K. Ito, Science **372**, 1078 (2021).

Author
K. Mayumi

Phase Transition in $5d^1$ Double Perovskite Ba_2CaReO_6 Induced by High Magnetic Field

Kindo, Y. Matsuda, and Hiroi Groups

Physical properties emerging from the combination effect of electron correlation and spin-orbit coupling have attracted considerable attention in the last decade. In 5*d* transition metal ions with partially filled t_{2g} orbital, large spin-orbit coupling of 0.4 eV may entangle the effective orbital angular momentum and the spin angular momentum. The electronic state is described by the effective total angular momentum J_{eff}. For example, an unpaired electron in the d^1 ion in the cubic octahedral crystal field occupies the J_{eff} = 3/2 quartet. In solids, interactions among spin-orbital entangled electrons may give rise to exotic ground states such as a spin liquid and multipolar orders. When the d^1 ions with the J_{eff} = 3/2 state interact on the face-centered-cubic (FCC) lattice, unconventional ground states such as multipolar orders, spin-orbit dimer phase, and spin-orbital liquid may emerge. In the multipolar ordered states, magnetic dipolar, electric quadrupolar, and magnetic octupolar moments can be the order parameter. Magnetic properties of double perovskite-type oxides, chlorides, bromides, and lacunar spinel selenides have been investigated as Mott insula-

tors with the J_{eff} = 3/2 state on the FCC lattice [1-4]. These examples demonstrate that various multipolar and dimer orders can be realized by applying a certain perturbation via non-magnetic cations and ligand anions.

Another way for exploring a novel electronic phase is applying strong magnetic field comparable to the magnitude of interactions among electrons. In the spin-1/2 Heisenberg model on the tetragonally distorted FCC lattice as seen in the rhenium double perovskite oxides at low-temperature, successive field induced magnetic phases including the 1/2-magnetization plateau may appear in the magnetization process. While the electric quadrupoles do not couple with magnetic field directly, a possibility of magnetic field induced quadrupolar transition has been discussed in CeB_6, where the Ce atom with $4f^1$ electron configuration has Γ_8 quartet ground state of which symmetry is identical to the J_{eff} = 3/2 quartet.

We focused on a rhenium double perovskite oxide Ba_2CaReO_6, which is a candidate of the J_{eff} = 3/2 Mott insulator with Re^{6+} ($5d^1$) ions. The magnetization of Ba_2CaReO_6 was measured in the pulsed high magnetic field by changing the maximum magnetic field values up to 66 T as shown in Fig. 1 [5]. The magnetization curve at 4.2 K deviates from the linear behavior around 35 T and exhibits a steep increase at around 45 T, indicating the presence of a magnetic field induced phase transition. The full magnetic moment of Ba_2CaReO_6 estimated from the effective magnetic moment is 0.38 μ_B and thus the magnetization of 0.2 μ_B at the high field region is clearly smaller than the full moment. The magnetic field induced phase transition in Ba_2CaReO_6 was also clearly detected in the magnetostriction $\Delta L/L_{0T}$ measured at 4.2 K as shown in Fig. 2. The longitudinal magnetostriction is positive and amounts to 2-3 $\times 10^{-4}$ at around 60 T, while the transverse magnetostriction is negative and amounts to ~1 $\times 10^{-4}$ at around 60 T. The longitudinal magnetostriction is plotted against magnetization in the inset of Figure 2. The magnetostriction changes quadratically to magnetization up to around 40 T. The deviation from the quadratic behavior is observed as increasing the field, suggesting a change in the way of spin-lattice coupling via orbital degrees of freedom. The magnetic field induced phase transition is attributed to the transition from the collinear to the canted antiferromagnetic orders with possible changes in the orbital states. Ba_2CaReO_6 would reside in the parameter regime close to the boundary between the two magnetic orders, representing a suitable material for investigating the interplay between the spin-orbital entangled electrons and magnetic field.

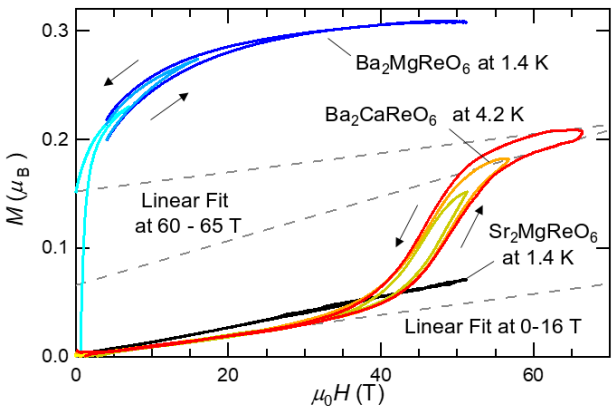

Fig. 1. Magnetization curves of Ba_2CaReO_6 measured up to 66 T (red) and those of relative compounds Ba_2MgReO_6 (blue) and Sr_2MgReO_6 (black).

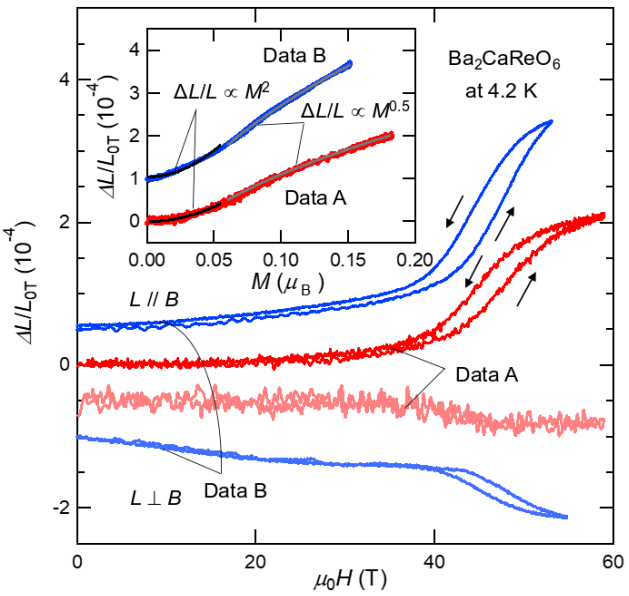

Fig. 2. Magnetostriction $\Delta L/L_{0T}$ of Ba_2CaReO_6 measured at 4.2 K. The magnetostriction with positive and negative values correspond to the longitudinal and transverse magnetostriction, respectively. The longitudinal magnetostriction is plotted against the magnetization in the inset.

References

[1] H. Ishikawa, T. Takayama, R. K. Kremer, J. Nuss, R. Dinnebier, K. Kitagawa, K. Ishii, and H. Takagi, Phys. Rev. B, **100**, 045142 (2019).
[2] H. Ishikawa, T. Yajima, A. Matsuo, Y. Ihara, and K. Kindo, Phys. Rev. Lett. **124**, 227202 (2020).
[3] H. Ishikawa, T. Yajima, A. Matsuo, and K. Kindo, J. Phys.: Condens. Matter **33**, 125802 (2021).
[4] D. Hirai, H. Sagayama, S. Gao, H. Ohsumi, G. Chen, T. Arima, and Z. Hiroi, Phys. Rev. Research **2**, 022063 (2020).
[5] H. Ishikawa, D. Hirai, A. Ikeda, M. Gen, T. Yajima, A. Matsuo, Y. H. Matsuda, Z. Hiroi, and K. Kindo Phys. Rev. B **104**, 174422 (2021).

Authors

H. Ishikawa, D. Hirai, A. Ikeda, M. Gen, T. Yajima, A. Matsuo, Y. H. Matsuda, Z. Hiroi, and K. Kindo

New Material Exhibiting the Interplay between Non-magnetic 3*d*-electron Kagome Bands and 4*f*-electron Magnetism

Kindo, Ozaki, and Tokunaga Groups

Kagome lattice, a two-dimensional network made of corner shared triangles, has attracted condensed matter physicists as a platform for realizing novel electronic states. A localized spin system on the kagome lattice is a typical example that exhibits a quantum spin liquid ground state due to the geometrical frustration. Itinerant electrons on the kagome lattice produces a band structure with uncommon features such as a Dirac point, van Hove singularity, and a flat band and may host unconventional density wave orders or superconductivity. Experimentally, 3*d* transition metal compounds with kagome lattice have been investigated in search for novel correlated electronic phases. Kagome cuprates are candidates for the Mott insulator with a quantum spin liquid ground state. Intermetallic compounds with the kagome layers of Cr, Mn, Fe, and Co have been investigated in recent years as a metal with large anomalous Hall effect and novel band structures. Recently, a series of vanadium

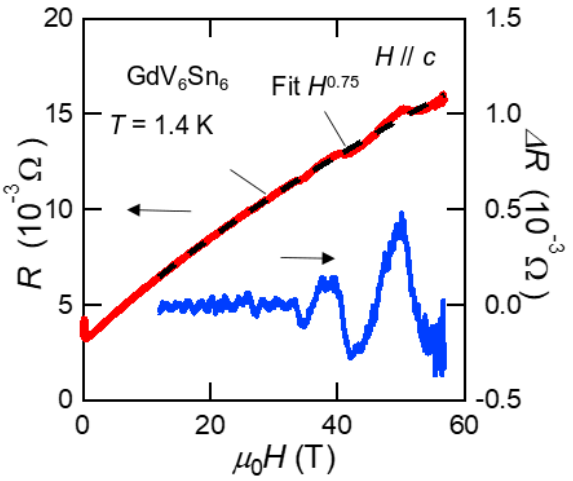

Fig. 1. Magnetoresistance of GdV_6Sn_6 at 1.4 K measured up to 56 T in pulsed magnetic field. A fit to $H^{0.75}$ magnetic field dependence, which is used to estimate the oscillating component ΔR, is shown by the dashed line.

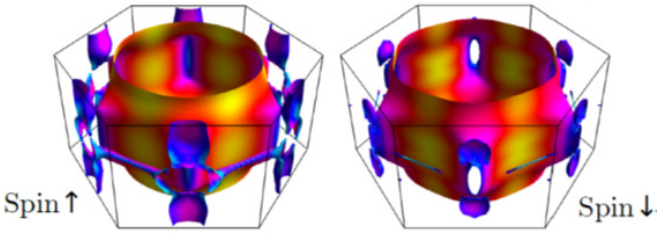

Fig. 2. Fermi surface plot of GdV_6Sn_6 including the effect of spin splitting.

antimonide AV_3Sb_5 (A = K, Rb, Cs) have attracted considerable attention as a new member of the kagome metal. AV_3Sb_5 compounds exhibit various phenomena such as the co-existence of charge density wave (CDW) order and superconductivity and the anomalous Hall effect without a magnetic order, suggesting that vanadium kagome metal is a promising platform for investigating unconventional electronic properties. Kagome layers made of vanadium are found in a series of stannide RV_6Sn_6 (R = Rare Earth), which are discovered in 2011 in the polycrystalline form [1]. Their physical properties are not investigated in the first report. The short V-V distances of approximately 2.7 Å may produce metallic conductivity within the kagome layer as seen in AV_3Sb_5. The variety of the rare earth ions, which separate the kagome layers instead of alkaline metals in AV_3Sb_5, may allow us to tune the physical properties.

We synthesized the high-quality single crystals of GdV_6Sn_6 and YV_6Sn_6 and investigate their electronic properties for the first time [2]. We revealed that GdV_6Sn_6 exhibits unique magnetotransport properties at low-temperature such as non-linear Hall resistivity and increase of resistance R in magnetic field H as $R \sim H^{0.75}$ up to 56 T with Shubnikov–De Haas oscillations as shown in the Fig. 1. The first principles band structure calculations revealed the presence of multiple Fermi surfaces with Dirac-like band crossings near the Fermi-energy as shown in the Fig. 2. The presence of multiple carriers is consistent with the non-linear Hall resistivity. The observed Shubnikov–De Haas oscillations can be attributed to the small Fermi pockets. The non-magnetic analogue YV_6Sn_6 turned out to exhibit similarly non-linear Hall resistivity, suggesting the two compounds host common electronic structure arising from the V-kagome layer. Moreover, a magnetic transition was observed at 5 K in GdV_6Sn_6. The magnetic order causes the negative magnetoresistance at weak magnetic field region below 1 T, which is absent in the non-magnetic YV_6Sn_6, pointing to a coupling between Gd-spins on the triangular lattice and carriers in the V-kagome layer. Our results demonstrate that RV_6Sn_6 family including GdV_6Sn_6 provide a new class of material to investigate the interplay between itinerant non-magnetic 3d-electron with bands inherent to the kagome lattice and magnetism of the 4f-electron on the triangular lattice.

References
[1] L. Romaka, Y. Stadnyk, V. V. Romaka, P. Demchenko, M. Stadnyshyn, and M. Konyk, J. alloys compd. **509**, 8862 (2011).
[2] H. Ishikawa, T. Yajima, M. Kawamura, H. Mitamura, and K. Kindo, J. Phys. Soc. Jpn. **90**, 124704 (2021).

Authors
H. Ishikawa, T. Yajima, M. Kawamura, H. Mitamura, and K. Kindo

Extraordinary π-electron Superconductivity in a Doped Quantum Spin Liquid

Kindo and Kohama Group

The realization of high-T_c superconductivity is one of the holy grails of condensed matter physics. As one idea to achieve this, P. W. Anderson proposed a possible pathway to the glory in 1987 just after the discovery of the high-T_c cuprates [1]. Strong geometric frustration of magnetically interacting spins suppresses magnetic orders, resulting in a quantum spin liquid (QSL) state. Sufficient carrier doping into a QSL yields mobility of the electrons keeping the correlated spin correlations, which perhaps lead to high-T_c charged superconducting pairs using the spin fluctuations. Nevertheless, it has been challenging to make superconductivity in a doped QSL stable in actual materials, and thus, the experimental understanding of the frustration effect on superconductivity has been less well developed.

Recently, several papers [2,3] reported that the organic superconductor, κ-$(BEDT\text{-}TTF)_4Hg_{2.89}Br_8$ (κ-HgBr), is one of the most plausible candidates for doped QSLs hosting superconductivity. This salt is classified into the strongly correlated dimer-Mott system and has the almost regular

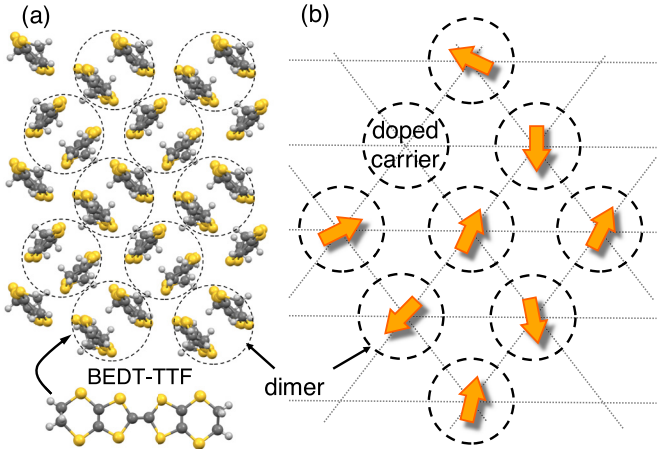

Fig. 1. (a) Molecular arrangement of the organic molecules in the two-dimensional organic layers in κ-HgBr. The dotted circles denote the molecular dimers forming the triangular lattice. (b) Schematic of the dimer lattice. The arrows represent spins of π-electrons.

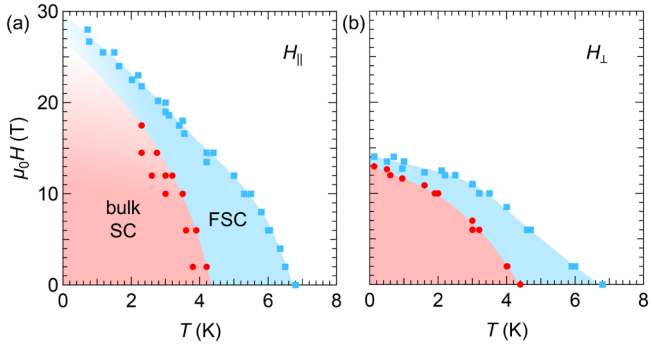

Fig. 2. Field-temperature superconducting phase diagrams in parallel (a) and perpendicular (b) fields. The blue and red shaded areas highlight the regions of the fluctuating superconductivity (FSC) and bulk superconductivity, respectively. The circles denote T_c whereas the boxes signify temperatures where FSC appears.

triangular lattice of the dimers, as shown in Fig. 1. Indeed, its magnetism can be described by antiferromagnetically interacting spins on a triangular lattice and does not exhibit any magnetic orders even at low temperatures. Thanks to the carrier doping by the nonstoichiometric ratio of the HgBr counter anions, the electronic state is an 11% hole-doped state from the half-filled Mott insulator, leading to metallic conductivity as well the superconductivity.

In this work [4], using various high-field measurements, we revealed that the superconductivity that emerged from the doped QSL exhibits unique field-temperature superconducting phase diagrams, as shown in Fig. 2. The red area represents the region of bulk superconductivity (SC) while the blue area indicates the region of fluctuating superconductivity (FSC). In a magnetic field, superconductivity is suppressed by the paramagnetic pair breaking effect and the orbital pair breaking effect, which yields limits of the upper critical field H_{c2} known as the Pauli limit H_P and orbital limit H_{orb}. When applying magnetic fields parallel to the superconducting plane for two-dimensional superconductivity, the orbital pair breaking effect is quenched and H_P governs H_{c2}. As H_P is proportional to the amplitude of the superconducting energy gap, the coupling strength of the superconductivity can be roughly estimated by the ratio H_{c2}/T_c. As shown in Fig. 2(a), amazingly, H_{c2}/T_c for κ-HgBr exceeds 6 TK^{-1}, which is much larger than not only 1.84 TK^{-1} expected in the conventional BCS framework, but also ~3 TK^{-1} observed in other strong-coupling organic superconductors. Besides, H_{c2}/T_c in perpendicular fields (Fig. 2(b)) reaches about 3 TK^{-1}, which is also much larger than those of other superconductors. Considering the results including the orbital limit in perpendicular fields, the superconductivity in κ-HgBr is realized by the extremely strong pairing of the anomalously heavy π-electrons. We discuss the origin of these anomalous features of the superconductivity and elucidate that these originate from quantum critical behavior developed near a quantum critical point of the QSL insulating phase.

In addition, we find that FSC appears even much above T_c (see the blue area in Fig. 2) compared to other organic superconductors. It is not clear at present why the fluctuation region appears in the wide temperature range above T_c, however, given the characteristic of the geometrical frustration to hinder long-range orders of spin-singlet pairing, this nature may be attributed to a characteristic of the superconductivity appearing in doped QSLs.

References
[1] P. W. Anderson, Science **235**, 1196 (1987).
[2] H. Oike, K. Miyagawa, H. Taniguchi, and K. Kanoda, Phys. Rev. Lett. **114**, 067002 (2015).
[3] H. Oike, Y. Suzuki, H. Taniguchi, Y. Seki, K. Miyagawa, and K. Kanoda, Nature Commun. **8**, 756 (2017).
[4] S. Imajo, S. Sugiura, H. Akutsu, Y. Kohama, T. Isono, T. Terashima, K. Kindo, S. Uji, and Y. Nakazawa, Phys. Rev. Research **3**, 033026 (2021).

Authors
S. Imajo, S. Sugiura[a], H. Akutsu[b], Y. Kohama, T. Isonoc, T. Terashima[c], K. Kindo, S. Uji[c], and Y. Nakazawa[b]
[a]Tohoku University
[b]Osaka University
[c]National Institute for Materials Science

Approaching the Best Wire for Non-Destructive Pulsed Magnet

Kindo Group

Non-destructive pulsed magnet is the most important tool for a precise measurement under very high magnetic field. Generating high magnetic field, however, has been hard task because the magnet is destroyed due to considerable Maxwell stress. The stress reaches about 2 GPa in the field of 70 Tesla(T). The simplest solution for generating high field non-destructively is making the coil-wire strong. Cu-Ag wire has been the best candidate for the coil-wire because the wire has the tensile strength of about 1.1 GPa and the conductivity of about 80% of copper. By using the wire, we succeeded in generating a field of 85.8 T in 2011. The best wire, unfortunately, was an accidental success. The wire was not reproduced though we continued to produce wires with similar physical properties. There were many wires having the same strength and conductivity but nothing could generate the field exceeding 80 T. This would be a mystery because the maximum field depends on the tensile strength of the wire mainly. Our efforts to reproduce the best wire were in vain. 10 years have passed since it became mystery.

To solve the mystery, we firstly classified the wire into good ones and bad ones. This classification indicated clearly that the quality of the wire depends on the manufacturing process, especially drawing one. In November 2021, we tested a wire regarded as an ideal combination of manufacturing process. Figure 1 shows the waveform of the magnetic

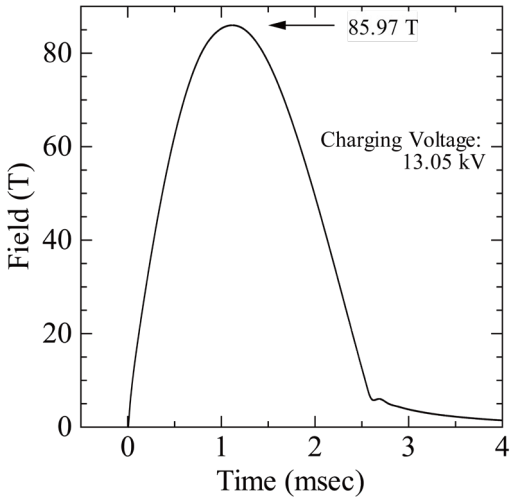

Fig. 1. The shape of completely non-destructive magnetic field of 85.97 Tesla.

field generated using this wire. There was no distortion of the waveform from the start to the end of the magnetic field generation, and we succeeded in generating a magnetic field of 85.97 T completely non-destructively, breaking the previous record.

The mystery of Cu-Ag wire was solved. The mystery lay in the manufacturing process, especially drawing one. Based on these results, we will develop wires that have undergone the ideal manufacturing process to generate even higher magnetic fields, and will provide a 100 T fields non-destructively contributing the joint research program.

Authors
K. Matsui, A, Matsuo, and K. Kindo

Particle-Hole Symmetry Breaking in a Spin-Dimer System $TlCuCl_3$ Observed at 100 T

Y. H. Matsuda and Kindo Group

In a pure dimer system, the transition between singlet state and the S_z = 1-triplet state under an external magnetic field drives a phase transition at the critical magnetic field $H_g \equiv \Delta/g\mu_B$ with Δ the spin gap. The H_g separates into two distinct critical points H_{c1} and H_{c2} in real spin-gap materials due to interdimer interactions; these two critical magnetic fields correspond to the beginning and saturation of the magnetization, respectively. It has been proposed that the field-induced ordering phase at H_{c1} in the dimer system with finite interdimer interactions (a three-dimensional S = 1/2 spin-gap dimer system) can be interpreted as a Bose-Einstein condensation (BEC) phase of magnons [1]. For a long time, this field-induced ordering phase at H_{c2} was thought to be the BEC phase of holes of magnons [2], e.g., the magnetic-field dependence of the order parameters in phase diagrams has a symmetry with respect to the particle-hole invariant point $H = (H_{c1} + H_{c2})/2$. However, the universality of this symmetry has been questioned in strong interdimer interaction system.

In present work, we study the magnetization (M) process of $TlCuCl_3$ (a strong interdimer interaction spin system) up to 100 T and discuss the particle-hole symmetry breaking of the BEC phase [3]. Figure 1 shows the magnetization process and the magnetic field dependence of the dM/dH at 2 K; the magnetization data simulated by the quantum Monte Carlo (QMC) calculation is also presented for the comparison of the M-H curves. The magnetization curve (M-H curve) has a monotonous convex downward shape, which manifests the difference between the critical behaviors around H_{c1} and H_{c2} and implies the absence of the particle-hole symmetry in $TlCuCl_3$.

The breaking of symmetry can be simply understood in the bond operator theoretical formalism. The magnetism around H_{c1} is contributed to by the outset of lowest triplet $|\uparrow\uparrow>$, namely, S_z = 1 condensations driven by the vanishing spin gap. In the pure-dimer limit $J_{intra} >> J_{inter}$, the other two higher-energy local excitations ($|\uparrow\downarrow> + |\downarrow\uparrow>$) and $|\downarrow\downarrow>$ can be neglected since they hardly affect the low-temperature physics. However, a finite J_{inter} interaction can mediate a four-particle interaction that accumulates highest-triplet $|\downarrow\downarrow>$ excitations in the presence of a partial lowest-triplet condensation and singlet condensation [4]. Therefore, $|\downarrow\downarrow>$

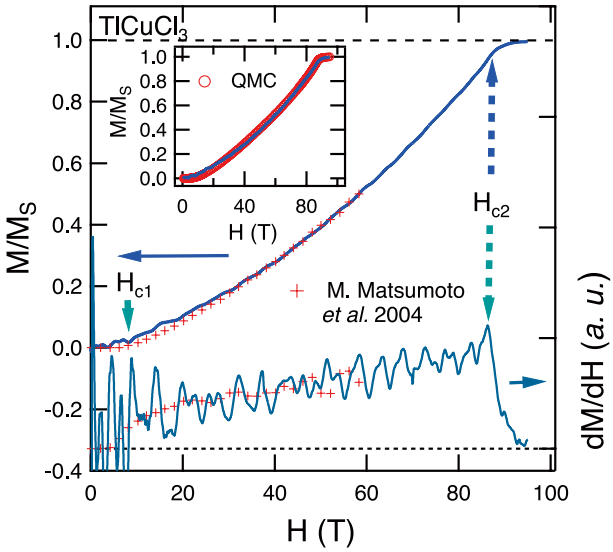

Fig. 1. The magnetization curve measured up to 95 T, as well as the dM/dH data. Red marks represent the results of Ref. [4]. The inset shows Comparison between the experimental magnetization curve and the QMC simulation results.

excitations suppress the magnetization from the $|\uparrow\uparrow>$ condensations when $H \gtrsim H_{c1}$. When the magnetic field increases beyond H_{c1}, such a suppression eventually becomes inefficient due to a large Zeeman gap to excite a $|\downarrow\downarrow>$ quasiparticle and is negligible near H_{c2}. Therefore, it can be concluded that the particle-hole symmetry in the weak interdimer spin system is broken in $TlCuCl_3$ due to the strong higher-order terms through the interdimer interactions.

References
[1] T. Nikuni, M. Oshikawa, A. Oosawa, and H. Tanaka, Phys. Rev. Lett. **84**, 5868 (2000).
[2] M. Jaime, V. F. Correa, N. Harrison, C. D. Batista, N. Kawashima, Y. Kazuma, G. A. Jorge, R. Stein, I. Heinmaa, S. A. Zvyagin, Y. Sasago, and K. Uchinokura, Phys. Rev. Lett. **93**, 087203 (2004).
[3] X.-G. Zhou, Y. Yao, Y. H. Matsuda, A. Ikeda, A. Matsuo, K. Kindo, and H. Tanaka, Phys. Rev. Lett. **125**, 267207 (2020).
[4] M. Matsumoto, B. Normand, T. M. Rice, and M. Sigrist, Phys. Rev. B **69**, 054423 (2004).

Authors
X.-G. Zhou, Yuan Yao, Y. H. Matsuda, A. Ikeda, A. Matsuo, K. Kindo, and H. Tanaka[a]
[a]Tokyo Institute of Technology

Two Spin-State Crystallizations in $LaCoO_3$ up to 200 T

Y. H. Matsuda Group

The puzzling properties of $LaCoO_3$ have been drawing the attention of researchers for more than 60 years, regarding the uncovered origin of the magnetic and insulating state at intermediate temperature range of 100 - 500 K. $LaCoO_3$ is characterized by the spin-state degrees of freedom that governs the temperature evolution of the electronic and magnetic properties. The origin of the magnetic and insulating state between 100 - 500 K is quite controversial, although it has been widely accepted that the ground state is the low spin (LS) non-magnetic insulator. As the origin of the magnetic states, some argue that the intermediate spin state (IS) is involved, while others claim that the mixture of the LS and high spin (HS) states is important. Many experimental results support each claim, being unable to put an end

to the long-standing discussion. We believe that this controversy is rooted in the itineracy-localization duality of correlated electrons in $LaCoO_3$.

We tackled this long-standing problem by using pulsed ultrahigh magnetic field beyond 100 T because beyond 100 T are supposed to be useful in controlling the excited spin-states. In the previous study of ours, we discovered two kinds of spin-state orderings, α and β phases that are extended beyond 100 T on the *B*-*T* phase diagram [1], by means of magnetization measurements using the induction method. However, the magnetization study shows only little information on the difference between the uncovered α and β phases, especially regarding the spin-state configurations.

We came up with an idea that magnetostriction measurement will supplement the magnetization study because the spin-state degree of freedom is coupled with the lattice volume even more directly than magnetization is. For this purpose, we have developed an ultrahigh speed magnetostriction measurement instrument utilizing the fiber Bragg grating (FBG) and optical filter method [2], for the measurement above 100 T. By means of the FBG based method, we have successfully revealed the magneto-lattice properties of $LaCoO_3$ up to 200 T [3]. The result shows very clearly that α and β phases are quite different in volume and that both have constant volume above 100 T, indicating both phases are super-lattice formations (crystallizations) of the spin-states. We have claimed several possible crystallizations in the paper [3]. The result clearly shows that the spin-state interactions lead to kinds of long-range ordering in $LaCoO_3$. At this moment, we still do not know why the ordering is present only in high magnetic fields. We further push the study to even higher magnetic field of 600 T using electromagnetic flux compression method and FBG based magnetostriction measurements, which have clarified even exotic phase diagram up to 600 T [4].

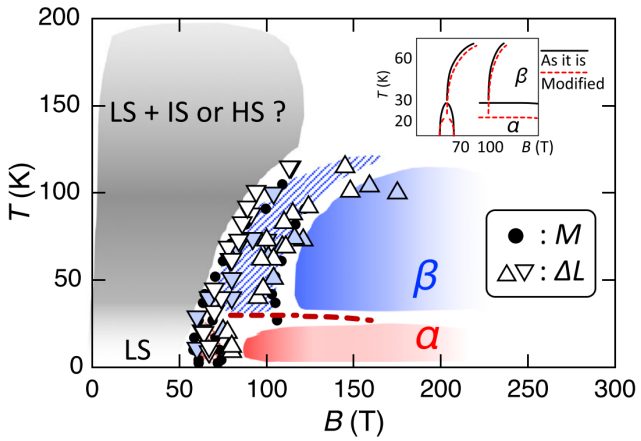

Fig. 1. Phase diagram of $LaCoO_3$ uncovered by the FBG based magnetostriction measurement up to 200 T.

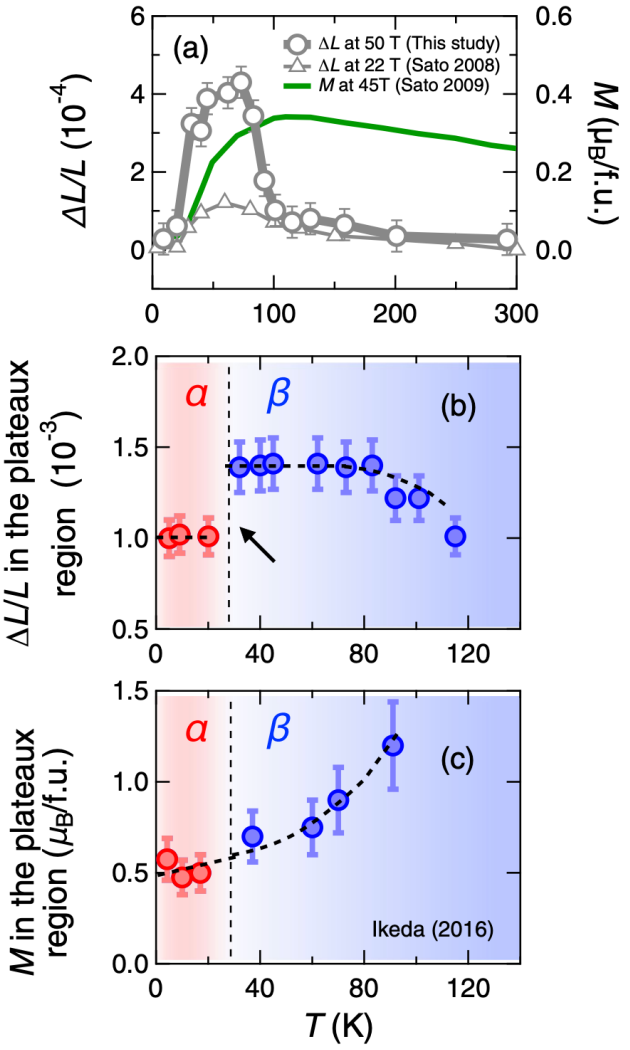

Fig. 2. Comparison of the temperature dependence between magnetization and magnetostriction at $B \sim 50$ T and 100 T and the sample temperatures from 4.2 to 300 K.

References

[1] A. Ikeda, T. Nomura, Y. H. Matsuda, A. Matsuo, K. Kindo, and K. Sato, Phys. Rev. B **93**, 220401(R) (2016).
[2] A. Ikeda, T. Nomura, Y. H. Matsuda, S. Tani, Y. Kobayashi, H. Watanabe, K. Sato, Rev. Sci. Instrum. **88**, 083906 (2017).
[3] A. Ikeda, Y. H. Matsuda, and K. Sato, Phys. Rev. Lett. **125**, 177202 (2020).
[4] A. Ikeda, Y. H. Matsuda, K. Sato, Y. Ishii, H. Sawabe, D. Nakamura, S. Takeyama, and J. Nasu, arXiv:2201.02704.

Authors
A. Ikeda[a], Y. H. Matsuda and K. Sato[b]
[a]University of Electro-Communications
[b]National Institute of Technology

Magnetic Field-Induced Phenomena in the Unconventional Superconductor UTe_2

Tokunaga Group

Unconventional superconductivity in UTe_2 is one of the hot topics in strongly correlated electron systems. The spin-triplet superconductivity is very likely because of its extremely high superconducting (SC) critical fields. Since its discovery three years ago, many experimental and theoretical works with intense competition revealed novel phenomena realized in UTe_2 [1]. External parameters, such as pressure and magnetic field (*H*), strongly affect superconductivity and magnetism in UTe_2. One of the intriguing phenomena induced by applied *H* is the reinforcement and reemergence of SC phases, which are sensitive to the *H* directions [2]. When the *H* applied along a hard magnetization *b* axis, the *H* reinforces the SC transition above 15 T. With increasing *H*, the superconducting transition temperature T_{sc} increases and is suppressed above $\mu_0 H_m \sim 35$ T, where a first-order metamagnetic transition takes place (see Fig. 1(b)) [3]. More surprisingly, the *H* along near the [011] direction induces another SC phase above H_m [2]. Thus, the metamagnetic

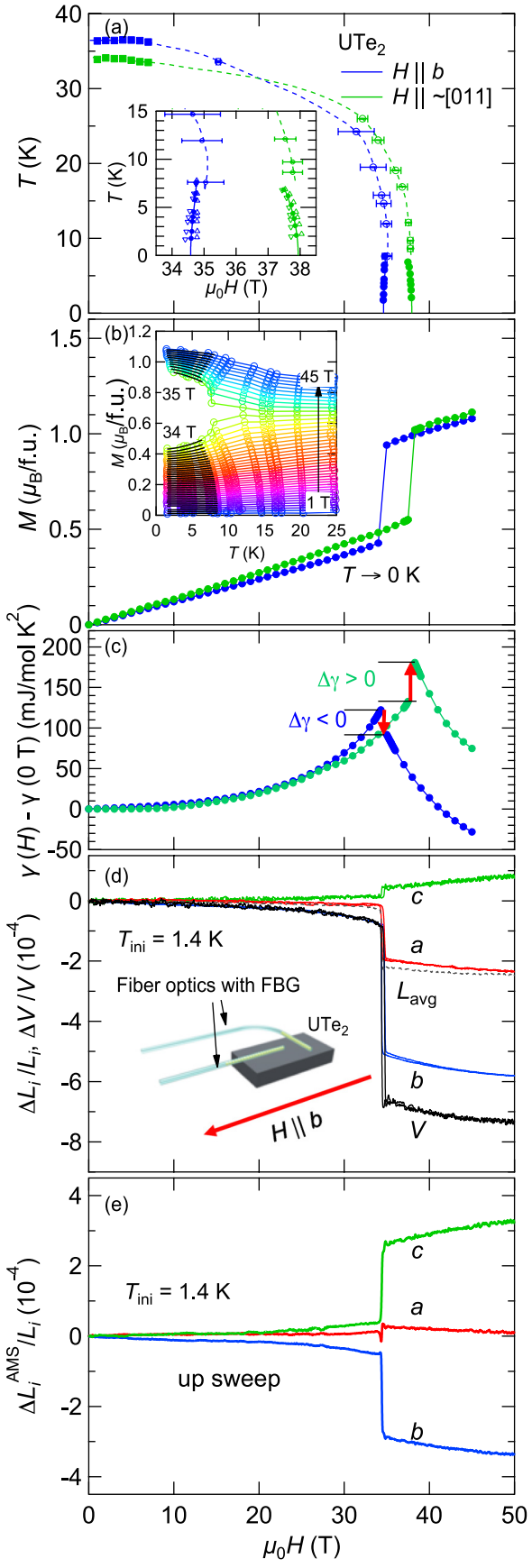

Fig. 1. (a)Phase diagrams of UTe_2 for $H \parallel b$ and ~[011]. The inset zooms near H_m. The filled (open) circles and squares indicate H_m (crossover) and T_χ^{max}, respectively. Magnetic field dependences of (b) magnetization extrapolated to 0 K, (c)electronic specific heat coefficient derived by thermodynamic relations, (d)linear and volume magnetostriction at T_{ini} = 1.4 K and (e)anisotropic magnetostriction at T_{ini} = 1.4 K.

transition strongly affects the SC transition. However, their relationship and the origin of metamagnetism leave many mysteries. Using state-of-the-art pulsed-high-field experiments developed in the International MegaGauss Science Laboratory at the ISSP, we have studied H-induced phenomena in UTe_2.

In order to address the relationship between metamagnetic and SC transition, we revealed the mass enhancement as a function of the magnetic field and its direction [4]. In general, the larger the density of state, the higher T_{sc} is. Field dependence of the electronic specific heat coefficient, γ (H), is derived thermodynamically by analyzing the T dependence of magnetization (M) at constant fields and phase diagram. Since the magnetocaloric effect (MCE) is significant [5], the sample temperature varies during the H sweep. To account for the MCE, we measure the sample T and M simultaneously using field-insensitive capacitance thermometers developed by Miyake et al. [6]. This method is also potent in determining the magnetic phase diagram more precisely.

The inset of Fig. 1 (b) shows the M (T) curves at constant H. On approaching H_m, T decreases significantly. This M (T, H) evaluation is the first attempt and a considerable breakthrough in the pulsed-field experiments. The sign change in dM/dT across H_m indicates the existence of a peak of γ (H) at H_m from Maxwell's relation. The γ (H) should change discontinuously across H_m because of the first-order transition. We solved this issue by employing Clausius-Clapeyron's equation. As shown in Fig. 1(a), dH_m/dT changes in its sign from positive for $H \parallel b$ to negative for $H \parallel$ ~[011]. This change means that the negative $\Delta\gamma$ (H) crossing H_m for $H \parallel b$ changes to positive for $H \parallel$ ~[011] [see Fig. 1(c)]. The negative (positive) $\Delta\gamma$ (H) for $H \parallel b$ (~[011]) is consistent with the suppression (reemergence) of SC at H_m. These findings hint at understanding the origin of the SC phases varying with the field directions.

Since the metamagnetic transition is of the first order, the volume at least should change across H_m. Thus, we tried to reveal volume/structural change, namely lattice instability, at H_m through the magnetostriction [7]. We performed magnetostriction measurements using the optical fiber with fiber-Bragg-grating and the optical filter method developed in Ikeda *et al.* [8]. The inset of Fig. 1 (d) is a schematic drawing of the setup for the magnetostriction measurements. The bare fiber optics were glued directly on the sample parallel and perpendicular to the field direction along the b axis, as in Ref. [9]. This method enables us to obtain the longitudinal and transverse magnetostriction simultaneously, the first example in pulsed fields.

$\Delta L_i/L_i$'s (i = a, b, c) show anisotropic H dependencies and change discontinuously at H_m, as expected for the first-order transition (Fig. 1 (d)). The volume magnetostriction $\Delta V/V$, i.e., a summation of $\Delta L_i/L_i$, shows a discontinuous change of -5.9×10^{-4} at H_m. Knowing ΔV and ΔM at H_m, we can estimate pressure (p) dependence of H_m from Clausius-Clapeyron's equation. The $H_m(p)$ obtained by the thermodynamic quantities are in good agreement with the $H_m(p)$ determined experimentally, confirming the reliability of our experiments. An important finding here is the anisotropic magnetostriction (AMS) defined as $\Delta L_i^{AMS}/L_i = \Delta L_i/L_i - \Delta L_{avg}/L_{avg}$ (the averaged linear magnetostrcition $\Delta L_{avg}/L_{avg} = \Delta V/3V$). For the isotropic case, the AMS is small. Interestingly, the strong anisotropy appears in the bc plane, while $\Delta L_a^{AMS}/L_a$ is very small. Thus, the metamagnetic transition in UTe_2 involves the lattice instability, which plays a crucial role in the SC phases near H_m. We also suggest the possible

valence instability in terms of the itinerant-localized duality picture of the uranium magnetism [7].

Without experimental developments, the fascinated *H*-induced phenomena in UTe_2 are not entirely solved. In other words, UTe_2 is our good trainer experimentally and physically. Our struggles for a complete understanding continue.

References

[1] D. Aoki, J.-P. Brison, J. Flouquet, K. Ishida, G. Knebel, Y. Tokunaga, and Y. Yanase, J. Phys.: Condens. Matter **34**, 243002 (2022).
[2] S. Ran, I.-L. Liu, Y. S. Eo, D. J. Campbell, P. Neves, W. T. Fuhrman, S. R. Saha, C. Eckberg, H. Kim, J. Paglione, D. Graf, J. Singleton, and N. P. Butch, Nat. Phys. **15**, 1250 (2019).
[3] A. Miyake, Y. Shimizu, Y. J. Sato, D. Li, A. Nakamura, Y. Homma, F. Honda, J. Flouquet, M. Tokunaga, and D. Aoki, J. Phys. Soc. Jpn. **88**, 063706 (2019).
[4] A. Miyake, Y. Shimizu, Y. J. Sato, D. Li, A. Nakamura, Y. Homma, F. Honda, J. Flouquet, M. Tokunaga, and D. Aoki, J. Phys. Soc. Jpn. **90**, 103702 (2021).
[5] S. Imajo, Y. Kohama, A. Miyake, C. Dong, J. Flouquet, K. Kindo, and D. Aoki, J. Phys. Soc. Jpn. **88**, 083705 (2019).
[6] A. Miyake, H. Mitamura, S. Kawachi, K. Kimura, T. Kimura, T. Kihara, M. Tachibana, and M. Tokunaga, Rev. Sci. Instrum. **91**, 105103 (2020).
[7] A. Miyake, M. Gen, A. Ikeda, K. Miyake, Y. Shimizu, Y. J. Sato, D. Li, A. Nakamura, Y. Homma, F. Honda, J. Flouquet, M. Tokunaga, and D. Aoki, J. Phys. Soc. Jpn. **91**, 063703 (2022).
[8] A. Ikeda, Y. H. Matsuda, and H. Tsuda, Rev. Sci. Instrum. **89**, 096103 (2018).
[9] M. Gen, A. Miyake, H. Yagiuchi, Y. Watanabe, A. Ikeda, Y. H. Matsuda, M. Tokunaga, T. Arima, and Y. Tokunaga, Phys. Rev. B **105**, 214412 (2022).

Authors

A. Miyake, M. Gen[a], A. Ikeda[b], K. Miyake[c], Y. Shimizu[d], Y. J. Sato[d], D. Li[d], A. Nakamura[d], Y. Homma[d], F. Honda[d, e], J. Flouquet[f], M. Tokunaga, and D. Aoki[d, f]

[a]The University of Tokyo
[b]University of Electro-Communications
[c]Osaka University
[d]Tohoku University
[e]Kyushu University
[f]CEA-Grenoble

Ultrasound Measurement under Ultrahigh Magnetic Fields

Kohama and Y. H. Matsuda Groups

Ultrasound is a powerful means to study numerous phenomena of condensed-matter physics as acoustic waves coupling strongly to structural, magnetic, orbital, and charge degrees of freedom. In this work, we have developed a new ultrasound measurement technique combined with the single-turn coil (STC) system, generating magnetic fields beyond 100 T [1].

Figure 1 summarizes the concepts of the ultrasound pulse-echo (PE) and continuous-wave excitation (CW) techniques. Usually, ultrasound measurements under pulsed magnetic fields are performed with the PE technique, where the pulsed ultrasound is excited and the transmitted echo signals are analyzed by a phase-sensitive technique. In this case, cross-talk noise and higher echoes that arrive after multiple reflections are separated in time. However, magnetic fields above 100 T are accessible only by destructive techniques, which generate fields only for several microseconds. This field duration is too short to perform PE ultrasound measurements. Instead, we have employed the CW technique, which excites and detects ultrasound waves continuously. In this case, the detected signal contains all echo signals. Only if the 0th echo signal is dominant, the

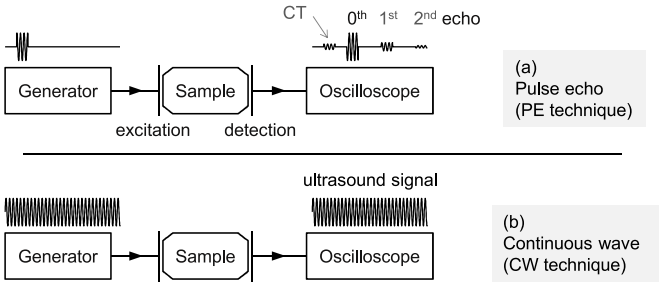

Fig. 1. Schematics of the (a) pulse-echo and (b) continuous-wave ultrasound techniques. Here, CT means crosstalk.

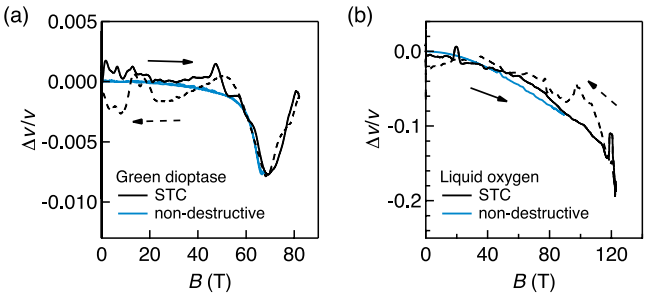

Fig. 2. Relative change in the sound velocity of (a) green dioptase at 4 K and (b) liquid oxygen at 77 K.

detected signal reflects the change of sound velocity. This condition is reasonably satisfied in various magnetic phase transitions, where acoustic attenuation increases and higher-echo signals do not affect the measurements. Therefore, the CW technique can be applied for detecting phase transitions under ultrahigh magnetic fields.

Figure 2 shows representative results on green dioptase and liquid oxygen. Results obtained by the STC (black) are compared with the ones by non-destructive magnets (cyan). These results reasonably coincide despite the significant difference in the field durations by the factor of 1000 (10 ms/10 μs). For the case of green dioptase [Fig. 2(a)], an anomaly corresponding to the magnetic phase transition is observed at 65 T. Here, the measurement resolution is of the order of $\Delta v/v \sim 10^{-3}$, which is sufficient for detecting various field-induced phase transitions. For the case of liquid oxygen [Fig. 2(b)], a continuous decrease of sound velocity is observed up to 120 T with the significant softening of $\Delta v/v \sim -0.2$. The observed change in sound velocity is extremely large, and cannot be explained by a magneto-volume effect. We point out that this sound-velocity change could be a precursor of a field-induced liquid-liquid transition of oxygen [2]. Now, the developed technique is open to users.

References

[1] T. Nomura, A. Hauspurg, D. I. Gorbunov, A. Miyata, E. Schulze, S. A. Zvyagin, V. Tsurkan, Y. H. Matsuda, Y. Kohama, and S. Zherlitsyn, Rev. Sci. Instrum. **92**, 063902 (2021).
[2] T. Nomura, A. Ikeda, M. Gen, A. Matsuo, K. Kindo, Y. Kohama, Y. H. Matsuda, S. Zherlitsyn, J. Wosnitza, H. Tsuda, and T. C. Kobayashi, Phys. Rev. B **104**, 224423 (2021).

Authors

T. Nomura, A. Hauspurg[a], D. I. Gorbunov[a], A. Miyata[a], E. Schulze[a], S. A. Zvyagin[a], V. Tsurkan[b], Y. H. Matsuda, Y. Kohama, and S. Zherlitsyn[a]

[a]Hochfeld-Magnetlabor Dresden (HLD-EMFL)
[b]University of Augsburg

Developing Novel Spectroscopy Techniques Using a Segmented Cross Undulator

I. Matsuda Group

Cross undulators, composed of a single set of insertion devices for linear horizontal and vertical polarization with a phase shifter in between, have become available at worldwide synchrotron and x-ray free electron laser facilities. To achieve higher degree of the light polarization, a segmented type of the cross undulator, was designed and successfully installed at SPring-8 BL07LSU [1]. At the beamline, the continuous variation of the phase shifts has realized smooth polarization controls of soft X-ray beam between linear and circular ones with fast switching (13 Hz) [1]. The oscillatory regulation has allowed us to determine the element-specific complex permittivity in soft X-ray [1]. In the present research, we demonstrated a new control of linear polarization at any angle with a segmented undulator.

The segmented cross undulator at SPring-8 BL07LSU is composed of eight segments of insertion device (ID) and seven phase shifters (PSs), as shown in Fig. 1 (a). The ID segment is a horizontal figure-8 undulator or a vertical figure-8 undulator. The horizontal (H) and vertical (V) ID segments are placed alternatively and sandwich a PS. A PS is used to adjust the relative phase of radiation emitted from each segment by changing the path length of the electron orbit in magnetic field. To realize linearly polarized light with arbitrary angle, θ, we combine two waves of the left- and right-handed circularly polarized light, generated by sets of the ID segments, Set A and Set B, as shown in Fig.1(a). Set A or B is composed of the two H and two V segments. When Set A produces right-handed (left-handed) circular polarized light, we make Set B generate lefthanded (right-handed) circular polarized light. Then, the rotation angle (θ) of linearly polarized light is controlled by changing the phase shift between the left and right circularly polarized light at the center PS. In other words, we can generate soft X-ray beam with linear polarization that continuously rotates its angle over 2π.

For demonstration, we made measurements of near-edge X-ray absorption fine structure (NEXAFS) on a 2D film of h-BN (Fig. 1(b)) [2]. Focusing on the π* and σ* NEXAFS peaks, we traced their intensity variations with angle of the linear polarization, θ. Since this NEXAFS methodology is different from the conventional one, we hereafter call it the rotational NEXAFS measurement. When the incident angle is 80°, as illustrated in Fig. 1(c), intensity of hν = 401.5 eV (π*) becomes the maximum at θ = 0, π, 2π (horizontal) and the minimum at θ = π/2, 3π/2 (vertical), while that of hν=408.0 eV (σ*) shows the opposite, as shown in Fig. 1(d). The rotational NEXAFS experiment enhances the clear electronic contrast between the π* (out-of-plane) and σ* (in-plane) orbitals of h-BN. The experimental plot is expected to be useful in making assignments of the electronic states and in determining the precise configuration of molecules.

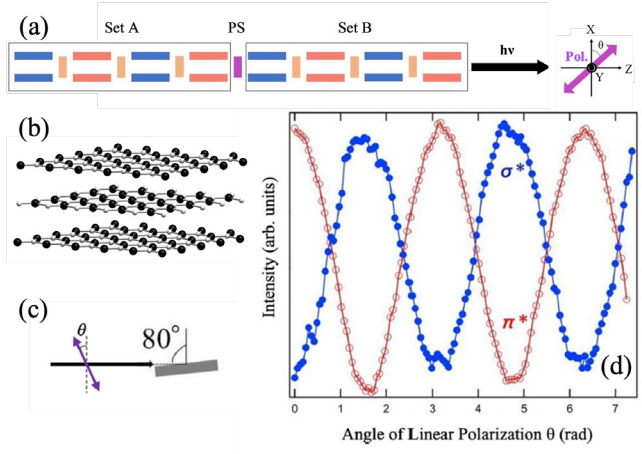

Fig. 1. (a) A schematic drawing of the segmented undulator with H (blue) and V (red) ID segments and PS's (orange). (b) An illustration of a h-BN film. (c) The measurement configuration. (d) The rotational NEXAFS spectra at the π* peak (hν = 401.5 eV) and the σ* peak (hν = 408.0 eV) [2].

Figure 2 shows another demonstration of the rotational X-ray spectroscopy experiment of the X-ray magnetic linear dichroism (XMLD) [3]. Figure 2 (a) shows an Ni L-edge XAS spectra of a NiO crystal taken with horizontal and vertical linearly polarized light at the incident angle of 80° from the surface normal. XMLD spectra of the NiO crystal is obtained by taking difference between the XAS spectra taken with the horizontal and vertical linear polarizations (Fig. 2 (b)), showing clear linear dichroisms. Focusing on the L2a and L2b peaks, the former has a large horizontal intensity, while the latter has a large vertical intensity. The spectral feature appears opposite in the XMLD signals. Figures 2(c,d) show results of the rotational XMLD, taken at the incident angle of 80°. The intensity changes with a period of π, showing a clear XMLD contrast. The reversed features between the ID section orders confirm the genuine XMLD signals (red and blue lines in the figure). The technique can

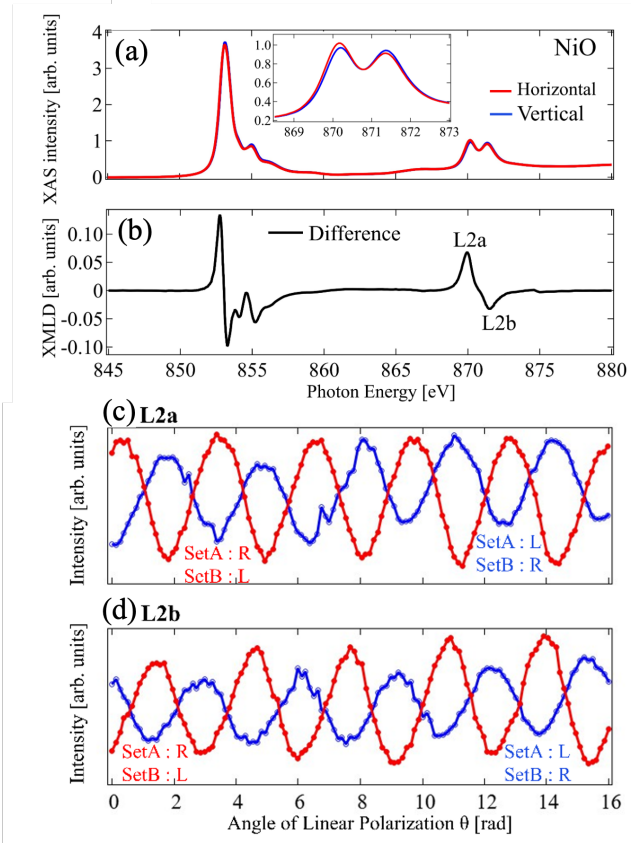

Fig. 2. (a) XAS and (b) XMLD spectra of a NiO crystal at the Ni L-edge and at an incident angle of 80°. In (a), the red (blue) curve indicates a spectrum, taken by the horizontal (verticals) linear polarization. (c)(d) Plots of the Rotational XMLD, shown as intensity at the L2a (hν = 869.95 eV) and L2b (hν = 871.55 eV) peaks at various angles of linear polarization. The red plot shows the results for Set A with right-handed polarization and Set B with left-handed polarization, while the blue plot shows the results with the opposite polarization configuration [3].

be combined with a lock-in-amplification and it is expected to detect fine magnetic signals of various materials.

References

[1] J. Miyawaki, S. Yamamoto, Y. Hirata, M. Horio, Y. Harada, and I. Matsuda, AAPPS Bulletin **31**, 25 (2021).
[2] Y. Kudo, Y. Hirata, M. Horio, M. Niibe, and I. Matsuda, Nucl. Instrum. Meth. Phys. Res. A **1018**, 165804 (2021).
[3] Y. Kudo, M. Horio, Y. Hirata, T. Ohkochi, T. Kinoshita, and I. Matsuda, e-J. Surf. Sci, Nanotechnol. **20**, 124 (2022).

Author

I. Matsuda

Visualization of the Strain-Induced Topological Phase Transition in a Quasi-One-Dimensional Superconductor $TaSe_3$

Kondo Group

The control of the phase transition from topological to normal insulators can allow for an on/off switching of the spin current. Topological phase transitions realized by elemental substitution [1] require the preparation of materials with various compositions and are thus far from a feasible device application, which demands a reversible operation.

In this study, we use angle-resolved photoemission spectroscopy (ARPES) and spin-resolved ARPES (SARPES) to visualize the strain-driven band-structure evolution of the quasi-one-dimension (quasi-1D) superconductor $TaSe_3$. Our results demonstrate that it undergoes reversible strain-induced topological phase transitions from a strong topological insulator phase with spin-polarized, quasi-one-dimensional topological surface states to topologically trivial semimetal and band insulating phases. The quasi-one-dimensional superconductor $TaSe_3$ provides a suitable platform for engineering the topological spintronics with the functionality to on/off switch a spin current that is robust against impurity scattering.

In the transition-metal trichalcogenides MX_3 (M = Nb, Ta; X = S, Se), physical properties vary and electronic orders evolve differently in accordance with the distinctive stacking sequences of the 1D chain variants [2]. Among them, $TaSe_3$ is especially appealing in that superconductivity emerges at low temperatures (~2 K) [3], in contrast with the other members, which typically undergo charge density wave transitions [2]. More intriguingly, recent ab initio calculations predict that semimetallic $TaSe_3$ belongs to a three-dimensional (3D) strong TI phase [4]. Therefore, it has been further suggested as a candidate for a topological superconductor with the topological surface states (TSSs) formed near E_F. Thanks to the van der Waals stacking of 1D chains [2] and the electronic proximity to other topological phases [4], $TaSe_3$ potentially brings an attractive functionality of controlling topological properties by fine-tuning of a single physical parameter, i.e., the lattice variation via strain.

In Fig. 1 [5], we demonstrate the first unambiguous confirmation of the strong TI phase in $TaSe_3$. Figures 1c,d shows the calculated and correspondingly experimental band dispersions around the Brillouin zone edge, where the TSSs are expected (the sharp features in Figs. 1c,d). To elucidate more details, we magnify the dispersions in Figs. 1e,f, where one can see clearly two branches of TSSs. Utilizing ultra-high resolution SARPES, we map the spin-resolved states in

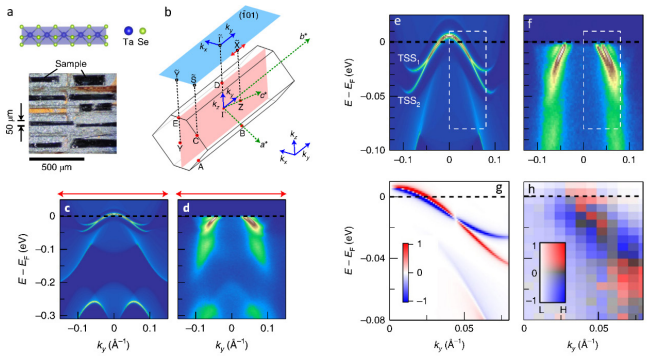

Fig. 1. Strong topological insulator phase in $TaSe_3$ revealed by ARPES [5]. (a) Crystal structure of the quasi-1D monoclinic $TaSe_3$ and a picture of single crystals mounted on a sample holder for ARPES measurements. (b) 3D bulk Brillouin zone and its 2D projection. (c, d) Calculated and experimental band dispersions along the red arrow in (b) near the zone edge where topological surface states (TSSs) are expected to emerge. (e, f) Magnified dispersions of (c, d) near E_F. Two branches of TSSs are observed. (g, h) Calculated and experimental spin-polarization maps in the energy-momentum window marked by the dashed box in (e, f). Measurement temperature was 10 K and a 7 eV laser was used as a light source.

Fig. 1h within the energy-momentum window specified by the dashed box in Fig. 1f. Correspondingly, the calculations are also shown in Fig. 1g. One can see that our results nicely reproduce the theoretical predictions of spin-polarized states with a spin-degenerated node point.

We have designed a device to apply strain to the quasi-1D crystals, based on a bending mechanism, as shown in Fig. 2a [5]. After tightening four screws, one can apply uniaxial tensile strain to the crystals mounted on the platform. This can be seen in Fig. 2b representing with color scale the distribution of longitudinal strain produced by the finite-element analysis. We also used commercial strain gauges to measure the strain values and confirmed a good agreement of those with the simulations [5]. Figures 2d-f show the band dispersions around the zone edge obtained under different strains tuned *in-situ*, revealing two-step phase transitions. At zero strain (Fig. 2d), one can see sharp and high-intense TSSs that are consistent with those shown in Figs. 1d,f. With increasing strain up to around 1%, the TSSs vanished (Fig. 2e) as a result of the topological phase transition, i.e., the band inversion is lifted and the bulk gap collapsed, turning the bulk state to the trivial semimetallic phase. As the strain reached 2.4%,

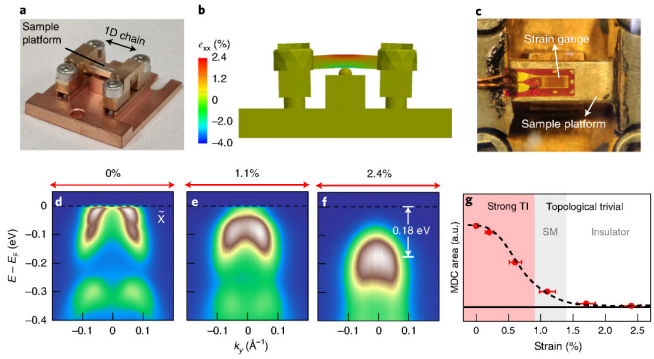

Fig. 2. Strain-induced topological and metal-insulator phase transitions revealed by ARPES for $TaSe_3$ [5]. (a) A picture of the strain device we designed and used for ARPES measurements. (b) Finite-element tensile strain simulation of the device (side view). (c) Top view of the device with a strain gauge attached. (d-f) ARPES band dispersions around the zone edge under strain controlled *in-situ*. The strain values applied are described on the top of each panel. (g) ARPES intensity at E_F as a function of the strain value, crossing three distinct phases, i.e., strong TI phase, trivial semimetal phase, and trivial insulator phase.

the band gap was reopened (Fig. 2f), and a metal-insulator transition occurred. These phase variations are reflected on the ARPES intensity at E_F , which is plotted in Fig. 2g as a function of strain values controlled in-situ. Comparing with our calculations, we conclude that we have realized two-step phase transitions, from a strong topological insulator phase, across a topologically trivial semimetallic phase, to a normal band insulator phase.

In summary, we have demonstrated that $TaSe_3$ hosts a strong TI phase in its ground state. By means of *in-situ* strain engineering of the band structure, we have observed two-step phase transitions in $TaSe_3$, including a topological phase transition from a strong TI phase to a trivial semimetal phase, and a subsequent metal-insulator transition. We note that $TaSe_3$ provides an excellent functionality of easily controlling the band topology by mechanical strain. Such a strain method is much simpler, reversible, and thus promising than element substitution method for future application utilizing topological phase transition. Furthermore, our results give prediction that the Majorana fermions emerge in the $TaSe_3$ superconductor and they are controllable by the strain method, so encouraging follow-up research toward the future realization of the quantum computation.

References

[1] S.-Y. Xu *et al.*, Science **332**, 560 (2011).
[2] P. Monceau, Adv. Phys. **61**, 325 (2012).
[3] T. Sambongi *et al.*, J. Phys. Soc. Jpn. **42**, 1421 (1977).
[4] S. Nie *et al.*, Phys. Rev. *B* **98**, 125143 (2018).
[5] C. Lin *et al.*, Nat. Mater. **20**, 1093 (2021).

Authors

C. Lin, M. Ochi[a], R. Noguchi, K. Kuroda, M. Sakoda[b], A. Nomura[c], M. Tsubota[d], P. Zhang, C. Bareille, K. Kurokawa, Y. Arai, K. Kawaguchi, H. Tanaka, K. Yaji[e], A. Harasawa, M. Hashimoto[f], D. Lu[f], S. Shin[g], R. Arita[g,h], S. Tanda[b], and T. Kondo

[a]Osaka University
[b]Hokkaido University
[c]Tokyo University of Science
[d]Gakushuin University
[e]National Institute for Materials Science
[f]SLAC National Accelerator Laboratory
[g]The University of Tokyo
[h]RIKEN

Multipole Polaron in the Devil's Staircase of CeSb

Kondo Group

An electron-boson coupling, that leads to a quasiparticle (QP) of an electron combined with a local bosonic field, can cause interesting properties of condensed matter. For examples, dynamical behavior of a QP often plays roles in electronic instabilities leading to strongly correlated phenomena such as high-temperature superconductivity and colossal magnetoresistance. Thus, the investigation of such a QP is important in materials science. One of the most famous QPs is the polaron by electron-phonon coupling but such a QP state can be realized by coupling to other bosonic modes. However, only three types of electron–boson coupling have been experimentally identified: electron–phonon (or polaron), electron–magnon (or magnetic polaron) and electron–plasmon (or plasmaron) couplings, despite a number of investigations.

In this study, we found a new type of electron–boson coupling which leads to a unique QP state, 'multipole polaron', by investigating a rare-earth intermetallic compound CeSb [1].This new coupling mediates between the itinerant electrons and the bosonic field constituted by the crystal-electric-field (CEF) excitations of the localized 4f states. As evidence for it, we present laser angle-resolved photoemission spectroscopy (ARPES) [2] revealing band renormalization via the coupling of the mobile electron with the CEF excitation. This low-energy feature corresponds to a quadrupole CEF excitation (Jz = ±2) in the J multiplets of the 4f orbitals, possessing the 'multipole' freedom.

We present ARPES maps at the anti-ferromagnetic (AF) phase taken by high-resolution laser-ARPES in Fig. 1a, b. A clear signature for the band renormalization of the Sb 5p band is revealed: the Fermi velocity is largely reduced with a prominent kink at energy $E-E_F = -7 \pm 1$ meV, which directly manifests the presence of an electron–boson coupling (Fig. 1b). In fact, this low energy scale of the kink structure is consistent with the CEF excitation of the Ce 4f orbitals. The CEF splitting in the ordered 4f states of CeSb shows the ground state with Jz ≈ 5/2 (hereafter $f\Gamma_{80}$) and the higher $f\Gamma_8$ states with Jz ≈ 1/2 (hereafter $f\Gamma^*_8$) (Fig. 1c) [3]. The energy scale of the $f\Gamma_{80}$ to $f\Gamma^*_8$ excitation is ~5–6 meV and shows good agreement with the kink energy (7 ± 1 meV). Since the quadrupole CEF excitation ($|\Delta J_z| = 2$) for $f\Gamma_{80}$ to $f\Gamma^*_8$ has multipole character, our observations of the prominent kink reflect a coupling of the electron with the multipole CEF excitation. Such a QP with a large mass enhancement can be described as a multipole polaron that propagates in a sea of lamellar $f\Gamma_{80}$ orbits but largely dressed with the self-induced quadrupole polarization of the longitudinal $f\Gamma^*_8$ orbits, as illustrated by Fig. 1d.

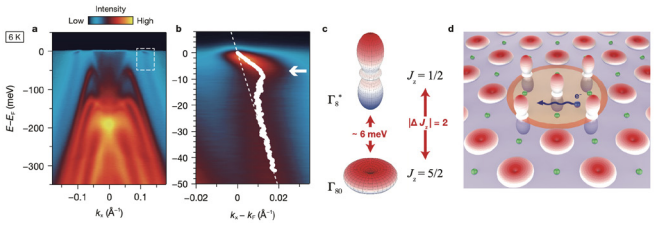

Fig. 1. (a) ARPES band map at T = 6 K (AF phase). (b) Magnified image for the prominent kink in the band dispersion within the dashed rectangles shown in (a). (c) CEF scheme of the localized 4f states in the ordered phase. (d) Schematic of the multipole polaron.

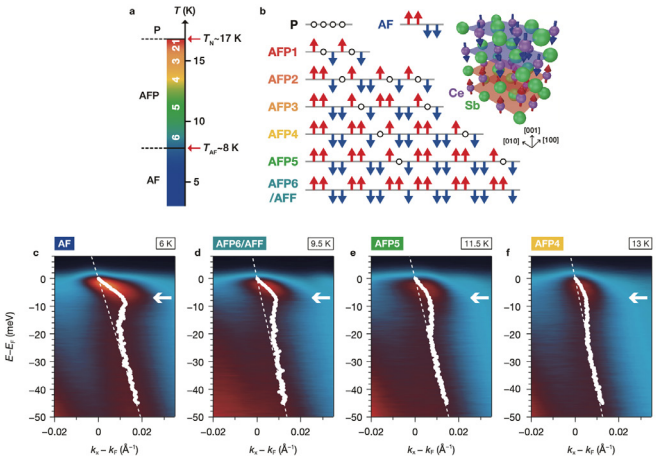

Fig. 2. (a) Temperature scale of the devil's staircase transition at zero field. (b) Schematics of magnetostructures that comprise stackings of ferromagnetic (arrows) and paramagnetic (circles) planes along the crystallography axis [001]. The inset shows the magnetic texture for the magnetic ground state (AF phase). (c-f) Magnified images for the prominent kink in the band dispersion for several distinct phases.

References
[1] Y. Arai *et al*., Nat. Mater. **21**, 410 (2022).
[2] K. Kuroda *et al*., Nat. Commun. **11**, 2888 (2021).
[3] J. Rossat-Mignod *et al*., J. Magn. Magn. Mater. **52**, 111 (1985).
[4] P. Bak, Phys. Today **39**, 38 (1986).

Authors
Y. Arai, K. Kuroda[a], T. Nomoto[b], Z. H. Tin[c], S. Sakuragi, C. Bareille, S. Akebi, K. Kurokawa, Y. Kinoshita, W.-L. Zhang[d], S. Shin[b], M. Tokunaga, H. Kitazawa[e], Y. Haga[f], H. S. Suzuki, S. Miyasaka[c], S. Tajima[c], K. Iwasa[g], R. Arita[b,h], and T. Kondo
[a]Present address: Hiroshima University
[b]The University of Tokyo
[c]Osaka University
[d]Sophia University
[e]National Institute for Materials Science
[f]Japan Atomic Energy Agency
[g]Ibaraki University
[h]RIKEN

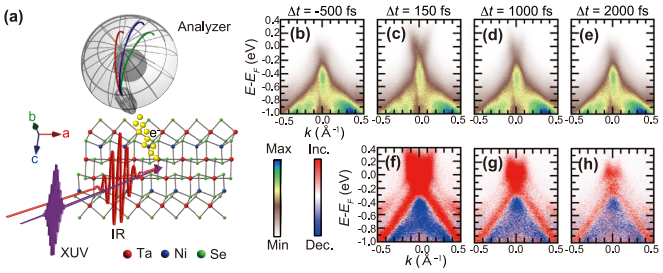

Fig. 1. (a) Schematic illustration of time- and angle-resolved photoemission spectroscopy (TARPES), as applied to Ta_2NiSe_5. The pump pulse is infrared light, whereas the probe pulse is extreme ultraviolet light produced by high harmonic generation. Photoelectrons are detected by a hemispherical electron analyzer. (b)–(e) TARPES spectra of Ta_2NiSe_5. The delay time between the pump and probe is indicated in each panel. (f)–(h) Differential images of TARPES. Red and blue points represent increasing and decreasing photoemission intensity, respectively.

Detecting Electron-Phonon Coupling During Photoinduced Phase Transition

Okazaki and Itatani Groups

Photoinduced phase transitions have been intensively studied owing to their potential capabilities to control a material of interest in an ultrafast manner, which can induce exotic phases unable to be attained at equilibrium. As materials of interest, strongly correlated electron systems provide very fruitful playgrounds because they exhibit very rich phases owing to intertwined couplings between multiple degrees of freedom including charge, orbital, spin, and lattice, where photoexcitation is a very promising way to control their physical properties. Recently, we revealed the photoinduced insulator-to-metal transitions (IMTs) in Ta_2NiSe_5 by using time- and angle-resolved photoemission spectroscopy (TARPES) as schematically shown in Fig. 1(a). Figures 1(b)-1(e) are TARPES spectra of Ta_2NiSe_5 in each delay time, and Figs. 1(f)-1(h) show differential images of TARPES, where red and blue regions correspond to increasing and decreasing intensity, respectively. One can notice that the photo-induced semimetallic bands shown as red regions in Figs. 1(f)-1(h) cross the Fermi level (E_F). However, the key mechanisms are still under debate, and it is currently a central issue as to how the couplings between the electron, lattice, and spin degrees of freedom are evolving during the photoinduced phase transition.

In order to reveal the underlying mechanism in terms of the electron-phonon couplings, we mapped out the frequency-dependent intensity of the Fourier components in the energy and momentum space, which we call frequency-domain angle-resolved photoemission spectroscopy (FDARPES). Figures 2(a)–2(e) show the FDARPES spectra corresponding to the frequencies of 1, 2, 3, 3.75, and 4 THz, respectively. To see each phonon mode associated with the FDARPES spectra, we performed the *ab initio* calculations. First, we calculated the band structure of Ta_2NiSe_5 based on the density functional theory within a generalized gradient approximation (GGA), and confirmed that the results can overall reproduce the photoemission results as shown in Fig. 2(f). Then, we employed the calculations to obtain the phonon modes based on the density functional perturbation theory. The calculated phonon modes corresponding to the 2- and 3-THz modes are shown in Figs. 2(g) and 2(h). Noticeably, the FDARPES spectra exhibit distinctively different behaviors depending on the frequency, which demonstrates that each phonon mode is selectively coupled to the specific electronic bands. Particularly, the 2-THz phonon mode has the strongest signal around E_F, where it consists of a mixture of Ta 5*d* and Se 4*p* orbitals, and this signature is responsible for the collapse of the excitonic insulating phase. In other words, the 2-THz phonon mode is revealed to be the most strongly coupled to the emergent photoinduced electronic bands crossing E_F. Furthermore, we proceeded to compare each FDARPES spectra with the band dispersions before and after photoexcitation. We found that the FDARPES spectrum at 1 THz matches the band dispersions after photoexcitation better than that before photoexcitation as shown in Fig. 2(a), while the FDARPES spectrum at 3 THz is closer to the band dispersions before photoexcitation as shown in Fig. 2(c). This means that both the semimetallic and semiconducting bands are coexistent in the transient state, and suggests the strong electron-phonon couplings for 1-THz and 3-THz phonon modes are associated with the semimetallic and semiconducting bands, respectively. Moreover, this finding demonstrates that, whereas the semimetallic and semiconducting states coexist after photoexciation, the FDARPES method can selectively reveal the coupling of each phonon mode to semimetallic and semiconducting states by the frequency-domain analysis.

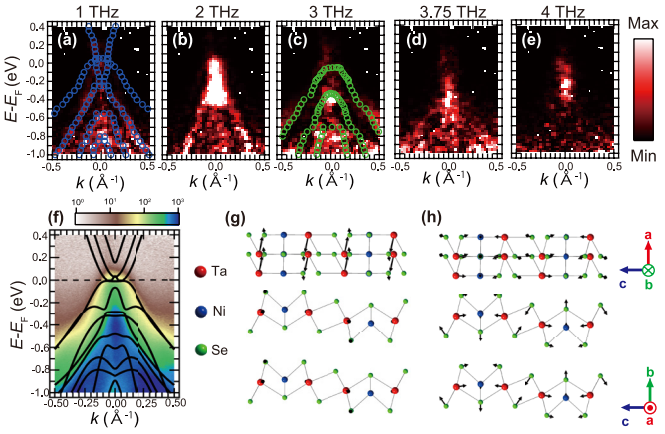

Fig. 2. (a)–(e) Frequency-domain angle-resolved photoemission spectroscopy (FDARPES) spectra shown as frequency-dependent intensities of the oscillation components as a function of energy and momentum. The peak positions in the TARPES spectra after and before photoexcitation are plotted as blue and green circles in (a) and (c), respectively. (f) Calculated band structure of Ta_2NiSe_5 based on the density functional theory within a generalized gradient approximation (GGA) superimposed onto the photoemission spectrum before pump excitation. (g), (h) Calculated phonon modes corresponding to (b) and (c), respectively.

Reference
[1] T. Suzuki, Y. Shinohara, Y. Lu, M. Watanabe, J. Xu, K. L. Ishikawa, H. Takagi, M. Nohara, N. Katayama, H. Sawa, M. Fujisawa, T. Kanai, J. Itatani, T. Mizokawa, S. Shin, and K. Okazaki, Phys. Rev. B **103**, L121105 (2021).

Authors
T. Suzuki, Y. Shinohara[a], Y. Lu[a], M. Watanabe, J. Xu, K. L. Ishikawa[a], H. Takagi[a,b], M. Nohara[c], N. Katayama[d], H. Sawa[d], M. Fujisawa, T. Kanai, J. Itatani, T. Mizokawa[e], S. Shin[a], and K. Okazaki
[a]The University of Tokyo
[b]Max Planck Institute
[c]Okayama University
[d]Nagoya University
[e]Waseda University